# Analyzing the wake of a wind turbine actuated with Dynamic Induction Control

Master of Science Thesis

Emiel Martijn de Boer

TU Delft

EWEM

DTU

# Analyzing the wake of a wind turbine actuated with Dynamic Induction Control

## Master of Science Thesis

by

Emiel Martijn de Boer

to obtain the degree of Master of Science in Aerospace Engineering at the Delft University of Technology and Master of Science in Engineering (European Wind Energy) at the Technical University of Denmark, to be defended publicly on Monday August 23$^{rd}$, 2021 at 09:00.

| | | |
|---|---|---|
| Student number: | 4312430 (TU Delft) | 193495 (DTU) |
| Project duration: | November 1, 2020 – July 31, 2021 | |
| Thesis committee: | Prof. dr. ir. J. W. van Wingerden, | TU Delft, supervisor |
| | Dr. ir. S. J. Andersen, | DTU, supervisor |
| | Prof. dr. S. J. Watson, | TU Delft, censor |
| | Dr. ir. D.J.N. Allaerts, | TU Delft |
| | Dr. ir. A. H. van Zuijlen | TU Delft |

An electronic version of this thesis is available at repository.tudelft.nl and findit.dtu.dk.

TU Delft Delft University of Technology

DTU

# Abstract

To meet current renewable energy demands, there is a major increase in global wind power capacity. Wind turbines are commonly clustered in wind farms. When operating, wind turbines extract energy from the wind, creating a region characterized by a low velocity, called the wake. The wake negatively impacts the power production of downstream wind turbines. This power loss can be alleviated with wind farm control, where an upstream wind turbine deviates from optimal individual operation to improve the power production of the total wind farm. A novel wind farm control concept is dynamic induction control. While the results of dynamic control look promising, the working principles behind the increase in energy are not yet well understood.

This thesis provides a framework to evaluate the transport of kinetic energy into a cylindrical control volume in a wind turbine wake using the instantaneous Navier Stokes energy equation. This approach can provide insight into the time behaviour of kinetic energy transport and can be used in conjunction with the Reynolds Averaged Navier Stokes energy equation. The wake is analyzed using Proper Orthogonal Decomposition to identify the dominant phenomena. The working principle of dynamic induction control is qualitatively described by dividing the wake into three regions: region I, dominated by pressure, region II, dominated by a vortex ring and region III, dominated by turbulence. The peak of transport of kinetic energy occurs in region II, as is confirmed by analysis through the instantaneous Navier Stokes energy equations. Finally, this thesis shows that for a simulation with uniform inflow and where the effect of the nacelle is not modelled, the transition from region II to region III is triggered by the interaction of the vortex ring with an inner vortex ring that forms around the nacelle wake. The nacelle wake is a result of not modelling the nacelle and deemed non-physical, so the ring vortex breakdown location that arises from this simulation does not have much physical meaning.

While there remains a lot of work to be done, this thesis confirms the potential of dynamic induction control shown in previous research. A particularly interesting aspect of dynamic induction control shown in this thesis is that a high amount of wake recovery is compressed into a short distance in the order of $3D$. This property makes dynamic induction control a potential way to decrease turbine spacing in wind farms, allowing the placement of more wind turbines on the same area.

# Preface

The first seed of this project was planted during my Bachelor thesis on wind farm control, supervised by Jan-Willem van Wingerden. After a fantastic journey provided by the European Wind Energy Master, where I followed courses on wind turbine aerodynamics at DTU and TU Delft, I was drawn to the dynamic wind farm control concept. This research was further shaped in collaboration with Søren Juhl Andersen, who is looking at wind turbine interaction from an aerodynamic perspective. I think this thesis is a perfect example of what the European Wind Energy Master can do: bringing together research and researchers from different universities to generate new insights.

I would like to thank Jan-Willem for guiding me through both my Bachelor and Master thesis. His enthusiasm on control concepts is contagious. In addition, I would like to thank Søren for always being able to link the aerodynamic phenomena I showed during our meetings to relevant theory or an interesting paper. Finally, I would like to thank Daniel for our sparring sessions.

*Emiel Martijn de Boer*

# List of Figures


1.1 Photograph of the Horns Rev 2 offshore wind farm. Due to fortunate atmospheric conditions when the photo was taken, the fog is a great visualization of wind turbine wakes, as described by Hasager et al. (2017). Photo by: Bel Air Aviation Denmark - Helicopter Services. . . . . 1

2.1 Streamlines past the rotor and the axial velocity and pressure up and downstream of the rotor. Taken from Hansen (2015). . . . . 6
2.2 Velocity triangle showing the induced velocities for a section of the blade. Taken from Hansen (2015). 7
2.3 Vortex systems. Taken from Sanderse (2009). . . . . 8
2.4 Schematic showing the instantaneous phenomena (top) that lead to the time-averaged flow features in the wake (bottom). Taken from Porté-Agel et al. (2020). . . . . 8
2.5 Wake center motion. Taken from Andersen et al. (2013) . . . . . 9
2.6 Mean kinetic energy transport terms. Note that the obtained results are for a case with wind turbines yawed with respect to the incoming wind. Taken from Houtin—Mongrolle et al. (2021). . . . . 10
2.7 The turbulent Mean Kinetic Energy entrainment term normalized by $\langle u_{hub} \rangle^3$. Taken from Newman et al. (2014) . . . . . 11
2.8 Horizontal Axis Wind Turbine basic working principles . . . . . 12
2.9 Overview of three notable wind farm control techniques proposed for mitigating the wake effect within wind farms. The schematic shows a top-view of two wind turbines aligned with the incoming free stream wind. Green elements highlight changes in turbine operation and wake conditions associated with each control concept. Taken from Kheirabadi and Nagamune (2019). . . . . 13
2.10 Control signal and flow field arising from a receding-horizon approach to dynamic induction control. 14
2.11 Vortex system arising from an adjoint-optimised control signal. Taken from Yılmaz and Meyers (2018) 15
2.12 The average wake velocity over a hypothetical rotor disk behind a wind turbine actuated with dynamic induction control simulated with uniform inflow conditions. Taken from Frederik et al. (2020a) . . . . 15
2.13 Trajectories of the outermost tip vortex filaments. Taken from Brown et al. (2021). . . . . 16
2.14 Wake model classification diagram. Taken from Murcia Leon (2017) . . . . . 17
2.15 Layout of grids around tower, blade and far-field. Taken from Zahle et al. (2007) . . . . . 19
2.16 Illustration of the actuator disk (AD), actuator line (AL) and actuator surface (AS). Taken from Sanderse et al. (2011). . . . . 20
2.17 First 12 spatial and temporal POD modes of a vertical slice of a wind turbine wake in uniform inflow. Taken from De Cillis et al. (2020). . . . . 22
2.18 Spatial development of the $1^{st}$, $3^{rd}$ and $8^{th}$ POD modes of slices parallel to the rotor plane of a wind turbine wake using a turbulence intensity $T_i = 7.1\%$. The energy content of the $1^{st}$, $3^{rd}$ and $8^{th}$ are shown as a function of distance. Circles denote the POD mode shown below. Taken from Sørensen et al. (2015) . . . . . 23

3.1 Mesh visualization for the computational grid for the SOWFA cases with high resolution. The red circle indicates the rotor area. . . . . 29
3.2 Mesh visualization for the available data points of case turb_base. The red circle indicates the rotor area. 31

4.1 Wake diagrams. . . . . 36

5.1 Transient behaviour of the streamwise velocity for case uni_high_base. . . . . 40
5.2 Vertical slice of the mean streamwise velocity at $y = 0$ for case uni_high_base. The dotted lines indicate the rotor plane cylinder. The quiver arrows indicate the local flow direction in the $[xz]$-plane. . . . 40
5.3 Time-averaged streamwise velocity profiles of a vertical line at $y = 0$ at various distances downstream for case uni_high_base. . . . . 41
5.4 Vertical slice of the instantaneous streamwise velocity at $y = 0$ at $t = 5000[s]$ for case uni_high_base. 41
5.5 Isosurface of the Q-criterion where $Q = 0.0005$, colored by the local streamwise velocity, at $t = 5000[s]$ for case uni_high_base. . . . . 41
5.6 Basic flow configuration leading to the Kelvin-Helmholtz instability. Taken from Kundu et al. (2015). . 42
5.7 The first seven spatial modes of Proper Orthogonal Decomposition applied on the velocity field of vertical slices parallel to the rotor plane, separated $2D$ for case uni_high_base. The first mode $r = 0$ is the mean. The modes $r = 1, 2, ..., 6$ oscillate around the mean. The quiver arrows indicate the $v$ and $w$ components of the respective modes. The modes are used for qualitative analysis. Their magnitude is only taken into account in the frequency spectrum. . . . . 43
5.8 The frequency spectrum found by applying Welch's method on the first six temporal modes multiplied with their respective variance $\sigma$, excluding the mean mode, of Proper Orthogonal Decomposition performed on the velocity field of vertical slices parallel to the rotor plane, separated $2D$ for case uni_high_base. . . . . 44
5.9 Relative energy of the first seven POD modes for case uni_high_base. The relative energy of the mean mode is much larger than the other modes and plotted on the right $y$-axis. . . . . 44
5.10 The first seven spatial POD modes for case uni_high_base. The first mode $r = 0$ is the mean. The modes $r = 1, 2, ..., 6$ oscillate around the mean. The quiver arrows indicate the $v$ and $w$ components of the respective modes. The modes are used for qualitative analysis, and their magnitude is only taken into account in the frequency spectrum. . . . . 45
5.11 The frequency spectrum found by applying Welch's method on the first six temporal modes multiplied with their respective variance $\sigma$, excluding the mean mode. . . . . 46
5.12 Transient behaviour of the streamwise velocity for case turb_base. . . . . 46
5.13 A vertical slice of the mean streamwise velocity at $y = 0$for case turb_base. The dotted lines indicate the rotor plane cylinder. The quiver arrows indicate the local flow direction in the $[xz]$-plane. . . . . 47
5.14 Time-averaged streamwise velocity profiles of a vertical line at the rotor centre at various distances downstream for case turb_base. . . . . 47
5.15 A vertical slice of the instantaneous streamwise velocity at $y = 0$ at $t = 1200[s]$ for case turb_base. The dotted lines indicate the rotor plane cylinder. The quiver arrows indicate the local flow direction in the $[xz]$-plane. . . . . 48
5.16 The first seven spatial modes of Proper Orthogonal Decomposition performed on the velocity field of vertical slices parallel to the rotor plane, separated $2D$ for case turb_base. The first mode $r = 0$ is the mean. The modes $r = 1, 2, ..., 6$ oscillate around the mean. The quiver arrows indicate the $v$ and $w$ components of the respective modes. The modes are used for qualitative analysis, and their magnitude is only taken into account in the frequency spectrum. . . . . 49
5.17 The frequency spectrum found by applying Welch's method on the first six temporal modes multiplied with their respective variance $\sigma$ excluding the mean mode, of Proper Orthogonal Decomposition performed on the velocity field of vertical slices parallel to the rotor plane, separated $2D$ for case turb_base. 50
5.18 Relative energy of the first seven modes for case turb_base. The relative energy of the mean mode is much larger than the other modes and plotted on the right $y$-axis. . . . . 50
5.19 The frequency spectrum found by applying Welch's method on the first six temporal modes multiplied with their respective variance $\sigma$ excluding the mean mode, of Proper Orthogonal Decomposition performed on the velocity field of vertical slices parallel to the rotor plane, at $0.5D$ for case turb_base. . . 51
5.20 The frequency spectrum found by applying Welch's method on the time signal of the respective $y$ and $z$-location of the wake centre found at locations separated $1.5D$, for case turb_base. . . . . 51

5.21 Transient behaviour of the streamwise velocity for case uni_high_0.25. . . . . 52
5.22 Periodically oscillating thrust coefficient $C_T[-]$ caused by periodically oscillating blade pitch $\theta$ for case uni_high_0.25. The flow data is divided into bins. Bin walls are indicated with dotted lines. . . . . 52
5.23 Streamwise velocity and pressure at $y = 0$, averaged over a bin, at, from top to bottom, $\theta = -4^o, 0^o, 4^o$ and $0^o$. The dotted lines indicate the rotor plane cylinder. The quiver arrows indicate the local flow direction in the $[xz]$-plane. The letters indicate the locations of interest, tracking the low-velocity field through the wake. . . . . 54
5.24 Vertical slice of the Q-criterion at $y = 0$, computed from velocities averaged over a bin at, from top to bottom, $\theta = -4^o, 0^o, 4^o$ and $0^o$, for case uni_high_0.25. . . . . 55
5.25 Isosurface of the Q-criterion, computed from velocities averaged over a bin at $\theta = -4^o, 0^o, 4^o$ and $0^o$, where $Q = 0.0001$, coloured by the local streamwise velocity, for case uni_high_0.25. . . . . 55
5.26 Schematic overview of the phenomena occurring in the wake of a wind turbine actuated with dynamic induction control. . . . . 56
5.27 The first seven spatial modes of Proper Orthogonal Decomposition performed on the velocity field of vertical slices parallel to the rotor plane, separated $2D$ for case uni_high_0.25. The first mode $r = 0$ is the mean. The modes $r = 1, 2, ..., 6$ oscillate around the mean. The quiver arrows indicate the $v$ and $w$ components of the respective modes. The modes are used for qualitative analysis, and their magnitude is only taken into account in the frequency spectrum. . . . . 57
5.28 The frequency spectrum found by applying Welch's method on the first six temporal modes multiplied with their respective variance $\sigma$ excluding the mean mode, of Proper Orthogonal Decomposition performed on the velocity field of vertical slices parallel to the rotor plane, separated $2D$ for case uni_high_0.25. . . . . 58
5.29 Relative energy of the first seven modes for case uni_high_0.25. The relative energy of the mean mode is much larger than the other modes and is plotted on the right $y$-axis. . . . . 58
5.30 The first seven spatial POD modes for case uni_high_0.25. The first mode $r = 0$ is the mean. The modes $r = 1, 2, ..., 6$ oscillate around the mean. The quiver arrows indicate the $v$ and $w$ components of the respective modes. The modes are used for qualitative analysis, and their magnitude is only taken into account in the frequency spectrum. . . . . 59
5.31 The frequency spectrum found by applying Welch's method on the first six temporal modes multiplied with their respective variance $\sigma$, excluding the mean mode for case uni_high_0.25. . . . . 60

6.1 Power and spatial gradient of power in the axial direction found from the time-averaged velocity, averaged over the rotor plane and multiplied with the rotor plane surface and normalized by the free stream power for case uni_high_base. . . . . 64
6.2 Vertical slice of the mean spatial gradient of power in the $x$-direction at $y = 0$ for case uni_high_base. The dotted lines indicate the rotor plane cylinder. The quiver arrows indicate the local flow direction in the $[xz]$ plane. . . . . 64
6.3 Components of the Reynolds Averaged Navier Stokes energy equation for case uni_high_base and case uni_low_base. . . . . 65
6.4 Vertical slice of the mean radial velocity $\langle u_{rad} \rangle$ at the centre of the rotor plane for case uni_high_base. The dotted lines indicate the rotor plane. The quiver arrows indicate the local flow direction in the $[xz]$ plane. . . . . 66
6.5 Surface integral of Reynolds stress components with a radial velocity term $u_{rad}$ for case uni_high_base. 66
6.6 Vertical slice of the dominant Reynolds stress component $\langle u_{ax} \rangle \langle u'_{ax} u'_{rad} \rangle$ normalized by the free stream velocity $u_\infty^3$, at the center of the rotor plane for case uni_high_base. . . . . 67
6.7 Vertical slice of the pressure field at $y = 0$ for uni_low_base. The dotted lines indicate the rotor plane cylinder. . . . . 67

6.8 Vertical slice of the production of turbulent kinetic energy $\mathcal{P} = \langle S_{ij} \rangle \langle u_i' u_j' \rangle$, normalized by the free stream velocity $u_\infty^3$ and rotor diameter $D$, at $y = 0$ for case uni_high_base. The dotted lines indicate the rotor plane cylinder. . . . . 68
6.9 Temporal behaviour of terms of the instantaneous Navier Stokes equation, evaluated over a slice parallel to the rotor plane at $1D$ and $10D$ downstream of the rotor, for case uni_low_base. . . . . 69
6.10 Components of the instantaneous Navier Stokes energy equation for case uni_high_base and case uni_low_base. . . . . 69
6.11 Power and spatial gradient of power in the axial direction found from the time-averaged velocity, averaged over the rotor plane and multiplied with the rotor plane surface and normalized by the free stream power for case turb_base. . . . . 70
6.12 Components of the Reynolds Averaged Navier Stokes energy and instantaneous Navier Stokes energy equation for case turb_base. . . . . 71
6.13 Vertical slice of the mean radial velocity $\langle u_{rad} \rangle$ at $y = 0$ for case turb_base. The dotted lines indicate the rotor plane cylinder. The quiver arrows indicate the local flow direction in the $[xz]$ plane. . . . . 71
6.14 Surface integral of Reynolds stress components with a radial velocity term $u_{rad}$ for case turb_base. . . 72
6.15 Vertical slice of the dominant Reynolds stress component $\langle u_{ax} \rangle \langle u_{ax}' u_{rad}' \rangle$, normalized by the free-stream velocity $u_\infty^3$, at $y = 0$, for case turb_base. . . . . 72
6.16 Vertical slice at $y = 0$ of the production of turbulent kinetic energy $\mathcal{P} = S_{ij} < u_i' u_j' >$ for case turb_base. $\mathcal{P}$ is normalized by the free stream velocity $u_\infty^3$ and rotor diameter $D$. The dotted lines indicate the edges of the rotor cylinder. . . . . 73
6.17 Power and spatial gradient of power found from $\frac{1}{2}\rho A \langle u_{ax} \rangle^3$ and $\frac{1}{2}\rho A \langle u_{ax}^3 \rangle$ for case uni_high_0.25. The power is averaged over the rotor plane and normalized by the free-stream power. . . . . 74
6.18 Power and spatial gradient of power found from $\frac{1}{2}\rho A \langle u_{ax} \rangle^3$ and $\frac{1}{2}\rho A \langle u_{ax}^3 \rangle$ for case uni_high_base, turb_base and uni_high_0.25. The power is averaged over the rotor plane and normalized by the free-stream power. . . . . 74
6.19 Temporal behaviour of components of the instantaneous Navier Stokes equation for case uni_high_0.25 at $1D$ and $5D$ downstream of the rotor. . . . . 75
6.20 Temporal behaviour of components of the instantaneous Navier Stokes equation for case uni_low_0.25 at $1D$ and $5D$ downstream of the rotor. . . . . 75
6.21 Components of the instantaneous Navier Stokes energy equation for case uni_high_0.25 and case uni_low_0.25. The regions corresponding to the behaviour of the vortex ring are indicated: region I, where no vortex ring is present, region II, where the vortex ring is present, and region III, where the vortex ring has broken down. . . . . 76
6.22 Components of the Reynolds Averaged Navier Stokes energy equation for case uni_high_0.25 and case uni_low_0.25. The regions corresponding to the behaviour of the vortex ring are indicated: region I, where no vortex ring is present, region II, where the vortex ring is present, and region III, where the vortex ring has broken down. . . . . 76
6.23 Vertical slice of the dominant Reynolds stress component $\langle u_{ax} \rangle \langle u_{ax}' u_{rad}' \rangle$, normalized by the free-stream velocity $u_\infty^3$, at $y = 0$, for case uni_high_0.25. The regions corresponding to the behaviour of the vortex ring are indicated: region I, where no vortex ring is present, region II, where the vortex ring is present, and region III, where the vortex ring has broken down. . . . . 77

7.1 Power and spatial gradient of power for different actuation frequencies. Uniform and turbulent inflow baseline cases are also shown for reference. . . . . 80
7.2 Time behaviour of the thrust coefficient $C_T$ for varying inflow cases. . . . . 80

# List of Tables

3.1 Overview of the simulation environments used in this work. Note that the data domain and resolution do not correspond with the computational domain and resolution. . . . . 28
3.2 Overview of the simulation cases analysed in this work. Control cases indicated with a Strouhal number are controlled by applying a sine wave with a frequency corresponding to the indicated Strouhal number and amplitude of $4^o$ on the blade pitch $\theta$. . . . . 28
3.3 Grid resolution for the SOWFA cases with high resolution. . . . . 29
3.4 Grid resolution for the SOWFA cases with low resolution. . . . . 30

# Nomenclature

**Symbols**

| | |
|---|---|
| $\alpha$ | Vertical wind profile power law exponent [-] |
| $\Gamma$ | Circulation [$\frac{m^2}{s}$] |
| $\gamma$ | Yaw misalignment angle [deg] |
| $\hat{n}$ | Unit normal vector [-] |
| $\kappa$ | Von Kármán constant ($\kappa = 0.4$) [-] |
| $\lambda$ | Tip speed ratio, $\frac{\Omega R}{u_\infty}$ [-] |
| $\Omega$ | Rotor rotational speed [rad/s] |
| $\Omega_{ij}$ | Vorticity tensor [$\frac{1}{s}$] |
| $\tau_g$ | Generator torque [Nm] |
| $\theta$ | Blade pitch [deg] |
| $a$ | Axial induction factor [-] |
| $a'$ | Tangential induction factor [-] |
| $C_T$ | Thrust coefficient [-] |
| $D$ | Rotor diameter [m] |
| $f$ | Frequency [Hz] |
| $L$ | Aerodynamic lift [N] |
| $N_b$ | Number of blades [-] |
| $P$ | Power [W] |
| $R$ | Rotor radius [m] |
| $St$ | Strouhal number, $\frac{fD}{u_\infty}$ [-] |
| $T$ | Thrust [N] |
| $u_\infty$ | Free stream wind speed [m/s] |
| $u_{far-wake}$ | Wind speed in the far wake [m/s] |
| $u_{ref}$ | Reference velocity [m/s] |
| $u_{rel}$ | Relative velocity [m/s] |
| $u_{rotor}$ | Wind speed at the rotor [m/s] |
| $z_0$ | Surface roughness length [m] |
| $z_{ref}$ | Reference height [m] |

**Symbols in Navier Stokes equations**

| | |
|---|---|
| $\epsilon$ | Viscous dissipation, $\epsilon = 2\nu S_{ij} S_{ij}$ [$\frac{m^2}{s^3}$] |
| $\langle T_i \rangle$ | Time-averaged flux of energy [$\frac{m^3}{s^3}$] |
| $\langle u_i' u_j' \rangle$ | Reynolds stress tensor [$\frac{m^2}{s^2}$] |
| $\mathcal{P}$ | Production of turbulent kinetic energy, $\mathcal{P} = -\langle u_i' u_j' \rangle \frac{\partial \langle u_j \rangle}{\partial x_i}$ [$\frac{m^2}{s^3}$] |
| $\nu$ | Viscosity [$\frac{m^2}{s}$] |
| $\rho$ | Air density [$\frac{kg}{m^3}$] |
| $f_i$ | Rotor force [N] |
| $p$ | Pressure [$\frac{N}{m^2}$] |
| $S_{ij}$ | Strain rate tensor, $S_{ij} = \frac{1}{2}\left(\frac{\partial u_i}{\partial x_j} + \frac{\partial u_j}{\partial x_i}\right)$ [$\frac{1}{s}$] |
| $T_i$ | Flux of energy [$\frac{m^3}{s^3}$] |

**Symbols related to Proper Orthogonal Decomposition**

| | |
|---|---|
| $\hat{X}$ | A reconstruction of signal $X$ using POD |
| $\Phi$ | Matrix of POD spatial modes |
| $\phi$ | POD spatial mode |
| $\Sigma$ | Matrix of POD singular values |
| $\sigma$ | POD singular value |
| $r$ | Number of modes included in POD truncation |
| $V$ | POD temporal mode |

**Operators**

| | |
|---|---|
| $\bar{\bullet}$ | Spatial average |
| $\frac{D\bullet}{Dt}$ | Material derivative, $\frac{\partial \bullet}{\partial t} + \langle \bullet \rangle \cdot \nabla \bullet$ |
| $\langle \bullet \rangle$ | Time average |
| $\tilde{\bullet}$ | Spatial filter |

**Einstein notation**

| | |
|---|---|
| $\frac{\partial \bullet}{\partial x_i}$ | Gradient, $\frac{\partial \bullet}{\partial x_i} = \nabla \bullet$ |

**Abbreviations**

**ABL** Atmospheric Boundary Layer

**AD** Actuator Disk

**AEP** Annual Electricity Production

**AL** Actuator Line

**AS** Actuator Surface

**CFD** Computational Fluid Dynamics

**DEL** Damage equivalent load

**DIC** Dynamic Induction Control

**DMD** Dynamic Mode Decomposition

**DNS** Direct Numerical Simulation

**DTU** Danmarks Tekniske Universitet

**DWM** Dynamic Wake Meandering

**FAST** Fatigue, Aerodynamics, Structures and Turbulence

**KHI** Kelvin Helmholtz Instability

**L.H.S.** Left Hand Side of an equation

**LES** Large Eddy Simulation

**MKE** Mean kinetic energy

**NREL** National Renewable Energy Laboratory

**OpenFOAM** Open-source Field Operations and Manipulations

**POD** Proper Orthogonal Decomposition

**R.H.S.** Right Hand Side of an equation

**RANS** Reynolds Averaged Navier Stokes

**SOWFA** Simulator for Off/Onshore Wind Farm Applications

**SVD** Singular Value Decomposition

**TI** Turbulence Intensity

**TKE** Turbulent kinetic energy

# Contents

**Abstract** iii

**Preface** v

**List of Figures** vii

**List of Tables** xi

**Nomenclature** xiii

**1 Introduction** 1
- 1.1 Objective and research questions . . . 2
- 1.2 Thesis overview . . . 2

**2 State of the art** 5
- 2.1 Wind turbine aerodynamics . . . 5
- 2.2 The wake effect . . . 8
- 2.3 Wind farm control . . . 11
- 2.4 Wind farm models . . . 16
- 2.5 Wake analysis methods . . . 20
- 2.6 Synthesis . . . 24

**3 Simulation environment** 27
- 3.1 Uniform inflow . . . 28
- 3.2 Turbulent inflow . . . 31

**4 Deriving the transport of kinetic energy equations** 33
- 4.1 Deriving the kinetic energy equations . . . 33
- 4.2 Control volume . . . 36
- 4.3 Numerical implementation . . . 38

**5 Analysis of flow dynamics** 39
- 5.1 Baseline control, uniform inflow . . . 39
- 5.2 Baseline control, turbulent inflow . . . 46
- 5.3 Dynamic induction control . . . 51
- 5.4 Discussion . . . 60

**6 Analysis of transport of kinetic energy** 63
- 6.1 Baseline control, uniform inflow . . . 63
- 6.2 Baseline control, turbulent inflow . . . 70
- 6.3 Dynamic induction control . . . 73
- 6.4 Discussion . . . 77

**7 Evaluating actuation frequencies** 79

**8 Conclusions and recommendations** 81
- 8.1 Conclusions . . . 81
- 8.2 Recommendations . . . 82

8.3 Contribution to the field . . . . . 84

**Bibliography** **85**

# 1

# Introduction

To meet current renewable energy demands, there is a major increase in global wind power capacity. Since 2000, the global installed capacity has gone from $17GW$ in 2000 to $733GW$ today[1]. Currently, about $5\%$ of wind energy capacity is built offshore. Offshore wind turbines are commonly clustered in wind farms to reduce deployment costs of the turbines and electricity grid, and operations and maintenance costs (Boersma et al., 2017). When operating, wind turbines extract energy from the wind, changing the characteristics of the flow downstream of the wind turbine: reducing the flow velocity and increasing the turbulence intensity (Sanderse et al., 2011). This region is referred to as the wake. A photograph of wind turbine wakes in an offshore wind farm is shown in fig. 1.1.

Figure 1.1: Photograph of the Horns Rev 2 offshore wind farm. Due to fortunate atmospheric conditions when the photo was taken, the fog is a great visualization of wind turbine wakes, as described by Hasager et al. (2017). Photo by: Bel Air Aviation Denmark - Helicopter Services.

Wind turbines in wind farms have complex interactions through their wakes. These interactions cause wind turbines in the wake of an upstream wind turbine to be negatively affected in terms of decreased power production, due to the decreased flow velocity, and increased loads, due to the increased turbulence intensity (Sanderse et al., 2011). Research on this phenomenon is ongoing from both an aerodynamic perspective, to capture wake behaviour in models of varying fidelity (Sanderse et al., 2011), and from a wind farm control perspective, to deviate from optimal

[1]https://irena.org/Statistics/View-Data-by-Topic/Capacity-and-Generation/Statistics-Time-Series

individual wind turbine operation to improve a total wind farm objective, such as maximized power production or minimized loads (Kheirabadi and Nagamune, 2019).

Wind farm control falls into three main concepts: axial induction control, wake redirection and wind turbine repositioning. Axial induction control was the first proposed wind farm control concept (Steinbuch et al., 1988). An upstream wind turbine reduces its power extraction from the wind, so that a downstream wind turbine is exposed to a higher wind speed. Wake redirection is based on misaligning an upstream wind turbine with respect to the incoming wind direction to direct the flow with reduced kinetic energy away from a downstream turbine (Jiménez et al., 2010). Wind turbine positioning can be applied in floating wind farms, repositioning individual turbines to minimize wake overlap (Boersma et al., 2017).

A novel approach is dynamic control, where the main control concepts are applied with a time-varying control input. Goit and Meyers (2015) proposed a time-varying axial induction control concept, showing a $16\%$ increase in wind farm power production compared to an uncontrolled reference. Munters and Meyers (2018a) proposed a time-varying wake redirection control concept using wind turbine yaw as actuator, showing an increase of $34\%$. Frederik et al. (2020a) proposed a time-varying wake redirection concept using individual pitch control as actuator, showing an increase of $7.5\%$[2]. The main goal behind these dynamic concepts is to excite dynamics in the wake to promote the transfer of kinetic energy from the high-energy flow surrounding the wake, to the low-energy flow in the wake. This process is also referred to as wake mixing or entrainment.

While the results of dynamic control look promising, the working principles behind the increase in energy are not yet well understood. Munters and Meyers (2018b) suggest that the working principle behind dynamic induction control is the creation of vortex rings in the wake of a wind turbine actuated with dynamic induction control at the right frequency and amplitude of the control signal. This thesis aims to elucidate the working principle behind dynamic induction control.

## 1.1. Objective and research questions

This thesis aims to support the research on dynamic induction control by providing insight into the dynamics that promote the transfer of kinetic energy from the free-stream flow into the wake. The following research questions have been formulated:

- What are the dominant phenomena in the wake that promote wake mixing?
  - What phenomena are present under baseline control with uniform inflow conditions?
  - What phenomena are present under baseline control with turbulent inflow conditions?
  - What phenomena are present under dynamic induction control with uniform inflow conditions?
- How can the transfer of kinetic energy into the wake be quantitatively described?
  - What is the difference between instantaneous and Reynolds Averaged kinetic energy transfer?
  - What are the characteristic regions in the wake of a turbine actuated with Dynamic Induction Control?
- What is the relation between flow and wind farm parameters and effective settings for dynamic induction control?

## 1.2. Thesis overview

The mentioned research questions will be answered in the body of this thesis. This work is structured as follows:

- Chapter 2 presents a literature review, supporting the claims made in the introduction, justifying the relevance of the research objective, and providing the theoretical basis for the rest of this thesis.

[2]Note that even though all of these numbers are found for turbulent inflow, they can not be compared directly to each other without taking into account the specific flow conditions used for the simulation.

- Chapter 3 describes the three simulation environments used in this research.
- Chapter 4 shows a derivation for the transport of kinetic energy into a cylindrical control volume in a wind turbine wake using the instantaneous and Reynolds Averaged Navier Stokes energy equation. The RANS energy equation has seen much use in literature related to wake recovery. The instantaneous Navier Stokes is a novel approach to describe the time behaviour of kinetic energy transport in the context of dynamic induction control.
- Chapter 5 presents a qualitative analysis of the phenomena arising in the wake of a wind turbine with baseline control under uniform inflow, a wind turbine with baseline control under turbulent inflow and a wind turbine with dynamic induction control under uniform inflow. In doing so, the first set of research questions are answered.
- Chapter 6 uses the RANS and instantaneous energy equations derived in chapter 4 to give quantitative insight into the transport of kinetic energy in the wake of a wind turbine with baseline control under uniform inflow, a wind turbine with baseline control under turbulent inflow and a wind turbine with dynamic induction control under uniform inflow. In doing so, the second set of research questions are answered.
- Chapter 7 evaluates different actuating frequencies of dynamic induction control in an attempt to answer the third research question.
- Chapter 8 summarises the findings presented in this thesis, proposes a series of recommendations for further research and provides a brief summation of the main contributions of this work.

# 2

# State of the art

This chapter gives an overview of the relevant theory, phenomena, concepts, models and methods described in literature, supporting the claims made in the introduction, justifying the relevance of the research objective, and providing the basis for the rest of this thesis. The chapter will treat the following topics:

- Wind turbine aerodynamics
- The wake effect
- Wind farm control
- Wind farm models
- Wake analysis methods

The findings are synthesised in section 2.6.

## 2.1. Wind turbine aerodynamics

The first step in understanding the wake interaction between two wind turbines, is the fundamental wind turbine aerodynamics. A one-dimensional, two-dimensional and three-dimensional model of a wind turbine rotor in ideal (inviscid, irrotational, incompressible) flow will briefly be explained here, as they will help to understand some of the main concepts of the wake effect:

- Actuator disk theory
- Blade Element Momentum theory
- Lifting line theory

### 2.1.1. Inviscid rotor and wake models

**Actuator Disk theory**

The most basic representation of a wind turbine is the classical one-dimensional actuator disk theory. In this theory, originally developed by Rankine (1865) and Froude (1889) to describe propellers, the wind turbine rotor is represented as a permeable surface normal to the freestream direction where the forces on the flow are uniformly distributed over the disk. The disk is assumed to be ideal: there are no friction forces, and there is no rotational velocity component

in the wake. Further assuming no external forces and inviscid, incompressible and stationary flow allows applying Bernoulli's principle, leading to the situation graphically depicted in fig. 2.1. The flow slows down gradually from the freestream velocity $u_\infty$ to an average value at the rotor plane $u_{rotor}$, to an average value far downstream in the wake $u_{far-wake}$. As the velocity drops, the static pressure increases according to Bernoulli. Additionally, the streamlines must diverge as a result of continuity. Energy is extracted from the flow at the actuator disk, where there is a pressure drop from immediately upstream to immediately downstream of the rotor. The slowdown of the streamwise velocity is defined using the axial induction factor $a$, according to eq. (2.1).

$$u_{rotor} = (1 - a)u_\infty \tag{2.1}$$

An important result from actuator disk theory is the famous Betz limit, showing that a turbine with no losses can capture a maximum of $16/27 = 59.3\%$ of the kinetic energy in the wind when the axial induction factor $a = 1/3$.

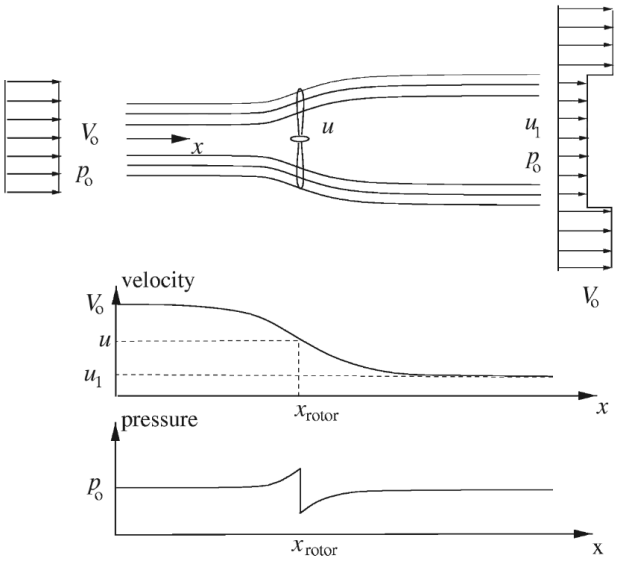


Figure 2.1: Streamlines past the rotor and the axial velocity and pressure up and downstream of the rotor. Taken from Hansen (2015).

**Blade Element Momentum Theory**

The actuator disk theory was extended by Glauert (1935) to the widely used Blade Element Momentum (BEM) theory. In BEM, wake rotation is taken into account by introducing a tangential induction factor $a'$. Additionally, the rotor is discretized into blade sections or annuli, effectively making a two-dimensional description of the system. The relative velocity and angle of attack of each blade section can be determined using a velocity triangle as in fig. 2.2.

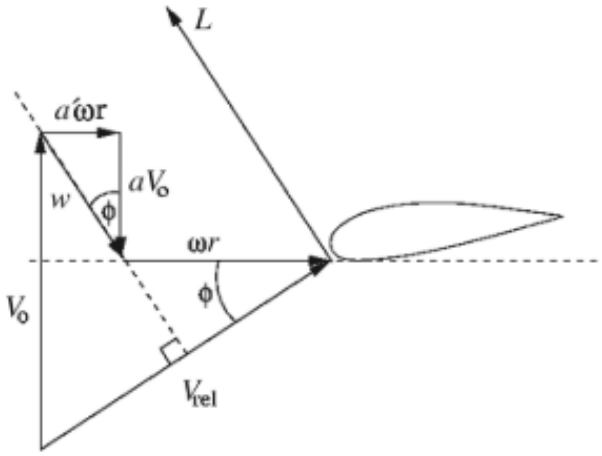


Figure 2.2: Velocity triangle showing the induced velocities for a section of the blade. Taken from Hansen (2015).

The local aerodynamic loads and induction factors can be found from the local geometry, relative velocity, angle of attack and airfoil polars in an iterative manner when assuming negligible flow velocity in the spanwise direction to ensure independence of annuli and an infinite number of blades, to ensure constant force from the blades on the flow in the tangential direction.

Two corrections must be taken into account in the BEM method: the Glauert correction for heavily loaded rotors and the Prandtl tip loss correction. The Glauert correction is an empirical relation between the thrust coefficient and the axial induction factor. The Prandtl tip loss correction has to be applied to correct for the assumption of an infinite number of blades.

Applying the BEM method introduces some power extraction losses with respect to the Betz limit derived from an ideal rotor in the actuator disk model. Firstly, there is energy spent in rotation in the wake. Secondly, the tip loss is taken into account, reducing the blade's efficiency near the tip. Finally, a drag force can be introduced by the airfoil polars.

**Lifting line theory**

The lifting line theory uses a vorticity-based approach to give a three-dimensional description of the flow field. The airfoil is represented as a line in the spanwise direction. According to the Kutta-Joukowski theorem ($L = \rho U_{rel} \times \Gamma$), the generation of lift is related to circulation around the airfoil. This leads to a distributed bound vortex along the airfoil. At the tip, air flows from the pressure side to the suction side, creating the tip vortex. The bound vortex and tip vortex can be modelled as vortex filaments with strength $\Gamma$. According to Helmholtz second theorem, a vortex filament can not end in a fluid. A closed vortex filament system must exist. The vortex filament that closes the system, called the shed vortex, can be considered far downstream. This is shown in fig. 2.3a. Applying the lifting line theory to the rotating wind turbine blades creates the helical vortex system shown in fig. 2.3b. There is a bound vortex along the three blades, a root vortex and three helical tip vortices.

A vortex filament describes the induced velocity around that filament. The Biot-Savart law can be applied to find the three-dimensional velocity at every point. The tangential component in the helical tip vortices results in an induced axial velocity against the direction of the wind at any spanwise position of the blade. The axial component in the helical tip vortices results in an induced tangential velocity at any spanwise position of the blade. These so-called downwash effects result in a change in the perceived angle of attack by the blade, and add an induced drag component to the local lift. This reduces the efficiency potential when compared to two-dimensional models. It is assumed that the induced velocities in and spanwise direction can be neglected for wind turbine blades.

The Glauert correction is not necessary as the wake self-adjusts to heavily loaded rotors. The Prandtl tip loss correction is not necessary as the induced velocities already capture this effect.

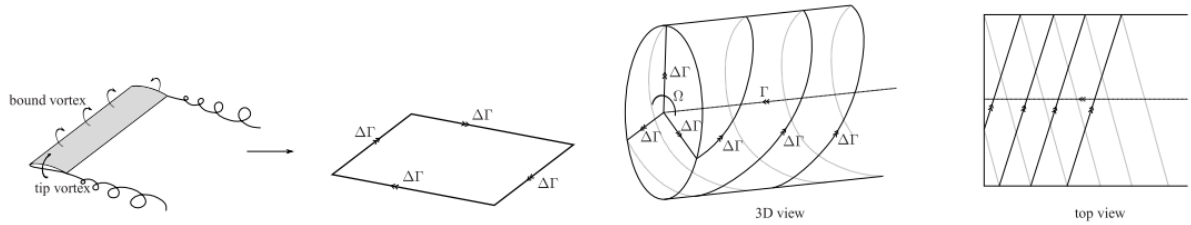


(a) Vortex system on a finite wing.

(b) Vortex system on a three-bladed rotating turbine.

Figure 2.3: Vortex systems. Taken from Sanderse (2009).

For further information on fundamental wind turbine aerodynamics, the reader is referred to the "Wind Energy Handbook" by Burton (2001) and "Aerodynamics of Wind Turbines" by Hansen (2015).

a

## 2.2. The wake effect

The main characteristic of a wind turbine wake can already be seen from the one-dimensional actuator disk analysis: a tubular region of reduced streamwise velocity downstream of the wind turbine with an area larger than the rotor. Barthelmie et al. (2009) show that wake effects can cause Annual Energy Production losses up to $12\%$ for a wind farm compared to turbines in free stream. The wake is further characterised by an increase in turbulence intensity caused by tip vortices, turbulent boundary layers leaving the blades and mechanical turbulence from the blade and tower and wake (Sanderse (2009)). However, physical phenomena in the wake become more complex when the assumptions for the simplified models break down. A schematic of the important phenomena in a wind turbine wake is shown in fig. 2.4.

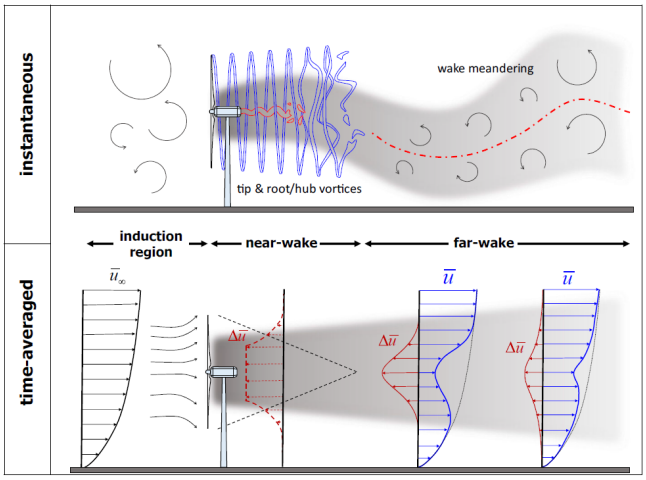


Figure 2.4: Schematic showing the instantaneous phenomena (top) that lead to the time-averaged flow features in the wake (bottom). Taken from Porté-Agel et al. (2020).

The wind turbine wake is typically divided into two regions: the near wake and the far wake (Vermeer et al. (2003)). The transition happens between one and five rotor diameters, depending on flow properties such as turbulence intensity and tip speed ratio (Sanderse (2009), Vermeer et al. (2003), Porté-Agel et al. (2020)).

The near wake is the area immediately behind the rotor where the properties of the rotor can be discriminated. In ideal flow, these properties are the velocity deficit and tip and root vortices found from actuator disk theory, blade

element momentum theory and/or lifting line theory. In a non-idealized wake, the difference in velocity between the air inside the wake and outside the wake creates a shear layer in which turbulent eddies are formed. The shear layer thickens when moving downstream, which is shown schematically by the dotted lines in the time-averaged schematic of the wake in fig. 2.4. At some distance downstream from the rotor plane, the thickening shear layers overlap. Because of the ambient shear layer, the turbulence intensity in the upper part of the shear layer is higher than in the lower part (Sanderse (2009)).

The tip vortices expand due to vortex stretching, and the radius of the helical structure increases as the wake expands. The stability of tip vortices is investigated in Sarmast et al. (2014) and extended by Sørensen et al. (2015). An expression is formulated that predicts the breakdown of the helical tip vortex as a function of rotor properties: number of blades $N_b$, tip speed ratio $\lambda$, convection velocity $u_c$, rotor radius $R$, turbulence intensity $TI$ and thrust coefficient $C_T$ as eq. (2.2).

$$\left(\frac{l}{R}\right)_{\text{near wake}} = -\left(\left(\frac{16\tilde{u}_c^3}{N_b \lambda C_T}\right)\ln\left(0.3TI\right) + 5.5\ln\left(TI\right)\right) \tag{2.2}$$

After the breakdown of the tip vortices, a transition region is reached. When the upper and lower shear layers overlap, the far wake region is reached, characterized by an approximately self-similar Gaussian velocity-deficit distribution. The properties of the rotor can no longer be discriminated.

### 2.2.1. Wake meandering

As a result of large turbulent structures present in the atmospheric boundary layer, the entire wake experiences a random unsteady oscillation with respect to the time-averaged wake centerline. This is known as wake meandering. While wake meandering improves wake mixing, it also introduces unsteady asymmetric loads on downstream turbines, possibly increasing fatigue loads. Models for wake meandering and their effects are presented by Ainslie (1988) and Larsen et al. (2008).

Andersen et al. (2013) show that in an infinitely long row of wind turbines, a vortex shedding frequency arises, in the form of an oscillating wake center in the lateral and vertical direction, with a Strouhal number of $St = 0.19[-]$.

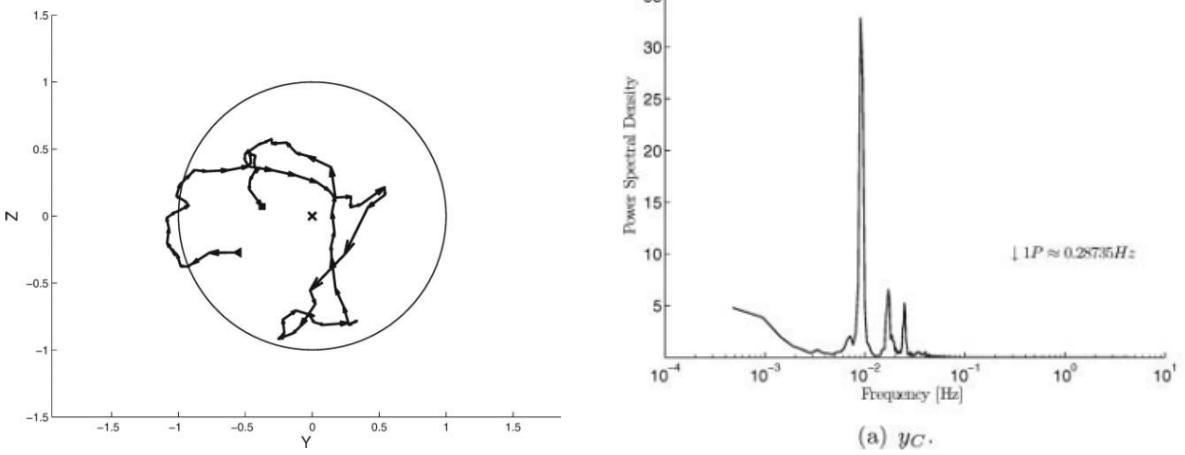


(a) Trajectory of the wake center.

(b) Power spectral density of the wake center motion.

Figure 2.5: Wake center motion. Taken from Andersen et al. (2013)

The Strouhal number is a dimensionless number describing oscillating flow mechanisms, relating the frequency

of vortex shedding $f$, a characteristic length $D$ and flow velocity $u$. For a cylinder, experiments show that the vortex shedding frequency remains close to $St = 0.2[-]$ over a large range of Reynolds numbers (Kundu et al., 2015).

$$St = \frac{fD}{u} \tag{2.3}$$

### 2.2.2. Wake mixing

The turbulent interaction of the wake with the surrounding flow promotes the extraction of kinetic energy in the form of streamwise velocity from the surrounding flow to the wake. This is referred to as wake mixing or entrainment and results in an increasing streamwise velocity. Actuator disk theory predicts a decreasing streamwise velocity in the streamwise direction. There is a point downstream of the rotor with the maximum velocity deficit, after which the velocity deficit decreases due to wake mixing (Annoni et al., 2016).

The transport of mean kinetic energy can be derived from the Reynolds Averaged Navier Stokes equation, and integrated over a streamtube to find eq. (2.4) (Houtin—Mongrolle et al., 2021):

$$\begin{aligned} \oiint_S (\underbrace{\frac{1}{2}\rho \langle \tilde{u}_i \rangle \langle \tilde{u}_i \rangle \langle \tilde{u}_j \rangle}_{\text{Advection}} + \underbrace{\langle \tilde{u}_j \rangle \langle \tilde{p} \rangle}_{\text{Pressure work}} + \underbrace{\langle \tilde{u}_i \rangle \rho \left\langle \tilde{u}_i' \tilde{u}_j' \right\rangle}_{\text{Reynolds stress work}} + A_{j,S}) n_j dS \\ - \iiint_{V_{st}} (\underbrace{\rho \left\langle \widetilde{S}_{ij} \right\rangle \left\langle \tilde{u}_i' \tilde{u}_j' \right\rangle}_{\text{Production of TKE}} + \underbrace{\rho \langle \tilde{u}_i \rangle \left\langle \tilde{f}_i \right\rangle}_{\text{Turbine work}} + A_V) dV = 0 \end{aligned} \tag{2.4}$$

with $\langle u_i' u_j' \rangle$ denoting the Reynolds stress tensor and $S_{ij}$ denoting the strain rate tensor. The advection term captures the change in the flux of mean kinetic energy through the streamtube surface. The production of Turbulent Kinetic Energy (TKE) term removes energy from the mean. Viscous and subgrid-scale terms on the surface and in the volume are gathered as $A_S$ and $A_V$. The terms in this equation describe the increase in mean kinetic energy, captured in the advection term, due to various work terms on the stream tube surface and the production of the TKE term in the streamtube volume. The derivation and application of eq. (2.4) in this research is further discussed in chapter 4.

The various terms are shown in fig. 2.6a. Houtin—Mongrolle et al. (2021) find the local dominant terms in the mean kinetic energy equation and link those to flow dynamics to define areas I, II, III and IV in the wake.

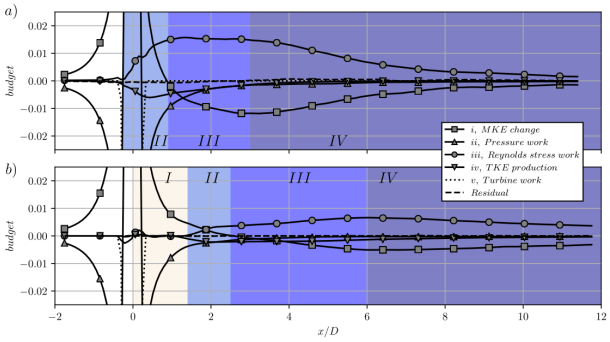


(a) Mean kinetic energy equation terms integrated over the streamtube cross-section. a) is a case with uniform inflow. b) is a case with turbulent inflow. Both cases are misaligned with the wind by $\gamma = 30^o$.

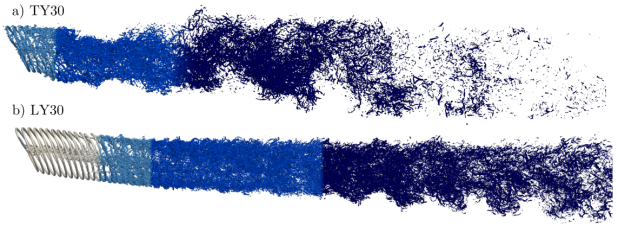


(b) 3D visualization of the instantaneous Q-criterion.

Figure 2.6: Mean kinetic energy transport terms. Note that the obtained results are for a case with wind turbines yawed with respect to the incoming wind. Taken from Houtin—Mongrolle et al. (2021).

Newman et al. (2014) and Andersen et al. (2017) focus on the Reynolds stress term ($iii$ in equation eq. (2.4)). They show that one of the Reynolds stress terms is dominant and has a characteristic spatial distribution as shown in fig. 2.7.

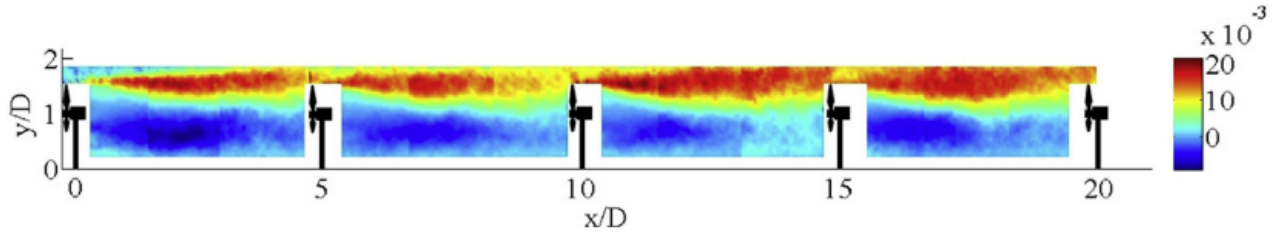


Figure 2.7: The turbulent Mean Kinetic Energy entrainment term normalized by $\langle u_{hub} \rangle^3$. Taken from Newman et al. (2014)

## 2.3. Wind farm control

Wind turbines that are in the wake of an upstream wind turbine experience a reduced power production and increased extreme and fatigue loads. To mitigate these effects, wind turbines in a wind farm can be controlled considering the effect of their operation on their neighbours. This is known as wind farm control. Three notable wind farm control concepts are shown in fig. 2.9. The working principle of these control techniques can be related to stationary wake physics. More recently, wind farm control concepts that are based on dynamic wake physics have been proposed. The basics of individual wind turbine control will be explained here, as well as the wind farm control concepts based on stationary and dynamic physics.

### 2.3.1. Individual wind turbine control

To understand the concepts of wind farm control, the most commonly used practical implementation of a rotor will be explained here. The simplified rotor models describe a Horizontal Axis Wind Turbine, the most commonly produced and used wind turbine. The rotor converts the momentum of the flow field into aerodynamic forces that drive the generator. The degrees of freedom for a wind turbine are:

- Blade pitch ($\theta$) - The rotor blades can be rotated around the axis aligned with the blades to change the angle of attack and thus aerodynamic forces on the blade.
- Generator torque ($\tau_g$) - The generator torque can be controlled to influence the rotational velocity of the rotor and power capture.
- Yaw ($\gamma$) - The nacelle can rotate around the axis aligned with the tower to align the rotor perpendicular to the wind.

The basic components of a wind turbine are shown in fig. 2.8a. For individual wind turbine control, different operating regions can be distinguished as a function of wind speed. These regions are shown in fig. 2.8b, along with a line of the total power present in the wind.

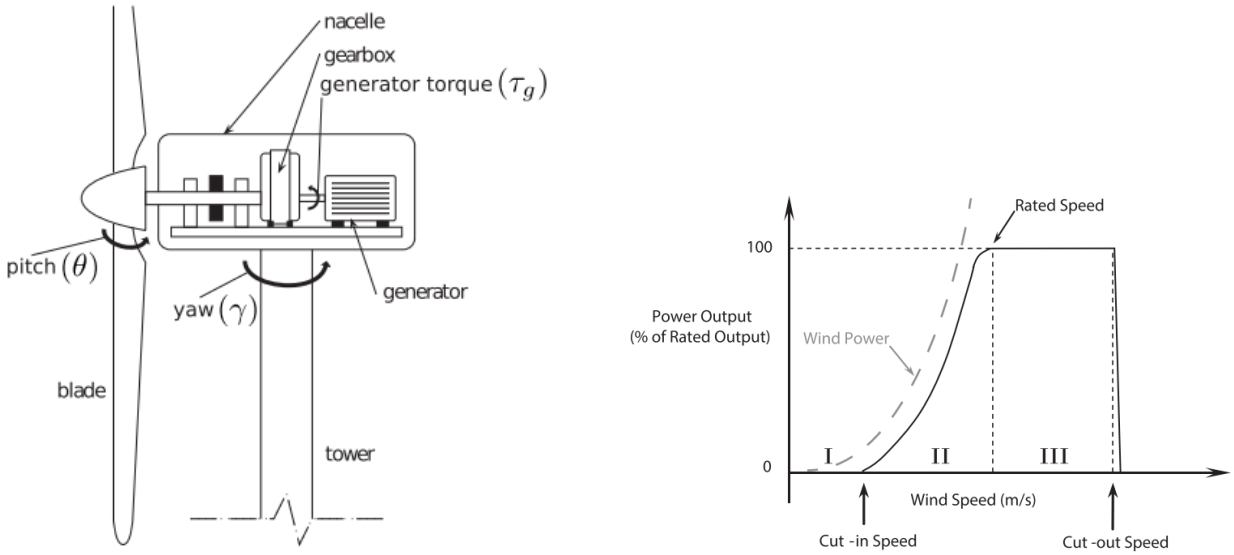


(a) Horizontal-axis wind turbine with labelled main components and control variables. Taken from Boersma et al. (2017).

(b) Typical wind turbine power curve. Taken from Boersma et al. (2017).

Figure 2.8: Horizontal Axis Wind Turbine basic working principles

In Region 1, the wind speed is below the cut-in wind speed. This means that it is not viable to operate the wind turbine for practical reasons, such as a minimum generator speed.

In Region 2, the wind turbine is operated to extract as much as possible energy from the flow. According to the Betz limit, at most $16/27 = 59.3\%$ of the power in the wind can be extracted, while in practice, this number lies even lower. Therefore, the line of actual power output lies below the line of total power present in the wind. The operating conditions for the pitch $\theta$ and torque $\tau_g$ follow from BEM theory. Pitch $\theta$ is most commonly set to be $0$, and the torque follows from the $K - \Omega^2$ law (Burton, 2001).

In Region 3, the generator has reached its maximum power output. The wind turbine is controlled to operate at the maximum power output and maximum rotational velocity by manipulating the blades' angle of attack.

### 2.3.2. Steady-state wind farm control

The control scheme for an individual wind turbine, where the wind turbine is operated to extract the maximum power from the wind without considering its neighbours, is referred to as greedy control. However, it might be beneficial to incorporate the surrounding wind turbines into the operating strategy of individual wind turbines. Wind farm control can be applied to achieve one or more of the following objectives: increasing power production, reducing structural degradation, and improving power quality (Kheirabadi and Nagamune, 2019). Increasing power production is most relevant when the wind turbines are operating in Region 2. Several concepts are described in literature and discussed below.

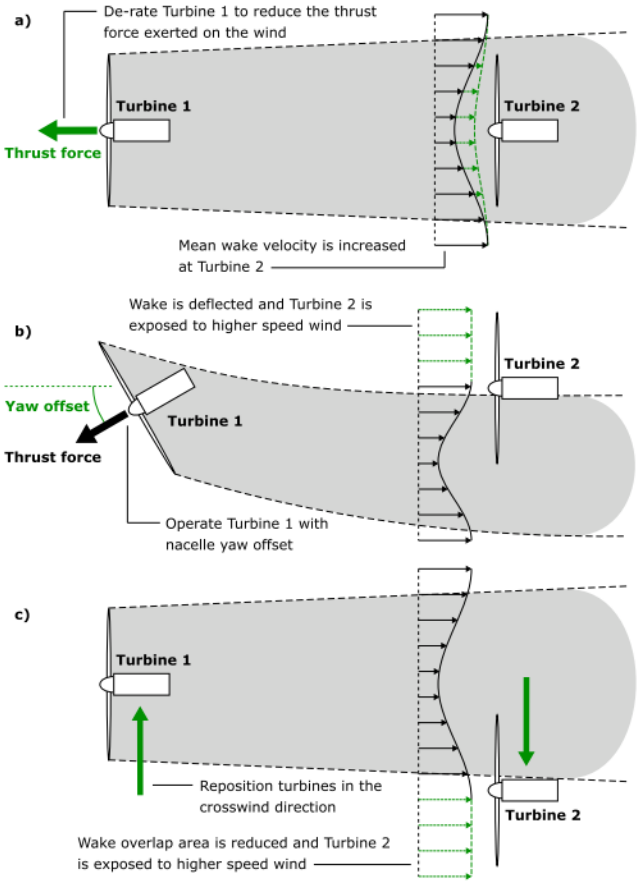


Figure 2.9: Overview of three notable wind farm control techniques proposed for mitigating the wake effect within wind farms. The schematic shows a top-view of two wind turbines aligned with the incoming free stream wind. Green elements highlight changes in turbine operation and wake conditions associated with each control concept. Taken from Kheirabadi and Nagamune (2019).

The first wind farm control concept is power de-rating or axial induction-based control. It was proposed by Steinbuch et al. (1988) and is shown in fig. 2.9a. It can be shown using actuator disk theory that when Turbine 2 is directly in the far wake of Turbine 1, where the streamwise velocity is $u_{rotor} = u_\infty(1-2a)$, that the optimal operation point for the axial induction factor $a$ of Turbine 1, when considering the power production as the sum of the power of Turbine 1 and Turbine 2, is not $a = 1/3$, but $a$ is in fact lower (Johnson and Thomas (2009)).

While axial induction-based control showed initial promising results, recent simulation studies (Nilsson et al. (2015)) and wind tunnel tests (Campagnolo et al. (2016)) show limited success of axial induction control. This is partly because the concept is based on actuator disk theory, which does not take into account wake recovery. Engineering wake models can be used to approximate the wake recovery (Annoni et al. (2016)).

The second wind farm control concept is yaw-based wake redirection. As shown in fig. 2.9b, the thrust force exerted by the wind turbine on the has a net force component perpendicular to the flow direction, causing the wake to deflect. This effect has been studied numerically by Jiménez et al. (2010) and experimentally by Wagenaar and Schepers (2012). While Turbine 1 operates in sub-optimal conditions, Turbine 2 has a potential power increase when the wake is successfully deflected. When applied correctly, the power production as the sum of Turbine 1 and Turbine 2 is greater when applying yaw-based wake redirection.

The third wind farm control concept is turbine repositioning of floating offshore wind turbines. Similar to yaw-based wake redirection, the goal is to reduce the overlap of the wake of Turbine 1 with the rotor of Turbine 2. The work-

ing principle is to re-position the individual turbines in real-time to achieve this goal as shown in fig. 2.9c (Boersma et al. (2017)).

### 2.3.3. Dynamic wind farm control

A new approach to wind farm control is to apply the notable wind farm control concepts, but with a time-varying input. The goal of this approach is to increase wake mixing by exciting dynamic wake phenomena.

Goit and Meyers (2015) propose to apply time-varying axial induction control, where the axial induction factor is calculated from a receding-horizon approach and using knowledge of the flow field. Qualitative analysis of the instantaneous flow fields shows that the working principle of this concept is based on the quasi-periodic shedding of vortex rings. The vortex rings can be seen in fig. 2.10b. This approach shows promising results, with an energy extraction increase of up to $16\%$ for one hour. However, this approach should be considered a benchmark rather than a practical control approach due to the high computational cost of finding the control settings in real-time using a receding horizon approach.

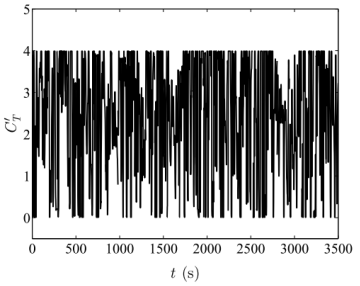


(a) Time evolution of the thrust coefficient of one of the turbines in the wind farm. Taken from Goit and Meyers (2015).

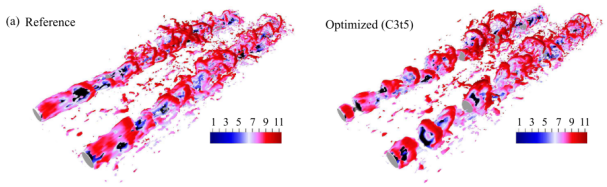


(b) Instantaneous snapshots of a portion of the wind-farm flow field for the reference (left) and optimized (right) case. Isosurface of vorticity magnitude coloured by streamwise velocity. Wind turbines are represented as grey disks. Taken from Munters and Meyers (2018b).

Figure 2.10: Control signal and flow field arising from a receding-horizon approach to dynamic induction control.

Yılmaz and Meyers (2018) perform a similar adjoint-based optimization for dynamic induction control. For uniform inflow, they find a control signal where three vortices are released in a cycle, that interact as they travel downstream at different velocities, shown in fig. 2.11b. This is a different working principle than the one proposed by Goit and Meyers (2015). This might be because of a different rotor model (Goit and Meyers (2015) use an Actuator Disk model, Yılmaz and Meyers (2018) use an Actuator Line model), a higher resolution, or including the effect of rotor inertia.

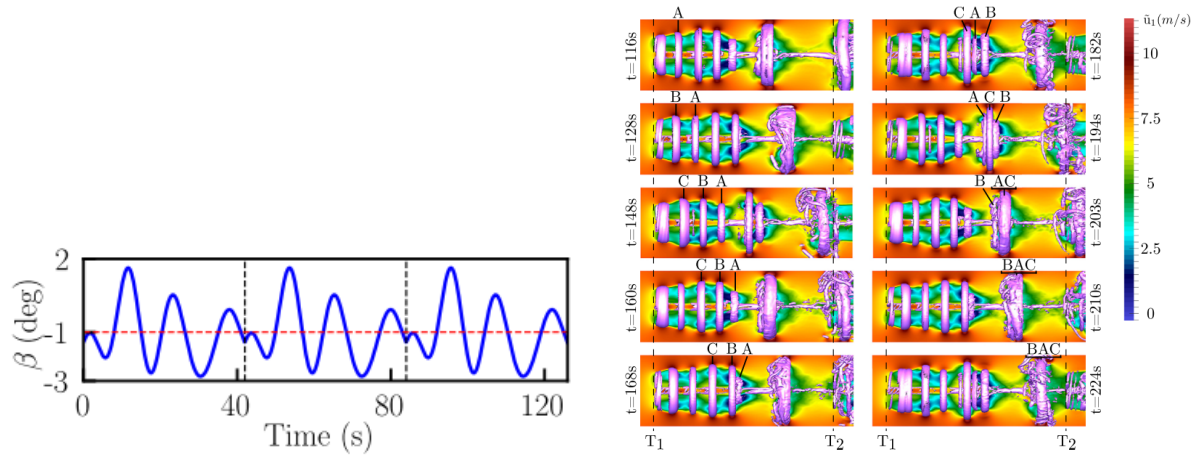


(a) Pitch control signal.

(b) Q-criterion.

Figure 2.11: Vortex system arising from an adjoint-optimised control signal. Taken from Yılmaz and Meyers (2018)

Munters and Meyers (2018b) propose a simpler approach, where the axial induction factor is implemented as a sinusoidal signal on an actuator disk. This approach successfully mimics the shedding of vortex rings using the receding horizon approach. Frederik et al. (2020a) perform a grid study to find the wake velocity increase as a function of actuation frequency, shown in fig. 2.12. At $5D$ downstream, the optimal frequency is approximately $St = 0.25[-]$. Interestingly, the optimal frequency differs as a function of distance from the upstream turbine: at $3D$, the optimal frequency is approximately $St = 0.35[-]$. Frederik et al. (2020b) show that the increase in weighted Damage Equivalent Load of the blade edgewise and hub is small, in the order of $0.3$ to $0.4\%$.

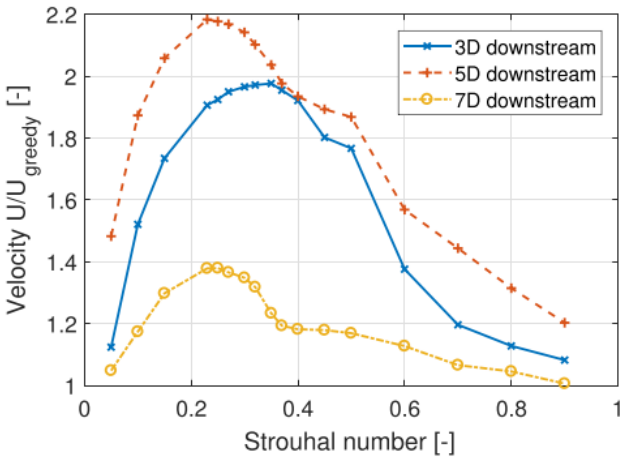


Figure 2.12: The average wake velocity over a hypothetical rotor disk behind a wind turbine actuated with dynamic induction control simulated with uniform inflow conditions. Taken from Frederik et al. (2020a)

A similar but alternate approach is presented by Brown et al. (2021). The wind turbine is leveraged as a flow actuator to accelerate the breakdown of the tip vortices. This causes an early transition of the near wake to the far wake, where the far wake has better wake mixing properties. The working principle is based on triggering a mutual inductance, vortex pairing, instability by pitching the blades $\omega = N_b(k - 0.5)$ times per rotor revolution, where

$N_b$ is the number of blades and $k$ are positive integers. This is then a fundamentally different working principle than the one proposed by Munters and Meyers (2018b), which is based on pitching the blades at a frequency around $St = 0.1 - 0.6[-]$ to shed coherent vortex rings in the wind turbine wake.

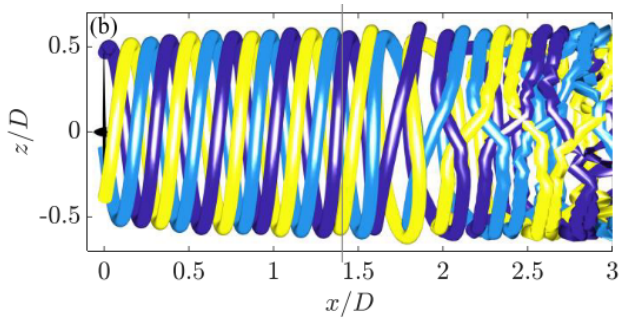


Figure 2.13: Trajectories of the outermost tip vortex filaments. Taken from Brown et al. (2021).

A dynamic control concept based on yaw-based wake redirection is presented by Munters and Meyers (2018a). While dynamic yawing provides no significant benefits for uniform inflow compared to static yaw control, it performs better in turbulent flow.

Frederik et al. (2020a) propose a novel method of redirecting the wake. By applying dynamic individual pitch control, varying tilt and yaw moments are applied on the rotor. As a result, the wake slowly varies its direction in time. It is hypothesized that this enhances wake mixing while maintaining lower power and thrust variations than those experienced in dynamic induction control or dynamic yaw control.

## 2.4. Wind farm models

To qualitatively and quantitatively analyse the wake effect on the performance of a wind farm, and its mitigation through wind farm control, three approaches can be taken.

Firstly, an analytical model can be defined. The benefits of analytical models include that their solutions are exact and give insight into the system. The main drawback is that they can only be defined when making strong assumptions that do not necessarily hold. Examples of analytical wind farm models are given in section 2.1. Indeed, the solutions are exact and provide insight, but several key phenomena are missed due to the strong assumptions.

Secondly, the wake effect can be analysed experimentally. Testing in the field gives the most accurate representation of the system without making assumptions. Drawbacks of testing in the field include measurement errors and a high cost and time investment. Additionally, new wind farm control concepts might fall outside the wind turbine design envelope, making wind turbine operators reluctant to approve wind farm control tests. Alternatively, the wake effect can be analysed in a wind tunnel. This mitigates the time and cost investment compared to experimenting in the field but still comes with considerable cost. However, new complexities arise in correctly scaling the system to a size that fits in the available wind tunnel.

Finally, the wake effect can be analysed numerically. A range of methods to numerically describe the wake exist, which typically include a trade-off between accuracy and computational time. The benefits of numerical analysis include a limited requirement of resources, easy variation of parameters, and full knowledge of the flow field. In contrast, drawbacks include numerical errors and the need for an accurate turbulence model.

The rest of this chapter will discuss various numerical wake models.

### 2.4.1. Wake models

Numerical wind farm models are typically classified from low-fidelity to high-fidelity. Increasing fidelity captures more physics but has a higher computational cost. A classification of wake models is shown in fig. 2.14.

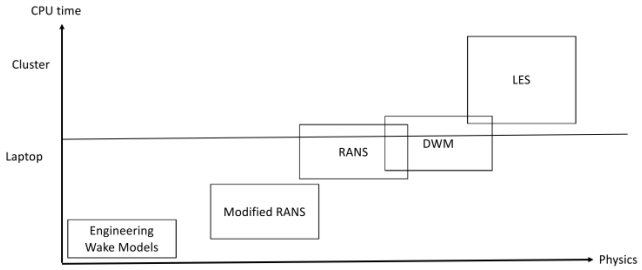


Figure 2.14: Wake model classification diagram. Taken from Murcia Leon (2017)

**Parametric models**

The low fidelity wake models give a parametric description of the steady or quasi-steady wake velocity profile and are based on the self-similar properties of the far wake. The parameters need to be tuned on experimental data or simulations. They are also referred to as kinematic, engineering or parametric wake models.

One of the simplest representations of the wake is the Jensen Park model based on the description by Jensen (1983) and Katic et al. (1987). It models the wake as a linearly expanding conical region with a velocity deficit that depends on the distance behind the rotor and a wake recovery coefficient.

By extending the Jensen Park model with a model for wake deflection through yaw (Jiménez et al. (2010)) and the improving wake overlap model, Gebraad (2014) extended the Jensen Park model to the FLOw Redirection and Induction in Steady-State (FLORIS) model. A dynamical version named FLOw Redirection and Induction Dynamics (FLORIDyn) is presented by Gebraad and Van Wingerden (2014). Other examples of low-fidelity wake models are the Frandsen model (Frandsen et al. (2006)).

Where low-fidelity wake models lack in detail, they are surprisingly accurate on a wind farm level (Boersma et al., 2017). Their low computation time makes them suitable for applications where many iterations are needed, such as wind farm design purposes or control purposes.

**Navier Stokes equations**

To capture more detail in the wake, simulations based on the incompressible Navier-Stokes equations as given in eq. (2.5) can be used. It is valid to use the incompressible Navier-Stokes equations because the flow velocity typically does not exceed $100m/s$ or a Mach number of $0.3$ in current wind turbines (Sanderse (2009)).

$$\begin{aligned} \frac{\partial u_i}{\partial x_i} &= 0 \\ \underbrace{\frac{\partial u_i}{\partial t}}_{\text{Acceleration term}} + \underbrace{\frac{\partial u_i u_j}{\partial x_i}}_{\text{Advection term}} &= - \underbrace{\frac{1}{\rho}\frac{\partial p}{\partial x_i}}_{\text{Pressure term}} + \underbrace{\nu \frac{\partial^2 u_i}{\partial x_j \partial x_j}}_{\text{Viscous term}} \end{aligned} \tag{2.5}$$

The Navier-Stokes equations can be applied numerically when discretizing spatially in a grid and temporally. This is referred to as Computational Fluid Dynamics (CFD). However, the phenomena that govern wind turbine wakes happen on a large range of physical and time scales (Sørensen et al. (2015)). Resolving all these scales is referred to as Direct Numerical Simulation (DNS) and is not feasible for wind farm wake simulations with current computing power. This can be solved by making assumptions to simplify the equations and/or introducing a turbulence model.

**Dynamic Wake Meandering model**

The Dynamic Wake Meandering Model (DWM) proposed by Larsen et al. (2008) is based on the conjecture that the transport of the wake can be modelled as if it acts as a passive tracer driven by the large-scale turbulence structures in the Atmospheric Boundary Layer. It is based on 2-D parabolic Navier-Stokes equations neglecting pressure terms.

The DWM consists of a model for velocity deficit, wake meandering, and rotor added turbulence. The velocity deficits are found using an actuator disc model. According to Taylor's hypothesis, the velocity deficits are assumed to be passive tracers that convect downstream with the mean wind speed and move laterally and vertically according to large scale lateral and vertical turbulence velocities in the rotor plane. The turbulence model includes components from wake meandering, added wake turbulence and ambient turbulence. The turbulence is modelled with an eddy viscosity model. The DWM improves the accuracy of engineering models by describing the dynamic wake meandering phenomenon at the cost of a slightly higher computational cost. It remains dependent on tuning parameters for the turbulence model.

**Reynolds Averaged Navier Stokes equations**
Commonly, the Navier Stokes equations are assessed in a time-averaged sense by decomposing the velocity in terms of its time-averaged value $\langle u \rangle$ and its fluctuations $u'$, called Reynolds decomposition:

$$u = \langle u \rangle + u' \tag{2.6}$$

Applied to the Navier Stokes equations eq. (2.5), the Reynolds Averaged Navier Stokes equations can be derived:

$$\underbrace{\langle u_j \rangle \frac{\partial \langle u_i \rangle}{\partial x_j}}_{\text{Advection term}} = - \underbrace{\frac{1}{\rho} \frac{\partial \langle p \rangle}{\partial x_i}}_{\text{Pressure term}} + 2\nu \underbrace{\frac{\partial \langle S_{ij} \rangle}{\partial x_i}}_{\text{Viscous term}} - \underbrace{\frac{\partial \langle u_i' u_j' \rangle}{\partial x_i}}_{\text{Reynolds stress}} \tag{2.7}$$

The main differences from the Navier Stokes equations are:

- The acceleration term $\frac{\partial u_i}{\partial t} = 0$, because we are assuming a steady-state solution.
- The appearance of the Reynolds stress tensor $\langle u_i' u_j' \rangle$. The Reynolds stress tensor arises from applying the Reynolds decomposition on the advective term with a fluctuating velocity field and represents the averaged momentum transfer caused by turbulent fluctuations.

This simplifies the Navier-Stokes equations by only requiring time-averaged velocities. However, the Reynolds stress tensor contains six additional unknown variables that must be modelled. A turbulence model is needed to close the equation. Various turbulence models exist and are discussed by Göçmen et al. (2016). RANS can describe the time-averaged velocity field in the wake with more accuracy than lower fidelity models that make stronger assumptions in their physics. A drawback of RANS is that it is not able to describe dynamic phenomena due to time-averaging. Additionally, the turbulence models are dependent on parameters that need to be tuned by experiments or higher fidelity simulations.

**Large Eddy Simulation**
Instead of applying time-averaging on the incompressible Navier-Stokes equations, a spatial low-pass filter can be applied, leading to the Large Eddy Simulation (LES) governing equations. Again, a new term appears, called the sub-filter scale stress tensor:

$$\underbrace{\frac{\partial \tilde{u}_j}{\partial t}}_{\text{Acceleration term}} + \underbrace{\frac{\partial \tilde{u}_i \tilde{u}_j}{\partial x_i}}_{\text{Advection term}} = - \underbrace{\frac{1}{\rho} \frac{\partial \tilde{p}}{\partial x_i}}_{\text{Pressure term}} + \nu \underbrace{\frac{\partial^2 \tilde{u}_j}{\partial x_i \partial x_i}}_{\text{Viscous term}} - \underbrace{\frac{\partial \tau_{ij}}{\partial x_i}}_{\text{Sub-filter scale stress tensor}} \tag{2.8}$$

When the filter width is in the inertial subrange, the sub-filter scale stress tensor can be modelled. This is based on the assumption that the smallest eddies have a more or less universal character that does not depend on the flow geometry (Sanderse et al., 2011)). Various turbulence models exist and are discussed by Meneveau and Katz (2000). Advantages of LES include that more wake behaviour is solved and less is modelled, so it is less dependent on the turbulence model for accuracy. Additionally, it inherently captures dynamic behaviour. This comes at the cost of increased computational time.

For further information on wind farm models, the reader is referred to the reviews by Sanderse et al. (2011) and Göçmen et al. (2016), and for more information on turbulence modelling to "Turbulent flows" by Pope (2000).

### 2.4.2. Rotor modelling

A representation of the rotor blades is necessary to solve the Reynolds Averaged Navier Stokes equations or the Large Eddy Simulation equations. There are two main approaches for representing the rotor: direct modelling or through a body force.

#### Direct modelling

The blades can be resolved using direct modelling. This is the most exact way of representing the blades, but also very computationally expensive (Sanderse et al., 2011). A visualization of the mesh around wind turbine components is shown in fig. 2.15.

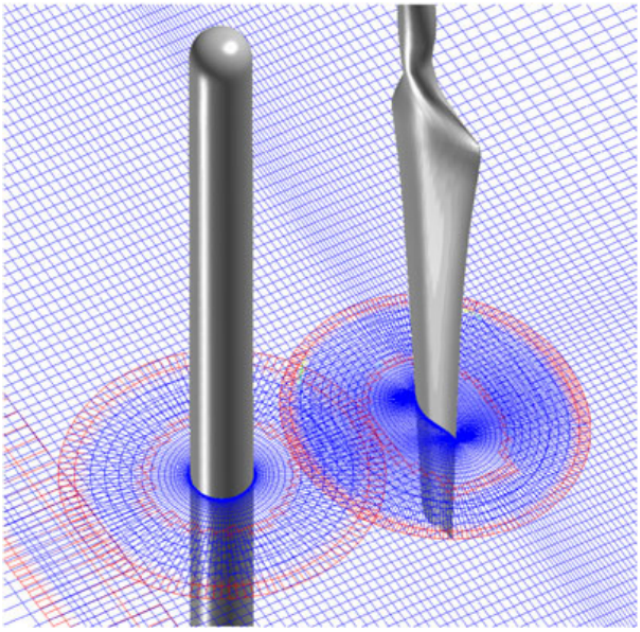

Figure 2.15: Layout of grids around tower, blade and far-field. Taken from Zahle et al. (2007)

#### Body force

In order to avoid calculation of blade boundary layers, the rotor blade can be modelled as a force on the flow $f_i$ by adding it to the Navier Stokes momentum equation eq. (2.5) (Sanderse et al., 2011):

$$\underbrace{\frac{\partial u_i}{\partial t}}_{\text{Acceleration term}} + \underbrace{\frac{\partial u_i u_j}{\partial x_i}}_{\text{Advection term}} = - \underbrace{\frac{1}{\rho}\frac{\partial p}{\partial x_i}}_{\text{Pressure term}} + \underbrace{\nu \frac{\partial^2 u_i}{\partial x_j \partial x_j}}_{\text{Viscous term}} + \underbrace{f_i}_{\text{Rotor force}} \tag{2.9}$$

There are three approaches for finding the force term $f_i$: the actuator disk, the actuator line, and the actuator surface. For the actuator disk method, the force depends on the radial position but is constant over an annulus. First, the local flow velocity needs to be found. Then, the sectional force can be found using the local lift and drag coefficient like in the Blade Element Momentum method. An extension of the actuator disk method is the actuator line method, introduced by Sørensen and Shen (2002). The line forces are not averaged over an annulus but computed locally as

a function of local flow velocity. A regularization kernel is used to transfer the rotating line forces to the stationary mesh.

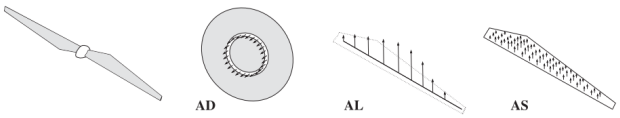


Figure 2.16: Illustration of the actuator disk (AD), actuator line (AL) and actuator surface (AS). Taken from Sanderse et al. (2011).

### 2.4.3. Inflow generation

Depending on the wake model, several inflow conditions can be imposed. The most common alterations to a uniform inflow profile are a vertical wind profile and turbulent fluctuations.

**Atmospheric Boundary Layer**

The vertical wind profile, arising from the planetary boundary layer, is commonly described using a logarithmic profile (Göçmen et al., 2016):

$$u(z) = \frac{u_\star}{\kappa} \ln\left(\frac{z}{z_0}\right) \tag{2.10}$$

where $u_\star$ is the friction velocity, $\kappa$ is the von Kármán constant ($\approx 0.4$), z is the elevation above ground level and $z_0$ is the surface roughness length. The vertical wind profile can also be characterized by the power law (Göçmen et al., 2016):

$$u(z) = u_{ref}\left(\frac{z}{z_{ref}}\right)^{\alpha} \tag{2.11}$$

where $u_{ref}$ is the undisturbed mean wind speed at a reference height $z_{ref}$ and $\alpha$ is the power-law exponent.

The atmospheric stability condition affects the flow characteristics. For wind energy applications, the atmosphere is generally assumed neutral (Göçmen et al., 2016). However, atmospheric stability can have a large effect on the inflow conditions.

**Turbulence intensity**

A more sophisticated way to generate inflow conditions is to create a separate simulation without wind turbines. The flow can develop in this so-called precursor simulation before it is used as an inflow condition to the final simulation with wind turbines (Göçmen et al., 2016). An advantage of the precursor is that both the atmospheric boundary layer and turbulence intensity can develop.

Alternatively, inflow turbulence can be simulated by a spectral tensor turbulence model developed by Mann (1994). The spectral tensor contains information on spectra, cross-spectra and coherence to provide suitable turbulence for engineering applications in wind energy.

## 2.5. Wake analysis methods

### 2.5.1. Q-criterion

A common way to identify coherent structures in fluid mechanics is to apply the Q-criterion proposed by Hunt et al. (1988). The Q-criterion is defined in terms of instantaneous velocity gradients. It can also be written in terms of the trace of the vorticity tensor $||\Omega_{ij}||$ and the trace of the strain rate tensor $||S_{ij}||$. Positive values of the Q-criterion are associated with rotation-dominated regions of the flow, or vortices. Negative values are associated with straining regions of the flow.

$$
\begin{aligned}
Q &= -\frac{1}{2}\frac{\partial u_i}{\partial x_j}\frac{\partial u_j}{\partial x_i} \\
Q &= \frac{1}{2}(||\Omega_{ij}||^2 - ||S_{ij}||^2)
\end{aligned}
\tag{2.12}
$$

### 2.5.2. Wake centre

The wake centre is found using the Weighted Geometric-Center Approach[1], where the wake centre is defined to be the average of all points below a threshold instantaneous streamwise velocity, weighted by the local instantaneous streamwise velocity. An instantaneous lateral and vertical wake centre can be identified at all slices downstream of a wind turbine in this fashion. For this research, a threshold value of $u_{thresh} = \frac{2}{3}u_\infty$ has been chosen.

$$
x_{wake} = \frac{\sum_i u_{ax} x_i}{\sum_i u_{ax}}, \quad \forall u_{ax} < u_{thresh} \tag{2.13}
$$

### 2.5.3. Proper Orthogonal Decomposition

A method to investigate wake dynamics is to decompose the flow field into spatial and temporal modes through Proper Orthogonal Decomposition (POD). An example of POD modes arising in a wind turbine wake is shown in fig. 2.17a. The modes show up in pairs, where each mode pair can be linked to a phenomenon in the flow. Modes 1 and 2 are linked to the tip/root vortex helical system, modes 3 and 4 are linked to the von Kármán vortex street shed by the tower, modes 5 and 6 are harmonics of the tip/root vortex helical system, modes 7 and 8 are again linked to the von Kármán vortex street, modes 9 and 10 are linked to a Kelvin-Helmholtz-like instability (this is further discussed in section 5.1.1) and the last two modes are conjectured to be related to the wake meandering phenomenon (De Cillis et al., 2020). POD also links the spatial modes to temporal modes, which can be related to a characteristic frequency. The characteristic frequencies of the first 6 mode pairs are shown in fig. 2.17b. Effectively, the flow field in the wake is described as a superposition of coherent structures in space and time. These properties make POD an excellent tool to identify dominant phenomena in a wind turbine wake.

[1] https://ewquon.github.io/waketracking/methodology.html

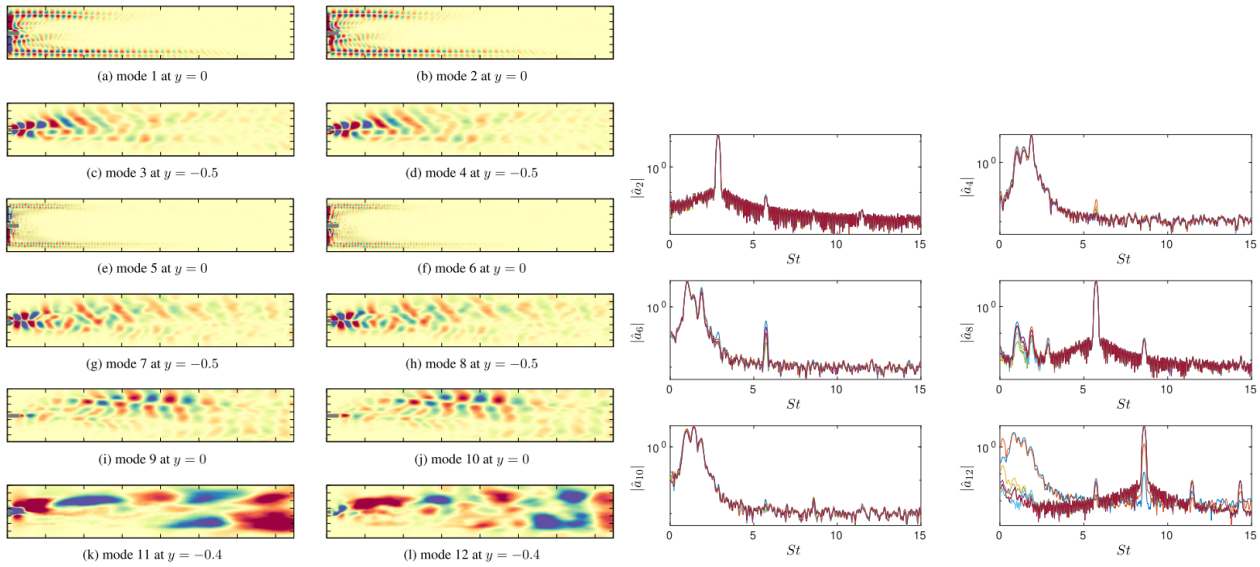


(a) Streamwise velocity contours of the first 12 Proper Orthogonal Decomposition modes.

(b) Welch's spectra for the first 6 mode pairs. The colours indicate different numbers of time snapshots.

Figure 2.17: First 12 spatial and temporal POD modes of a vertical slice of a wind turbine wake in uniform inflow. Taken from De Cillis et al. (2020).

Proper Orthogonal Decomposition can also be applied to slices parallel to the wind turbine. For example, Sørensen et al. (2015) use POD to determine the length of the near wake by evaluating the shape and energy content of the large coherent turbulent structures shown in fig. 2.18.

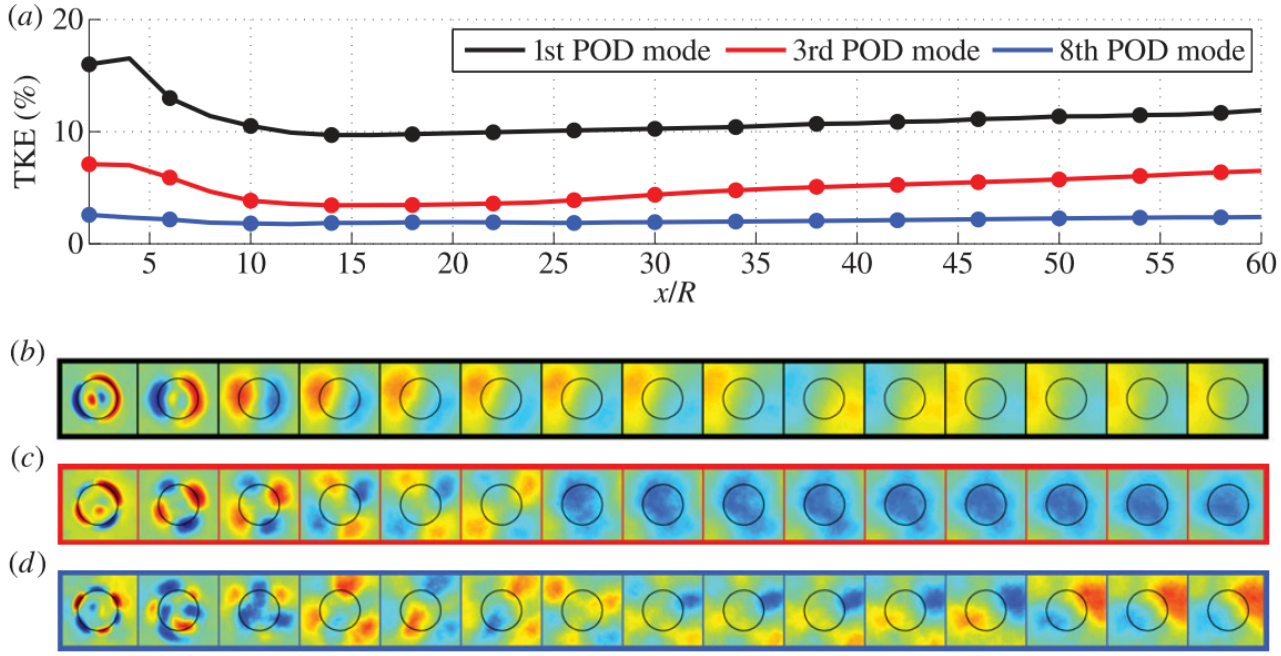


Figure 2.18: Spatial development of the $1^{st}$, $3^{rd}$ and $8^{th}$ POD modes of slices parallel to the rotor plane of a wind turbine wake using a turbulence intensity $T_i = 7.1\%$. The energy content of the $1^{st}$, $3^{rd}$ and $8^{th}$ are shown as a function of distance. Circles denote the POD mode shown below. Taken from Sørensen et al. (2015)

**Implementation**

An overview of applying POD on turbulent flows is given by Berkooz et al. (1993). When using a Computational Fluid Dynamics approach to solve a flow field problem, data is available on a grid of points for every time step. Every data point contains velocity information in the $x$, $y$ and $z$ direction and might additionally contain pressure information. This gives $n = n_x \times n_y \times n_z \times n_t \times n_q$ data points, with $n_x$, $n_y$ and $n_z$ denoting the number of grid points in the $x$, $y$ and $z$ direction, $n_t$ the number of time-steps and $n_q$ denotes the number of quantities used. For example, when using the velocity in the $x$, $y$ and $z$ direction, $n_q = 3$, and when adding the pressure information, $n_q = 4$. The first step in POD is to rearrange the three-dimensional data of every time-step $u(x, y, z, q, t)$ into tall column vectors corresponding to a time snapshot. For example , for $t = 1$ the data is represented as in eq. (2.14).

$$x_1 = \begin{bmatrix} u_{1,1,1,1,t=1} \\ \vdots \\ u_{n_x,n_y,n_z,n_q,t=1} \end{bmatrix}_{nx1} \tag{2.14}$$

All data can now be represented in the two-dimensional matrix $X$ as in eq. (2.15). Subscript $m$ denotes the number of time snapshots.

$$X = \begin{bmatrix} | & | & | & | \\ x_1 & x_2 & \cdots & x_m \\ | & | & | & | \end{bmatrix}_{nxm} \tag{2.15}$$

The Proper Orthogonal Decomposition is based on the Singular Value Decomposition, eq. (2.16). This decomposes the signal $X$ into orthogonal spatial modes, which are contained as column vectors in $\Phi$. $\Sigma$ is a diagonal matrix con-

taining the singular values $\sigma$, which are greater than zero and ordered from high to low. The singular values describe the variance of each mode. The temporal behaviour is captured in $V^*$.

$$X = \Phi_{n\times m}\Sigma_{m\times m}V^*_{m\times m} \tag{2.16}$$

Writing out the matrices:

$$X = \begin{bmatrix} | & | & \dots & \vdots \\ \phi_1 & \phi_2 & \dots & \phi_m \\ | & | & \dots & \vdots \end{bmatrix}_{n\times m} \begin{bmatrix} \sigma_1 & 0 & \dots & 0 \\ 0 & \sigma_2 & \dots & 0 \\ \vdots & \vdots & \ddots & 0 \\ 0 & 0 & 0 & \sigma_m \end{bmatrix}_{m\times m} \begin{bmatrix} - & V_1 & - \\ - & V_2 & - \\ \vdots & \vdots & \vdots \\ - & V_m & - \end{bmatrix}_{m\times m} \tag{2.17}$$

The spatial modes $\Phi$ can be interpreted by reshaping the tall column vectors back into the dimensions of the grid. For example, reshaping $\phi_1$ of the POD performed by De Cillis et al. (2020) results in the spatial mode shown in the top left of fig. 2.17a.

Commonly the mean is subtracted first. When the mean is not subtracted first, this will result in a spatial mode that corresponds to the mean, and does not contain a frequency component. This is referred to as the $0^{th}$ mode.

The temporal modes $V$ are interpreted by transitioning from the time domain to the frequency domain. Welch's method is applied to the row vectors. Welch's method is similar to the Fourier transform but applies a method based on windows to reduce the noise caused by imperfect and finite data Welch (1976). The frequency spectrum is shown in fig. 2.17b.

**Reconstruction**

A reconstructed flow field $\hat{X}$ can be found from the sum of spatial modes, multiplied with their variance and temporal mode. Typically, a summations is done from mode $1$ to mode $r$:

$$\hat{X} = \sum_{k=1}^{r} \Phi_k \Sigma_k V^*_k \tag{2.18}$$

The rank-$r$ POD reconstruction $\hat{X}$ is the best rank-$r$ approximation of $X$ according to the Eckart-Young theorem.

**Wake mixing reconstruction**

Instead of reconstructing the flow field, the POD modes can be used to reconstruct the transport of mean kinetic energy terms that were discussed in section 2.2.2 and will be further discussed in chapter 4 (De Cillis et al., 2020).

For example, the surface integral of one component of the Reynolds stress term can be reconstructed as:

$$\oiint_{\mathcal{S}} -\left(\langle u\rangle\langle u'w'\rangle\right) d\mathcal{S} \approx \sum_{k=1}^{r} \oiint_{\mathcal{S}} -\left(\phi_0^u \phi_k^u \phi_k^w \sigma_k\right) d\mathcal{S} \tag{2.19}$$

Here, $\phi_0^u$ denotes the $0^{th}$ mode, so the mean component of the flow in the $u$ direction. $\phi_k^u$ and $\phi_k^w$ denote the turbulent fluctuations in the $u$ and $w$ direction. The correct magnitude of the fluctuations is reconstructed using the variance $\sigma_k$. Applying this method can provide insight into what modes are most beneficial for energy flux (De Cillis et al., 2020).

## 2.6. Synthesis

The literature review shows that there are several dynamic control concepts and that even within the niche dynamic induction control, there are several distinct concepts. Additionally, the literature review shows that so far, the work on dynamic control focuses either on elaborate adjoint-based optimization methods to find optimal control signals, or on grid searches to find optimal control signals, and less on the working principles behind the concepts.

This work focuses on sinusoidal dynamic induction control with an actuation frequency around $St = 0.25[-]$. This is because Munters and Meyers (2018b) and Frederik et al. (2020a) separately found this to be effective at the same actuation frequency. Additionally, there seem to be coherent dynamics in the wake in the form of vortex rings that will form an interesting basis for analysis. The aim is that the analysis provided in this thesis provides further understanding of the working principles behind this concept to better understand what would be efficient control signals.

**Simulation**

Because dynamic induction control inherently relies on dynamic phenomena in the wind turbine wake, assessing the wake using time-averaging assumptions such as Reynolds-Averaged Navier Stokes codes is unsuitable. Additionally, the dynamic phenomena triggered by dynamic induction control are not well understood, so choosing a model able to capture as much of the dynamics as possible is desired. On the other hand, case properties include a large domain, high Reynolds numbers and small turbulence scales, so there is a limit imposed by computational power. For these reasons, dynamic induction control is evaluated in an LES model, where the wind turbine is modelled as an actuator line. The simulation environment is further elaborated on in chapter 3.

To distinguish phenomena arising from dynamic induction control from phenomena naturally occurring in the wake, a uniform vertical wind profile is chosen. However, it should be noted that the effectiveness of dynamic induction control is likely influenced by interaction with turbulent inflow. Munters and Meyers (2018b) mention that sinusoidal dynamic induction control exploits natural instabilities in the vortex sheets shed from a wind turbine and find an effective frequency of $St = 0.25[-]$, while Andersen et al. (2013) find a naturally occurring frequency in the wake of an infinitely long row of wind turbines with a turbulent inflow of $St = 0.2[-]$. The proximity of these frequencies suggests the phenomena might interact. Therefore, for further research, investigating dynamic induction control with turbulent inflow is necessary.

# 3

# Simulation environment

The analyses performed in this work are based on simulations in a Large Eddy Simulation framework, using an actuator line representation of the wind turbine rotor. As discussed in section 2.6, LES can describe the dynamic phenomena that arise when applying dynamic induction control. The actuator line representation gives a more accurate representation of the effect of the rotor on the near-wake. There are three simulation environments used in this work. An overview of the environment properties is shown in table 3.1.

Two simulation environments are solved in the Simulator for Off/Onshore Wind Farm Applications (SOWFA). SOWFA[1] is a Computational Fluid Dynamics (CFD) solver based on Open-source Field Operations and Manipulations (OpenFOAM) libraries[2] coupled with the Fatigue, Aerodynamics, Structures and Turbulence (FAST) tool[3] developed by the US National Renewable Energy Laboratory (NREL).

The first of these environments has a higher spatial and temporal computational resolution than the second, as can be seen from table 3.3 and table 3.4. They will hereafter be referred to as the high resolution and low-resolution SOWFA environment. Note that the qualification of high and low resolution is only relative to each other. The reason for choosing a lower resolution is the lower computational time, allowing the evaluation of more cases. Comparison with the higher resolution cases will show that there are no large scale phenomena missed by using the lower resolution, but there is a difference between the kinetic energy transport terms. This will be discussed in section 6.4.3. The SOWFA cases are further discussed in section 3.1.

Additionally, a case with a wind turbine in a shear layer with turbulent inflow simulated in a different solver, EllipSys3D, is analysed. EllipSys3D is a CFD solver developed in collaboration with the Technical University of Denmark (DTU) and the former National Laboratory for Sustainable energy (Risø) in Denmark, see Sørensen (1995). Given that the case computed in EllipSys3D is computed under similar conditions as the cases computed in SOWFA, namely a single wind turbine, where the flow field is solved using an LES framework where the rotor is represented by an actuator disk, this allows an evaluation of the differences between uniform and turbulent inflow for a baseline control case. Additionally, the methods for assessing kinetic energy transport are validated in the turbulent inflow environment. The EllipSys3D case is further discussed in section 3.2.

[1] https://www.nrel.gov/wind/nwtc/sowfa.html
[2] https://openfoam.org/
[3] https://www.nrel.gov/wind/nwtc/fast.html

Table 3.1: Overview of the simulation environments used in this work. Note that the data domain and resolution do not correspond with the computational domain and resolution.

| **Environment reference** | **SOWFA, high-res** | **SOWFA, low-res** | **EllipSys3D** |
|---|---|---|---|
| **Solver** | SOWFA | SOWFA | EllipSys3D |
| **Inflow** | Uniform | Uniform | Turbulent |
| **Turbulence intensity** | $0\%$ | $0\%$ | $\approx 6\%$ |
| **Inflow wind speed** | $9[m/s]$ | $9[m/s]$ | $8[m/s]$ |
| **ABL shear layer** | No | No | Yes |
| **Wind turbine** | DTU 10 MW | DTU 10 MW | 2.3 MW |
| **Rotor diameter** | $178.3[m]$ | $178.3[m]$ | $96.2[m]$ |
| **Pressure available** | No | Yes | No |
| **Data spatial domain** | $0-12D$ | $0-9D$ | $0-10D$ |
| **Data spatial resolution** | $12.5[m]$ | $12.5[m]$ | $1.77[m]$ |
| **Data temporal resolution** | $2[s]$ | $2[s]$ | $0.5[s]$ |

The cases are shown in table 3.2. A baseline case is solved and analysed in all three environments. This creates insight into the phenomena naturally occurring in a wind turbine wake under uniform and turbulent inflow conditions. The different inflow signals provide diverse data, which is desirable for validating the method for the transport of kinetic energy.

A dynamic induction control case is computed in the SOWFA environment with high resolution and low resolution. For the high-resolution environment, pressure data is lacking, whereas for the low-resolution environment, that data is available. This allows an evaluation of whether or not the relatively low resolution is sufficient to capture the dynamic phenomena. Two additional dynamic induction control cases are evaluated in the SOWFA low-resolution environment, with different actuation frequencies.

Finally, two cases with a different constant blade pitch setting at $\theta = 4^o$ and $\theta = -4^o$ are evaluated in the SOWFA low-resolution environment. This gives insight into the steady-state wake at the peaks of the actuation signal. Interestingly, these cases are computed by allowing the flow to settle with a baseline blade pitch setting $\theta = 0$. Then, the blade pitch settings is instantly changed to $\theta = 4^o$ or $\theta = -4^o$. This provides additional information on the settling behaviour of the wake under changing blade pitch settings.

Table 3.2: Overview of the simulation cases analysed in this work. Control cases indicated with a Strouhal number are controlled by applying a sine wave with a frequency corresponding to the indicated Strouhal number and amplitude of $4^o$ on the blade pitch $\theta$.

| **SOWFA, high-res** | | **SOWFA, low-res** | | **EllipSys3D** | |
|---|---|---|---|---|---|
| **Case reference** | **Control** | **Case reference** | **Control** | **Case reference** | **Control** |
| uni_high_base | Baseline | uni_low_base | Baseline | turb_base | Baseline |
| uni_high_0.25 | St = 0.25 [-] | uni_low_0.25 | St = 0.25 [-] | | |
| | | uni_low_0.20 | St = 0.2 [-] | | |
| | | uni_low_0.30 | St = 0.3 [-] | | |
| | | uni_low_theta_4 | $\theta = 4^o$ | | |
| | | uni_low_theta_-4 | $\theta = -4^o$ | | |

## 3.1. Uniform inflow

The settings for the cases with uniform inflow simulated in SOWFA will be discussed here. A DTU 10 MW wind turbine as described by Bak et al. (2013) is simulated for a uniform inflow of $9[m/s]$. A baseline control case and a dynamic induction control case at $St = 0.25[-]$ are computed in the high-resolution framework. The run-time for one case

with the spatial and temporal resolution for this framework, including post-processing, is approximately two weeks. A baseline control case, three dynamic induction control cases at $St = [0.2, 0.25, 0.3][-]$ and two cases evaluating different baseline control pitch settings are computed with a lower spatial and temporal resolution. Their run-time, including post-processing, is approximately three days.

### 3.1.1. High resolution

The computational mesh for the high resolution cases is described in table 3.3 and shown in fig. 3.1. Some quick calculations are shown here to support the chosen simulation parameters.

Table 3.3: Grid resolution for the SOWFA cases with high resolution.

| | X [m] | Y [m] | Z [m] | Cell size [m] |
|---|---|---|---|---|
| Original | [0 2500] | [0 1000] | [0 600] | 50 |
| Refinement 1 | [200 2500] | [200 800] | [0 460] | 25 |
| Refinement 2 | [220 2480] | [220 780] | [0 420] | 12.5 |
| Refinement 3 | [250 2390] | [250 750] | [0 400] | 6.25 |
| Refinement 4 | [280 2230] | [270 730] | [0 350] | 3.125 |

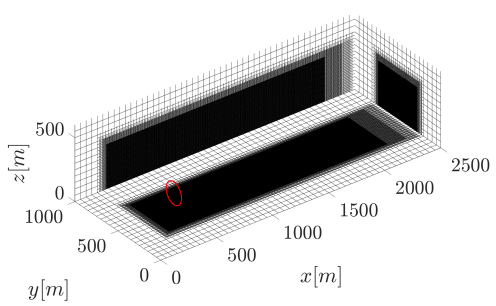


(a) Isometric view.

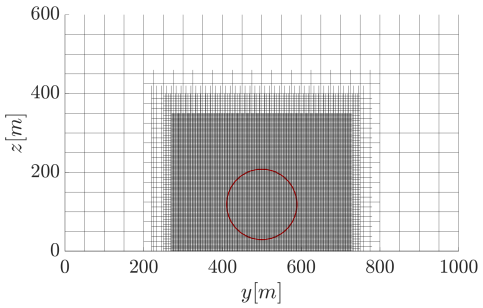


(b) Front view.

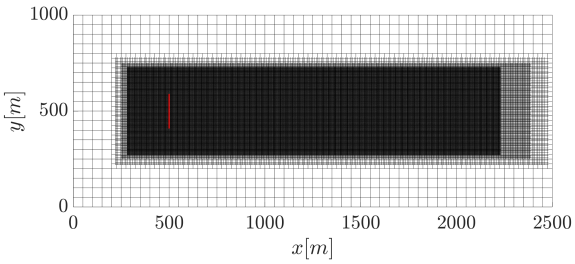


(c) Top view.

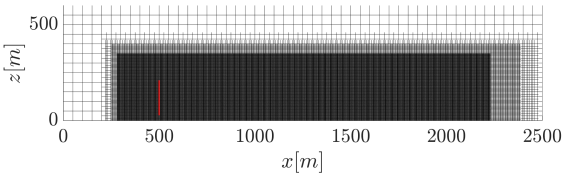


(d) Side view.

Figure 3.1: Mesh visualization for the computational grid for the SOWFA cases with high resolution. The red circle indicates the rotor area.

#### Transient

The fastest flow-through time of the domain is $\frac{|x|}{u_\infty} = \frac{2500[m]}{9m/s]} = 278[s]$. The slowest flow-through time, assuming a perfect kinetic energy extraction with an axial induction factor of $a = 1/3[-]$, and no recovery of wind speed, is: $\frac{L_x}{U_\infty(1-2a)} = \frac{2500[m]}{9(1-2\cdot1/3)[m/s]} = 833[s]$. First, the simulation is run for $1000[s]$ to let the wake develop. Then, the

simulation is run for another $4000[s]$ to collect data. Data is only stored after $t = 1000[s]$. The development of the flow is checked in section 5.1.1 to make sure the transient is resolved.

**Blockage ratio**
The chosen domain leads to a blockage ratio of $\frac{A_{rotor}[m^2]}{A_{domain}[m^2]} = \frac{\pi R^2}{L_y \cdot L_z} = 0.04[-]$. This is below but close to the value of $0.05$ suggested by Sarlak et al. (2016) as the lower limit of where blockage effects can be expected. The flow velocity near the edge of the domain is checked in section 5.1.1 to make sure blockage effects are limited.

**Time step**
The DTU 10 MW has a maximum design rotational velocity of $\Omega = 1.005[rad/s]$, which can also be expressed as $0.16[Hz]$ or $St = 3.17[-]$. The shortest time it takes for a rotor tip to travel through one cell is then: $\frac{L_{cell}}{\Omega \cdot R} = 0.03[s]$. However, the cases are simulated at below-rated wind speeds at $u_\infty = 9[m/s]$. Therefore, the rotor is operating at a lower rotational velocity, and the shortest time it takes for a rotor tip to travel through one cell is expected to be $0.04[s]$. The time-step for the simulation is chosen to be $\Delta t = 0.04[s]$.

**Data availability**
Data is collected from the domain corresponding to Refinement 4 in table 3.3 with a uniform cell size of $3.125[m]$. Data from 4000 seconds of simulated time is collected. The turbine data is stored at $25[Hz]$. Flow data is stored at $0.5[Hz]$. This gives a very large dataset that is hard to work with. The size of the dataset is reduced by selecting every $4^{th}$ spatial component, giving a spatial resolution of $12.5[m]$ in the $x$, $y$ and $z$ directions.

**Cell size**
Solving with a cell size of $3.125[m]$ with the DTU 10 MW radius of $89.17[m]$ leads to $\frac{89.17[m]}{3.125[-]} = 29[-]$ cells per blade. This is similar to the 25 cells per blade used by Sørensen et al. (2015) and should be sufficient to resolve the tip vortices. However, it might no longer be possible to see the tip vortices in the available data on account of decimating the data. This is checked in chapter 5.

**Dynamic induction control**
A sinusoidal feed-forward signal is applied on the blade pitch $\theta$ with an amplitude of $4^o$ and with a frequency of $St = 0.25[-]$ or $f = \frac{St \cdot u_\infty}{D} = 0.0126[Hz]$ as found to be an effective DIC frequency by Frederik et al. (2020a).

### 3.1.2. Low resolution

The computational mesh for the low resolution cases is described in table 3.4. The highest spatial resolution is the same as in the high-resolution case, but the refinements occur closer to the wake. A time-step $\Delta t = 0.2$ is used, $5$ times that of the high-resolution case. This means that the rotor tip will travel through multiple cells in one time-step, providing less accurate results close to the rotor plane. The effect of this is evaluated in chapter 7.

Table 3.4: Grid resolution for the SOWFA cases with low resolution.

| | X [m] | Y [m] | Z [m] | Cell size [m] |
|---|---|---|---|---|
| **Original** | [0 2500] | [0 1000] | [0 600] | 50 |
| Refinement 1 | [200 2300] | [200 600] | [0 460] | 25 |
| Refinement 2 | [220 2200] | [220 560] | [0 420] | 12.5 |
| Refinement 3 | [250 2000] | [25 500] | [0 400] | 6.25 |
| Refinement 4 | [400 2500] | [315 370] | [0 330] | 3.125 |

## 3.2. Turbulent inflow

The results from the baseline control uniform inflow cases are compared to results from a turbulent inflow case. A dataset published by DTU[4] is used for this purpose. The dataset is described by Liew et al. (2020). A 2.3 MW wind turbine with a diameter of $D = 96.2[m]$ is simulated in EllipSys3D. Turbulence is generated using a Mann box, see Mann (1994) and Mann (1998), to achieve a turbulence intensity of approximately $6\%$. The atmospheric boundary layer is modelled according to the power law with a shear exponent of $\alpha = 0.14$. Further description of the numerical framework is provided by Sørensen et al. (2015).

The computational domain is $20R \times 20R \times 40R$ in the lateral, vertical and streamwise directions. Wind field slices are extracted every $1R$ behind the wind turbine for $1R-23R$. Additionally, a slice of the free-stream is available. Each blade is resolved by 27 cells. The available data mesh for the turbulent inflow case is shown in fig. 3.2.

Data is available with a time resolution of $0.12[s]$. This makes the data-set large and hard to work with, so only every fourth time snapshot is selected to reduce the time resolution to $0.5[Hz]$. The simulated wind turbine has a fixed rotor speed of $1.37[rad/s]$, $0.218[Hz]$ or $St = 2.62[-]$.

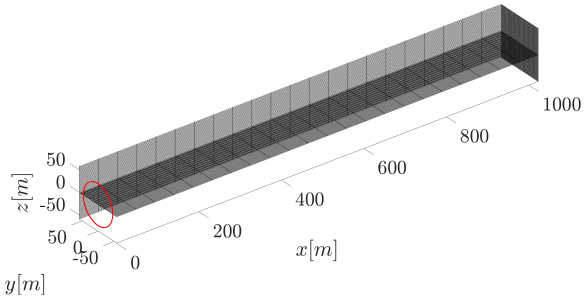


(a) Isometric view.

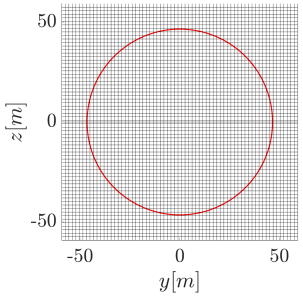


(b) Front view.

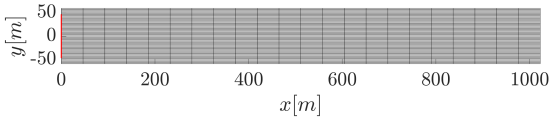


(c) Top view.

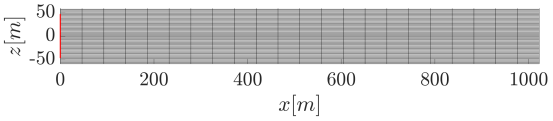


(d) Side view.

Figure 3.2: Mesh visualization for the available data points of case turb_base. The red circle indicates the rotor area.

[4]https://data.dtu.dk/articles/dataset/LES_of_wake_flow_behind_2_3MW_wind_turbine/12005421/1

# 4

# Deriving the transport of kinetic energy equations

Dynamic induction control aims to increase the wake recovery of a controlled wind turbine by transferring kinetic energy from the relatively high velocity surrounding flow to the relatively low-velocity wake. The transport of kinetic energy can be numerically described as a function of local flow quantities (velocity and pressure) by manipulating the Navier Stokes equations. Slightly different equations arise when applying this method to the instantaneous Navier Stokes equations and the Reynolds Averaged Navier Stokes Equations. Both approaches are theoretically described by Pope (2000). The Reynolds Averaged Navier Stokes approach is applied to experimental data of a wind turbine in turbulent inflow conditions with baseline control by Newman et al. (2014) and simulated data by Andersen et al. (2017), and to a yawed wind turbine by Houtin—Mongrolle et al. (2021).

The instantaneous and Reynolds Averaged Navier Stokes approach are applied and compared in this work. The RANS approach has seen much use in literature, which will provide a good means to validate the method. The instantaneous approach will provide insight into the dynamic behaviour of the various transport of kinetic energy components. The application of the instantaneous Navier Stokes energy equation is a novel approach to describe the time behaviour of kinetic energy transport in the context of dynamic induction control.

This chapter will start by deriving the instantaneous and Reynolds Averaged Navier Stokes energy equation. Then, the control volume approach is explained. Finally, the numerical implementation of the equations is discussed.

## 4.1. Deriving the kinetic energy equations

**Instantaneous kinetic energy equation**
Recalling the incompressible Navier Stokes momentum equations eq. (2.5):

$$\frac{\partial u_i}{\partial x_i} = 0$$

$$\underbrace{\frac{\partial u_j}{\partial t}}_{\text{Acceleration term}} + \underbrace{u_i \frac{\partial u_j}{\partial x_i}}_{\text{Advection term}} = - \underbrace{\frac{1}{\rho}\frac{\partial p}{\partial x_j}}_{\text{Pressure term}} + \underbrace{\nu \frac{\partial^2 u_j}{\partial x_i \partial x_i}}_{\text{Viscous term}} \tag{4.1}$$

The viscous term can be rewritten using the continuity equation:

$$\nu\frac{\partial^2 u_j}{\partial x_i \partial x_i} = \nu\frac{\partial^2 u_j}{\partial x_i \partial x_i} + \nu\frac{\partial}{\partial x_j}\left(\underbrace{\frac{\partial u_i}{\partial x_i}}_{=0}\right) = \nu\frac{\partial}{\partial x_i}\left(\frac{\partial u_i}{\partial x_j} + \frac{\partial u_j}{\partial x_i}\right) = 2\nu\frac{\partial S_{ij}}{\partial x_i}, \tag{4.2}$$

to include the strain rate tensor $S_{ij}$:

$$S_{ij} = \frac{1}{2}\left(\frac{\partial u_i}{\partial x_j} + \frac{\partial u_j}{\partial x_i}\right) \tag{4.3}$$

The energy equation can be obtained from the Navier Stokes momentum equation by multiplying with $u_j$. The kinetic energy of the fluid, per unit mass, is:

$$E = \frac{1}{2}u_j \cdot u_j \tag{4.4}$$

The product rule can be used to find the correct energy terms:

$$\begin{aligned} \frac{\partial E}{\partial t} &= \frac{\partial}{\partial t}\left(\frac{1}{2}u_j u_j\right) = \frac{1}{2}\left(u_j\frac{\partial u_j}{\partial t} + u_j\frac{\partial u_j}{\partial t}\right) = u_j\frac{\partial u_j}{\partial t} \\ u_i\frac{\partial E}{\partial x_i} &= u_i\frac{\partial}{\partial x_i}\left(\frac{1}{2}u_j u_j\right) = \frac{1}{2}u_i\left(u_j\frac{\partial u_j}{\partial x_i} + u_j\frac{\partial u_j}{\partial x_i}\right) = u_j u_i\frac{\partial u_j}{\partial x_i}, \end{aligned} \tag{4.5}$$

and to find the correct pressure and viscous terms:

$$\begin{aligned} \frac{\partial}{\partial x_j}\left(\frac{u_j p}{\rho}\right) &= u_j\frac{1}{\rho}\frac{\partial p}{\partial x_j} + \frac{p}{\rho}\underbrace{\frac{\partial u_j}{\partial x_i}}_{=0} = u_i\frac{1}{\rho}\frac{\partial p}{\partial x_i} \\ \frac{\partial}{\partial x_i}\left(2\nu u_j S_{ij}\right) &= 2\nu S_{ij}\frac{\partial u_j}{\partial x_i} + 2\nu u_j\frac{\partial S_{ij}}{\partial x_i} = 2\nu u_j\frac{\partial S_{ij}}{\partial x_i} + \epsilon, \end{aligned} \tag{4.6}$$

where it is used that $\frac{\partial u_i}{\partial x_j} = \frac{\partial u_j}{\partial x_i}$ to find the viscous dissipation $\epsilon$:

$$2\nu S_{ij}\frac{\partial u_j}{\partial x_i} = \nu\left(S_{ij}\frac{\partial u_i}{\partial x_j} + S_{ij}\frac{\partial u_j}{\partial x_i}\right) = \nu S_{ij}\left(\underbrace{\frac{\partial u_i}{\partial x_j} + \frac{\partial u_j}{\partial x_i}}_{2S_{ij}}\right) = 2\nu S_{ij}S_{ij} = \epsilon \tag{4.7}$$

Finally, the instantaneous energy equation can be found by multiplying the Navier Stokes equations with $u_j$:

$$\begin{aligned} u_j\frac{\partial u_j}{\partial t} + u_j u_i\frac{\partial u_j}{\partial x_i} &= -u_j\frac{1}{\rho}\frac{\partial p}{\partial x_j} + u_j 2\nu\frac{\partial S_{ij}}{\partial x_i} \\ \underbrace{\frac{\partial E}{\partial t}}_{\text{Change of energy in time}} + \underbrace{u_i\frac{\partial E}{\partial x_i}}_{\text{Advection of energy}} &= -\frac{\partial}{\partial x_i}\left(\underbrace{u_i\frac{p}{\rho}}_{\text{Pressure work}} - \underbrace{2\nu u_j S_{ij}}_{\text{Viscous transport}}\right) - \underbrace{\epsilon}_{\text{Viscous dissipation}} \\ \underbrace{\frac{DE}{Dt}}_{\text{Material derivative}} &= -\nabla\cdot T_i - \epsilon \end{aligned} \tag{4.8}$$

where the instantaneous flux of energy $T_i$ is:

$$T_i = u_i \frac{p}{\rho} - 2\nu u_j S_{ij} \tag{4.9}$$

The time rate of change of the energy can now be expressed as a function of the pressure work, viscous transport and viscous dissipation. The material derivative notation is the notation used by Pope (2000).

**Mean kinetic energy equation**
Recalling the Reynolds Averaged Navier Stokes equations eq. (2.7):

$$\langle u_i \rangle \frac{\partial \langle u_j \rangle}{\partial x_i} = -\frac{1}{\rho}\frac{\partial \langle p \rangle}{\partial x_j} + 2\nu \frac{\partial \langle S_{ij} \rangle}{\partial x_i} - \frac{\partial \langle u_i' u_j' \rangle}{\partial x_i} \tag{4.10}$$

The equations for the mean kinetic energy $\langle E \rangle$ and turbulent kinetic energy $\langle k \rangle$ are:

$$\begin{aligned} \langle E \rangle &= \frac{1}{2}\langle u_j \rangle \cdot \langle u_j \rangle \\ \langle k \rangle &= \frac{1}{2}\langle u_j'^2 \rangle \end{aligned} \tag{4.11}$$

$\langle E \rangle$ can be found by multiplying the Reynolds Averaged Navier Stokes equations with $\langle u_j \rangle$:

$$\begin{aligned} \langle u_j \rangle \langle u_i \rangle \frac{\partial \langle u_j \rangle}{\partial x_i} &= -\langle u_j \rangle \frac{1}{\rho}\frac{\partial \langle p \rangle}{\partial x_j} + \langle u_j \rangle 2\nu \frac{\partial \langle S_{ij} \rangle}{\partial x_i} - \langle u_j \rangle \frac{\partial \langle u_i' u_j' \rangle}{\partial x_i} \\ \underbrace{\langle u_i \rangle \frac{\partial \langle E \rangle}{\partial x_i}}_{\text{Advection of energy}} &= -\frac{\partial}{\partial x_i}\left( \underbrace{\langle u_i \rangle \frac{\langle p \rangle}{\rho}}_{\text{Pressure work}} - \underbrace{2\nu \langle u_j \rangle \langle S_{ij} \rangle}_{\text{Viscous transport}} + \underbrace{\langle u_i \rangle \langle u_i' u_j' \rangle}_{\text{Reynolds stress work}} \right) - \underbrace{\mathcal{P}}_{\text{Production of TKE}} - \underbrace{\epsilon}_{\text{Viscous dissipation}} \\ \frac{D\langle E \rangle}{Dt} &= -\nabla \cdot \langle T_i \rangle - \mathcal{P} - \epsilon \end{aligned} \tag{4.12}$$

where it is now also used that:

$$\frac{\partial}{\partial x_i}\left( \langle u_j \rangle \langle u_i' u_j' \rangle \right) = \langle u_j \rangle \frac{\partial \langle u_i' u_j' \rangle}{\partial x_i} + \underbrace{\langle u_i' u_j' \rangle \frac{\partial \langle u_j \rangle}{\partial x_i}}_{-\mathcal{P}} = \langle u_j \rangle \frac{\partial \langle u_i' u_j' \rangle}{\partial x_i} - \mathcal{P} \tag{4.13}$$

The production of turbulent kinetic energy $\mathcal{P}$ term describes the transfer of energy from the mean flow field to the turbulent fluctuations:

$$\mathcal{P} = -\langle u_i' u_j' \rangle \frac{\partial \langle u_j \rangle}{\partial x_i} \tag{4.14}$$

The time-averaged flux of energy $\langle T_i \rangle$ now also includes the Reynolds stress work:

$$\langle T_i \rangle = \langle u_i \rangle \frac{\langle p \rangle}{\rho} - 2\nu \langle u_i \rangle \langle S_{ij} \rangle + \langle u_i \rangle \langle u_i' u_j' \rangle \tag{4.15}$$

## 4.2. Control volume

The kinetic energy equation for the instantaneous Navier Stokes equations and Reynolds Averaged Navier Stokes equations have now been derived. However, the quantity of interest is the kinetic energy flux from the surrounding flow into the wake. A control volume approach will be followed, with the control volume defined as shown in fig. 4.1a. A cylinder parallel to the rotor plane, with diameter $D$, length $dx$ and distance downstream of the rotor plane $x$ is examined.

Note that this approach is different from the one proposed by Houtin—Mongrolle et al. (2021), where the control volume boundaries are defined by a streamtube. The main reason for this is of practical nature: the cylindrical control volume proposed here is easier to compute. Additionally, the wind speed in a cylindrical control volume with a diameter $D$ can be directly related to the power production of a hypothetical downstream wind turbine located in that control volume.

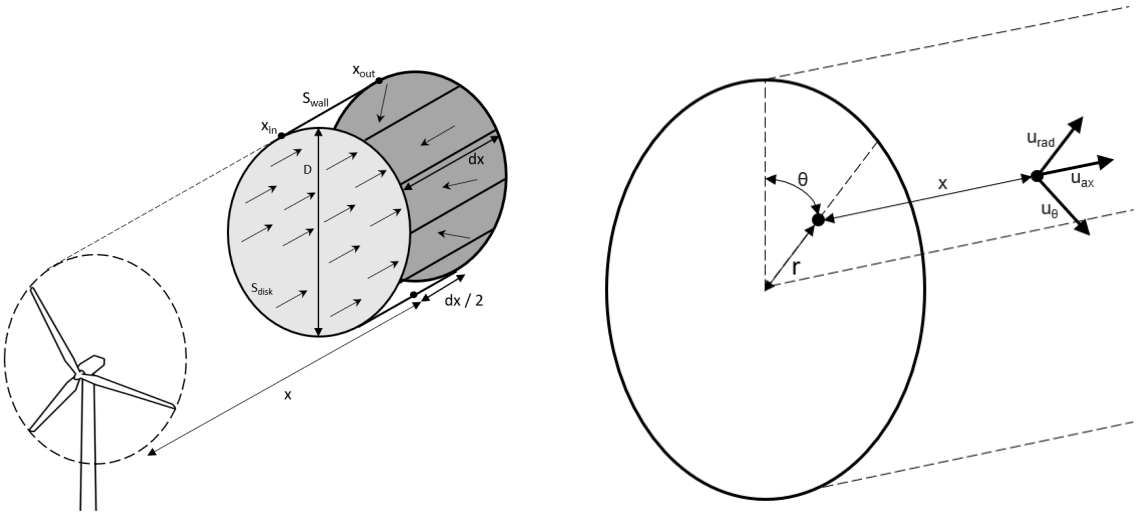


(a) Control volume.

(b) Cylindrical coordinate system.

Figure 4.1: Wake diagrams.

Applying a volume integral over the control volume for the instantaneous energy equation and applying Gauss's theorem:

$$\begin{aligned} \iiint_{\mathcal{V}} \left(\frac{\partial E}{\partial t}\right) d\mathcal{V} + \iiint_{\mathcal{V}} \left(u_i \frac{\partial E}{\partial x_i}\right) d\mathcal{V} &= -\iiint_{\mathcal{V}} \left(\frac{\partial}{\partial x_i}\left(T_i\right)\right) d\mathcal{V} - \iiint_{\mathcal{V}} \left(\epsilon\right) d\mathcal{V} \\ \iiint_{\mathcal{V}} \left(\frac{\partial E}{\partial t}\right) d\mathcal{V} + \oiint_{\mathcal{S}} \left(u_i E \cdot \hat{n}\right) d\mathcal{S} &= -\oiint_{\mathcal{S}} \left(T_i \cdot \hat{n}\right) d\mathcal{S} - \iiint_{\mathcal{V}} \left(\epsilon\right) d\mathcal{V} \end{aligned} \tag{4.16}$$

Similarly, applying the control volume and Gauss's theorem on the Reynolds Averaged Navier Stokes energy equation this results in:

$$\oiint_{\mathcal{S}} \left(\langle u_i \rangle \langle E \rangle \cdot \hat{n}\right) d\mathcal{S} = -\oiint_{\mathcal{S}} \left(\langle T_i \rangle \cdot \hat{n}\right) d\mathcal{S} - \iiint_{\mathcal{V}} \left(\mathcal{P}\right) d\mathcal{V} - \iiint_{\mathcal{V}} \left(\epsilon\right) d\mathcal{V} \tag{4.17}$$

**Power increase over control volume**

A cylindrical coordinate system is chosen as shown in fig. 4.1b. The cylindrical coordinate system is convenient as the velocities can be easily expressed in components normal to the control volume surfaces: $u_{ax}$ is normal to the disk

surface, and $u_{rad}$ is normal to the cylinder wall surface. The remaining velocity component, $u_\theta$, has no component normal to the control volume surface and will disappear from the derivation. Applying this, the surface integral can be decomposed into the surface of the disk and the surface of the wall. For example, decomposing the energy advection term from the instantaneous Navier Stokes energy equation:

$$\oiint_{\mathcal{S}} (u_i E \cdot \hat{n})\, d\mathcal{S} = \underbrace{\oiint_{\mathcal{S}_{disk}} (u_{ax} E \cdot \hat{n})\, d\mathcal{S}_{disk}}_{\text{Power increase over control volume}} + \underbrace{\oiint_{\mathcal{S}_{wall}} (u_{rad} E \cdot \hat{n})\, d\mathcal{S}_{wall}}_{\text{Advection flux through cylinder wall}} \tag{4.18}$$

Further examining the first term on the R.H.S., and considering the energy and power per unit mass:

$$\begin{aligned} E &= \frac{1}{2}u^2 \\ P &= \frac{1}{2}Au^3 = EAu, \end{aligned} \tag{4.19}$$

it can be seen that the first term on the R.H.S. evaluates the power per unit mass at the disk surface entering the volume and at the disk surface leaving the volume. The difference is the power increase over the control volume. Linking this to the image of the control volume in fig. 4.1a, this can be computed as:

$$\underbrace{\oiint_{\mathcal{S}_{disk}} (u_{ax} E \cdot \hat{n})\, d\mathcal{S}_{disk}}_{\text{Power increase over control volume}} = \underbrace{\oiint_{\mathcal{S}_{disk}} (u_{ax} E)\, d\mathcal{S}_{disk}\Big|_{x_{out}}}_{\text{Power leaving the control volume}} - \underbrace{\oiint_{\mathcal{S}_{disk}} (u_{ax} E)\, d\mathcal{S}_{disk}\Big|_{x_{in}}}_{\text{Power entering the control volume}} \tag{4.20}$$

The negative sign at $x_{in}$ comes from $u_{ax}$ moving in the negative direction of the normal of the disk surface, while it acts along the normal of the surface at $x_{out}$.

**Decomposing surface integral**

Decomposing all surface integrals into components normal to the disk surface and components normal to the wall surface, the power increase over the control volume can be found as a function of work done on the surface of the control volume for the instantaneous Navier Stokes energy equation:

$$\begin{aligned} \iiint_{\mathcal{V}} \left(\frac{dE}{dt}\right) d\mathcal{V} + \oiint_{\mathcal{S}_{disk}} (u_{ax} E \cdot \hat{n})\, d\mathcal{S}_{disk} = &\oiint_{\mathcal{S}_{disk}} (-T_{ax} \cdot \hat{n})\, d\mathcal{S}_{disk} \\ &+ \oiint_{\mathcal{S}_{wall}} (-u_{rad} E \cdot \hat{n} - T_{rad} \cdot \hat{n})\, d\mathcal{S}_{wall} \\ &- \iiint_{\mathcal{V}} (\epsilon)\, d\mathcal{V} \end{aligned} \tag{4.21}$$

Similarly for the RANS energy equation:

$$\begin{aligned} \oiint_{\mathcal{S}_{disk}} (\langle u_{ax}\rangle \langle E\rangle \cdot \hat{n})\, d\mathcal{S} = &\oiint_{\mathcal{S}_{disk}} (-\langle T_{ax}\rangle \cdot \hat{n})\, d\mathcal{S}_{disk} \\ &+ \oiint_{\mathcal{S}_{wall}} (-\langle u_{rad}\rangle \langle E\rangle \cdot \hat{n} - \langle T_{rad}\rangle \cdot \hat{n})\, d\mathcal{S}_{wall} \\ &- \iiint_{\mathcal{V}} (\mathcal{P})\, d\mathcal{V} - \iiint_{\mathcal{V}} (\epsilon)\, d\mathcal{V} \end{aligned} \tag{4.22}$$

## 4.3. Numerical implementation

**Neglecting terms**

Using data points generated by a Large Eddy Simulation, such as in this work, flow quantities (velocity and pressure) are spatially filtered. This introduces the sub-filter scale stress tensor $\tau_{ij}$. Additionally, applying the actuator line method to model the wind turbine blade, a body force $f_i$ is introduced.

$$\frac{\partial \tilde{u}_j}{\partial t} + \frac{\partial \tilde{u}_i \tilde{u}_j}{\partial x_i} = -\frac{1}{\rho}\frac{\partial \tilde{p}}{\partial x_i} + \nu \frac{\partial^2 \tilde{u}_j}{\partial x_i \partial x_i} - \underbrace{\frac{\partial \tau_{ij}}{\partial x_i}}_{\text{Sub-filter scale stress tensor}} + \underbrace{\tilde{f}_i}_{\text{Rotor force}} \tag{4.23}$$

The results will show that not taking into account the rotor force results in a large error in the rotor plane. However, the resolution in the data-set does not allow correctly implementing $f_i$.

The sub-filter scale stress tensor is not taken into account. Additionally, the viscous terms are not taken into account. The viscous terms and sub-filter scale stress tensor will have a small influence, taken into account by computing the residual of the remaining terms. The results show that this residual is small, so not taking these terms into account is valid. This approach is also applied by Houtin—Mongrolle et al. (2021).

The total residual for the instantaneous Navier Stokes energy equation is then:

$$\text{residual} = \frac{\partial}{\partial x_i}\left(-2\nu u_j S_{ij}\right) - \frac{\partial \tau_{ij}}{\partial x_i} + u_j f_j - \epsilon \tag{4.24}$$

and for the Reynolds Averaged Navier Stokes energy equation:

$$\text{residual} = \frac{\partial}{\partial x_i}\left(-2\nu \langle u_j \rangle \langle S_{ij} \rangle\right) - \frac{\partial \tau_{ij}}{\partial x_i} + \langle u_j \rangle \langle f_j \rangle - \epsilon \tag{4.25}$$

**Spatial gradient of power**

Dividing the power increase over the control volume by the length of the control volume $dx$, the spatial gradient of power $\frac{\partial P}{\partial x}$ can be found. In this work, the spatial gradient of power is non-dimensionalised by rotor diameter $D$, so the gradient is evaluated in power per rotor diameter. This allows for comparison between the simulation environments.

The disk surface integrals can be divided by $dx$. The wall surface integrals effectively change into contour integrals. The contour integrals are evaluated by interpolating the flow parameters at $40$ locations along the disk wall contour, averaging and multiplying by the disk circumference.

# 5

# Analysis of flow dynamics

An analysis of dynamic phenomena occurring in the wake of a wind turbine with baseline control under uniform and turbulent inflow conditions is performed. The reason for the baseline analysis is twofold: firstly, the analysis tools are validated. Secondly, to find aerodynamic phenomena naturally occurring in the wake that might interact with the dynamics caused by dynamic induction control. Then, the wake of a wind turbine actuated with sinusoidal dynamic induction control at an actuation frequency of $St = 0.25[-]$ with an amplitude of $\theta = 4^o$ is analysed. Uniform inflow conditions are used for this analysis, in order to be able to differentiate the dynamics occurring from exciting the blade pitch from naturally occurring dynamics.

The analysis is performed by investigating the mean and instantaneous flow parameters of velocity and pressure. Additionally, the regions dominated by vorticity are investigated using the Q-criterion. Finally, the flow is analysed using Proper Orthogonal Decomposition to show the dominating spatial and temporal modes and their relative energy distribution.

## 5.1. Baseline control, uniform inflow

This section shows an analysis of the phenomena occurring in the wake of a turbine with baseline control under uniform inflow conditions. The cases used to perform this analysis are uni_base_high and uni_base_low.

### 5.1.1. General flow overview

**Transient**

To describe the transient behaviour of the LES simulation, the time evolution of the spatial average of circular slices with rotor diameter $D$ parallel to the rotor plane, separated $2D$, is shown in fig. 5.1. The solution stabilizes after approximately $1500s$. From here on, data with $t > 2000s$ is used for analysis.

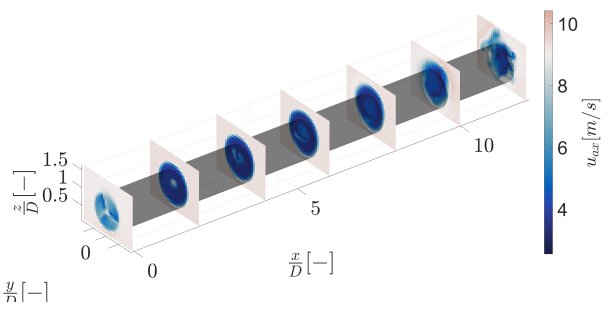


(a) Slices showing contour plots of the instantaneous streamwise velocity at $t = 5000[s]$. The transparent cylinder indicates the rotor plane cylinder, the area of spatial averaging.

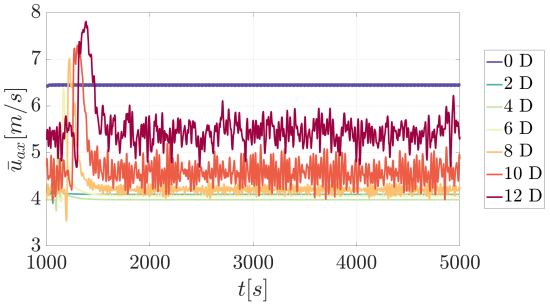


(b) Instantaneous streamwise velocity averaged over a rotor plane cylinder slice.

Figure 5.1: Transient behaviour of the streamwise velocity for case uni_high_base.

### High-velocity region downstream of nacelle

A vertical slice of the mean streamwise velocity at the center of the rotor-plane $y = 0$ is shown in fig. 5.2. The effect of the rotor on the velocity results in a velocity deficit in the regions inside the rotor radius and outside the nacelle radius. Immediately downstream of the nacelle, there is no velocity deficit. This region will be referred to as the nacelle wake. This is a result of the applied rotor model in the simulation, and not physical. Churchfield et al. (2015) discuss that even though this rotor model is commonly applied, the nacelle wake causes interactions with the rotor wake that affect the wake breakdown and meandering behaviour of the wind turbine wake.

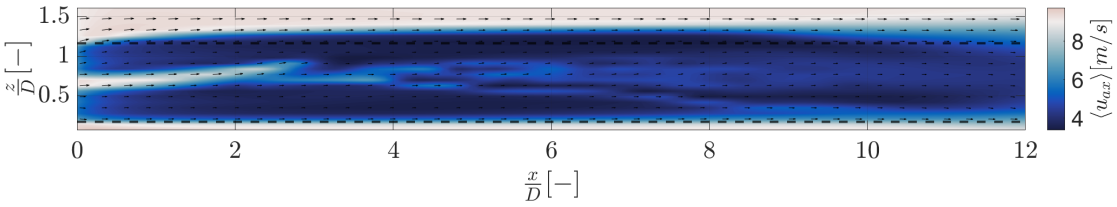


Figure 5.2: Vertical slice of the mean streamwise velocity at $y = 0$ for case uni_high_base. The dotted lines indicate the rotor plane cylinder. The quiver arrows indicate the local flow direction in the $[x\,z]$-plane.

### Speed-up behaviour near wall

Streamwise mean velocity profiles of vertical lines at various distances downstream of the rotor are shown in fig. 5.3. This figure also shows there is no velocity deficit immediately downstream of the nacelle. The velocity deficit is distributed over space until it assumes an approximately Gaussian profile in the far wake.

The flow accelerates to faster than the free-stream wind speed near the domain boundaries. This can be explained by the relatively high blockage ratio. Because this effect remains near the domain boundaries, the results of this simulation can be assumed valid, at least in a qualitative manner.

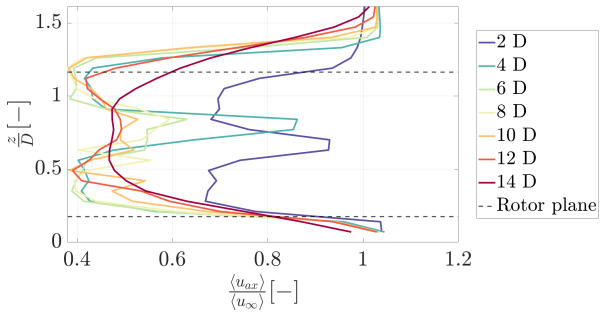


Figure 5.3: Time-averaged streamwise velocity profiles of a vertical line at $y = 0$ at various distances downstream for case uni_high_base.

**Coherent structure in the far-wake**

An instantaneous snapshot of the streamwise velocity is shown in fig. 5.4, and an instantaneous snapshot of the Q-criterion is shown in fig. 5.5. A wave-like structure starts to appear at the interface between the wake and the free-stream. Inspection of the Q-criterion isosurface reveals that the wave-like structure is of helical character.

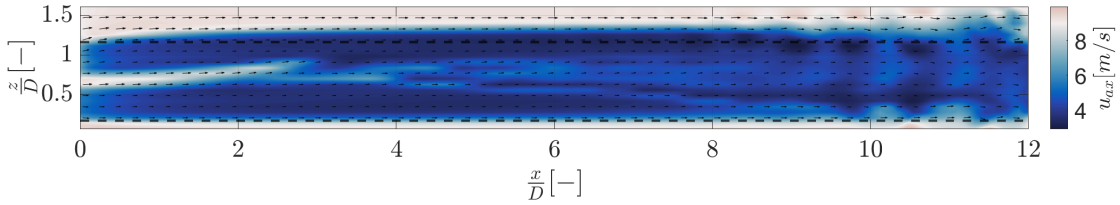


Figure 5.4: Vertical slice of the instantaneous streamwise velocity at $y = 0$ at $t = 5000[s]$ for case uni_high_base.

While the computational data has a resolution that should adequately describe the tip vortices, they can not be individually identified in fig. 5.5, but are smeared out. This is because a decimated data set is used.

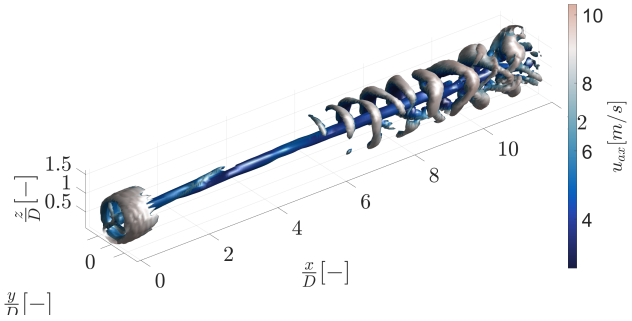


Figure 5.5: Isosurface of the Q-criterion where $Q = 0.0005$, colored by the local streamwise velocity, at $t = 5000[s]$ for case uni_high_base.

The wave-like structure, growing in space and time downstream of the wind turbine, combined with the case properties: an approximately step difference in the axial velocity over the interface between the wake and the free

stream, leads to the conjecture that a Kelvin Helmholtz Instability can be seen. Indeed, there are several mentions in literature of this phenomenon occurring in the wake of a wind turbine in uniform inflow simulations, such as in work by De Cillis et al. (2020).

The Kelvin Helmholtz Instability is an inertial instability that arises assuming ideal flow (incompressible, inviscid, irrotational flow) and performing a stability analysis on the basic flow configuration shown in fig. 5.6. The result of the stability analysis for these conditions is that any small perturbation of the interface shape will exponentially grow in space and time. This effect is well described by Kundu et al. (2015).

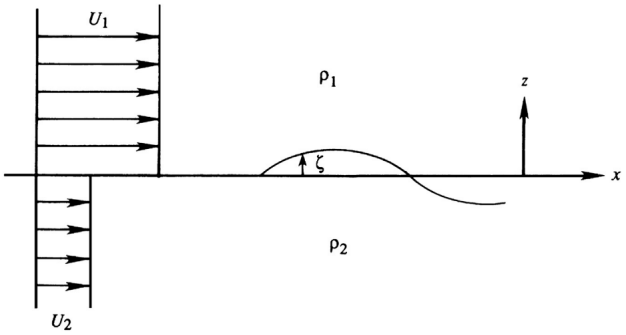


Figure 5.6: Basic flow configuration leading to the Kelvin-Helmholtz instability. Taken from Kundu et al. (2015).

### 5.1.2. Proper Orthogonal decomposition

Proper Orthogonal Decomposition is applied to give insight into the coherent spatial and temporal structures. Firstly, POD is applied on slices parallel to the rotor plane. Then, POD is applied to a vertical slice perpendicular to the rotor plane.

#### Parallel slices

Proper Orthogonal Decomposition is applied to slices parallel to the rotor plane. An advantage of this is that no assumptions are made about the same frequency being dominant throughout the wake. This gives insight into what frequency is dominant at varying distances downstream. The first seven spatial modes of vertical slices parallel to the rotor plane, separated $2D$, are shown in fig. 5.7. Their respective frequency spectra are shown in fig. 5.8. Finally, their respective relative energy is shown in fig. 5.9.

The mean mode, $r = 0$, is identical to the mean flow. The frequency of the mean mode is $f = 0$, so it is not included in the frequency spectra. The mean mode describes $> 95\%$ of the energy for the first $5D$, but decreases in energy after that. More modes are necessary to describe the dynamic phenomena in the flow. At $0D$, the modes are dominated by the induced velocity field by the rotor. The modes show distinct spatial structures. Modes $1$ and $2$ display six distinct regions around the rotor perimeter, modes $3$ and $4$ display 12 regions, modes $5$ and $6$ display 24 regions. The modes with the same number of regions are clearly paired. Note that the modes are orthogonal. They have the same number of regions but a slight spatial offset in the form of rotation. When considered in unison, the sinusoidal oscillations of the paired modes will add up to a rotating velocity field. A frequency peak at $3P$ or $St \approx 9[-]$ is expected. However, this frequency is not captured in the available data. Instead, the aliasing frequency at $St = 2.6[-]$ and the aliasing frequency of harmonics of the $3P$ frequency can be seen. At $2D$ and $4D$, a frequency peak at $St \approx 0.4[-]$ can be seen. At $4D$, this corresponds to modes $1$ and $2$. Inspecting the spatial modes reveals that these oscillations are related to turbulent fluctuations around the nacelle wake.

Starting at $2D$, and growing through the wake until $10D$, a dominant frequency of $St \approx 0.8$ arises. Inspecting the corresponding spatial modes reveals characteristic oscillating bands just outside the top of the rotor plane. These correspond to the oscillations caused by the Kelvin Helmholtz Instability. The Kelvin Helmholtz Instability theory states that a small oscillation will grow in space and time. This is indeed the behaviour that can be seen, where a small

oscillation that already exists at $2D$ grows into the dominant phenomenon in the wake. The peak of the relative energy of the modes related to the Kelvin Helmholtz Instability occurs around $9D$. Behind this distance, the coherent Kelvin Helmholtz Instability structure starts breaking up, and more modes are needed to describe the turbulent fluctuations in the wake.

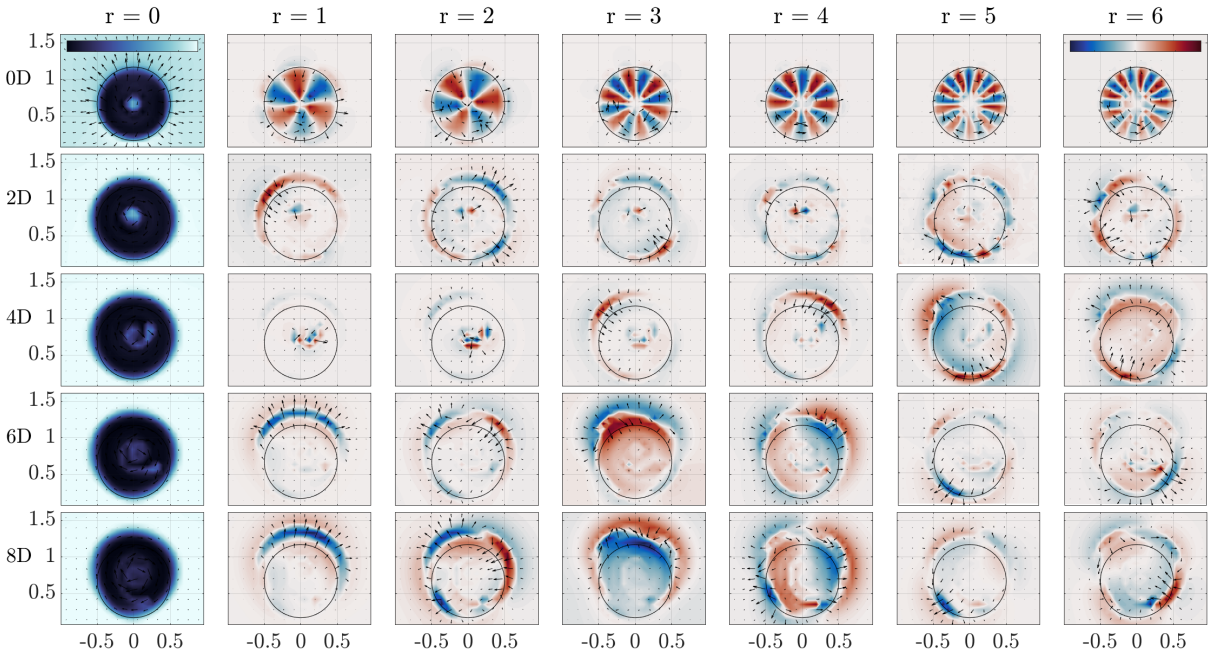


Figure 5.7: The first seven spatial modes of Proper Orthogonal Decomposition applied on the velocity field of vertical slices parallel to the rotor plane, separated $2D$ for case uni_high_base. The first mode $r = 0$ is the mean. The modes $r = 1, 2, \ldots, 6$ oscillate around the mean. The quiver arrows indicate the $v$ and $w$ components of the respective modes. The modes are used for qualitative analysis. Their magnitude is only taken into account in the frequency spectrum.

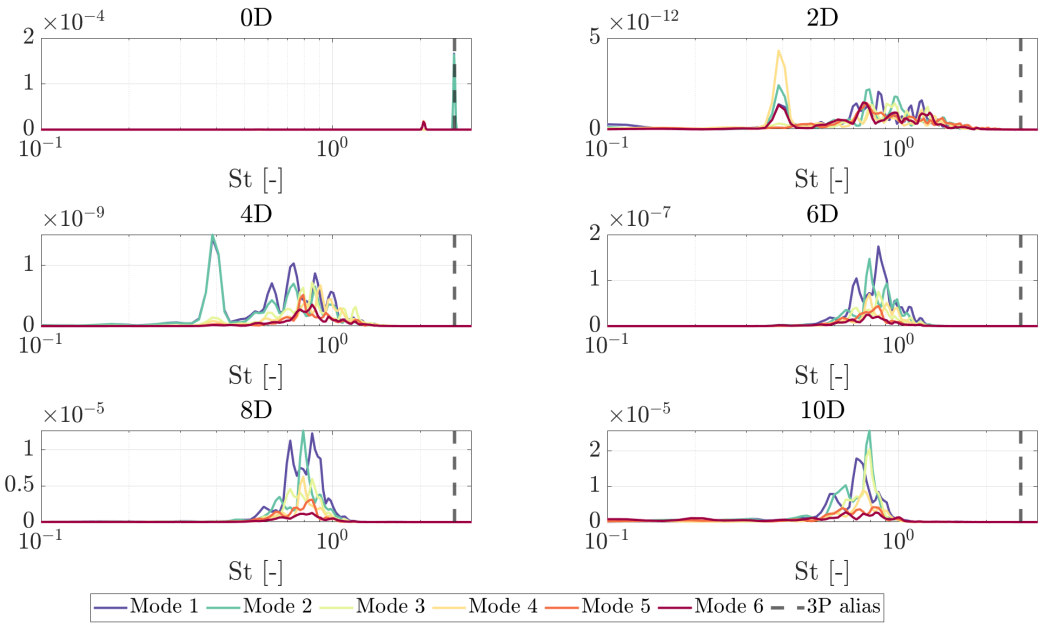


Figure 5.8: The frequency spectrum found by applying Welch's method on the first six temporal modes multiplied with their respective variance $\sigma$, excluding the mean mode, of Proper Orthogonal Decomposition performed on the velocity field of vertical slices parallel to the rotor plane, separated $2D$ for case uni_high_base.

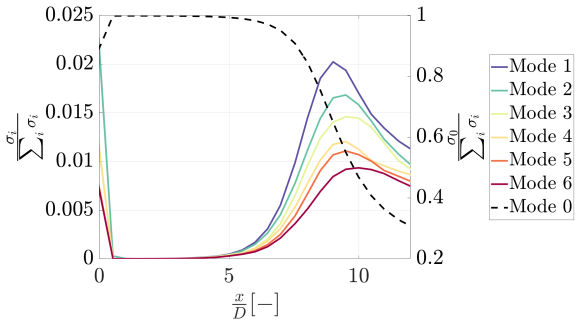


Figure 5.9: Relative energy of the first seven POD modes for case uni_high_base. The relative energy of the mean mode is much larger than the other modes and plotted on the right $y$-axis.

### Modal decomposition: vertical slices

Proper Orthogonal Decomposition is applied to a vertical slice perpendicular to the rotor plane. An advantage of this is that this gives insight into the most energetic spatial modes and their frequencies, taking into account the entire wake. The consecutive modes show the same spatial profile, with a slight spatial offset. When considered in unison, their sinusoidal oscillations add up to an oscillating velocity field. It becomes apparent that the Kelvin Helmholtz Instability creates an oscillating velocity in the wake with a frequency of $St \approx 0.8[-]$.

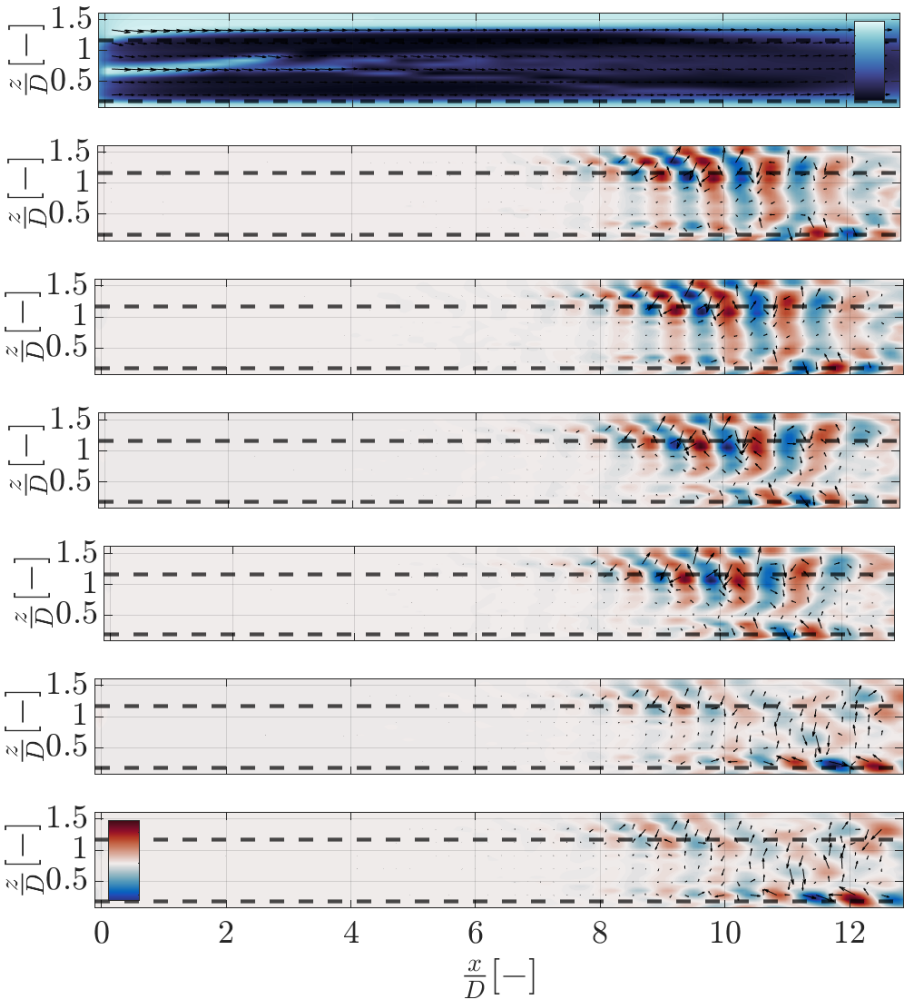


Figure 5.10: The first seven spatial POD modes for case uni_high_base. The first mode $r = 0$ is the mean. The modes $r = 1, 2, \ldots, 6$ oscillate around the mean. The quiver arrows indicate the $v$ and $w$ components of the respective modes. The modes are used for qualitative analysis, and their magnitude is only taken into account in the frequency spectrum.

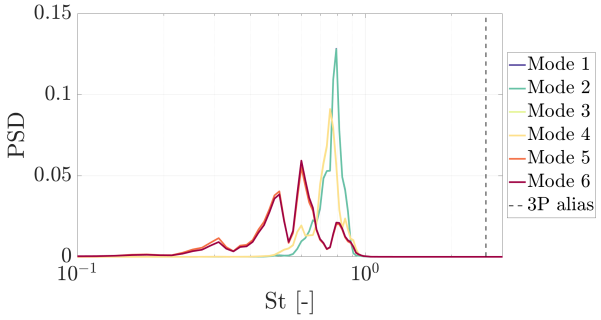


Figure 5.11: The frequency spectrum found by applying Welch's method on the first six temporal modes multiplied with their respective variance $\sigma$, excluding the mean mode.

## 5.2. Baseline control, turbulent inflow

### 5.2.1. General flow overview

This section shows an analysis of the phenomena occurring in the wake of a turbine with baseline control under turbulent inflow conditions. The case used to perform this analysis is turb_base.

**Transient**

To describe the transient behaviour of the LES simulation, the time evolution of the spatial average of circular slices with rotor diameter $D$ parallel to the rotor plane, separated $2D$, is shown in fig. 5.1. There is no transient behaviour to be seen, so the full time domain of the data can be used.

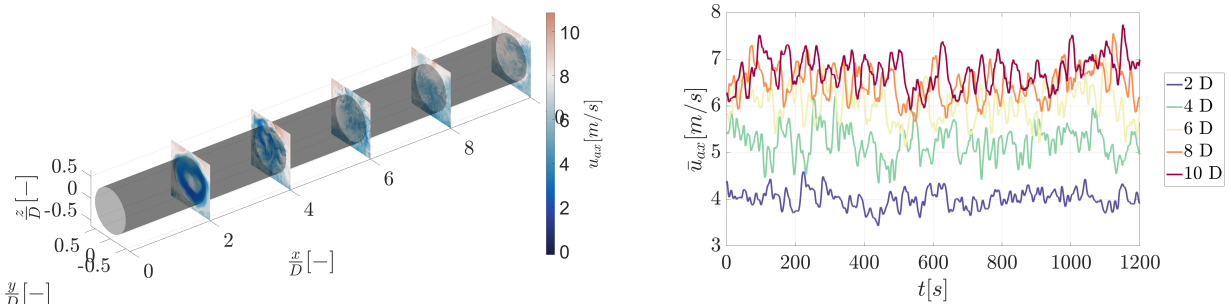


(a) Slices showing contour plots of the instantaneous streamwise velocity at $t = 1200[s]$. The transparent cylinder indicates the rotor plane cylinder, the area of spatial averaging.

(b) Instantaneous streamwise velocity averaged over a rotor plane cylinder slice.

Figure 5.12: Transient behaviour of the streamwise velocity for case turb_base.

**High-velocity region downstream of nacelle**

A vertical slice of the mean streamwise velocity at $y = 0$ is shown in fig. 5.12. Similar to the uniform inflow case, the effect of the rotor on the velocity results in a velocity deficit in the regions inside the rotor radius and outside the nacelle radius. Immediately downstream of the nacelle, there is no velocity deficit.

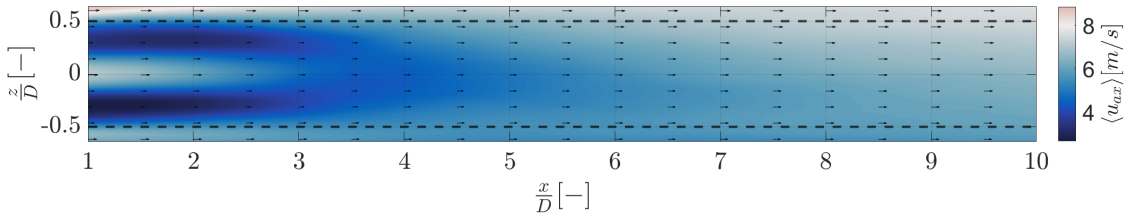


Figure 5.13: A vertical slice of the mean streamwise velocity at $y = 0$for case turb_base. The dotted lines indicate the rotor plane cylinder. The quiver arrows indicate the local flow direction in the $[x\,z]$-plane.

### Mean velocity profile

Streamwise mean velocity profiles of vertical lines at various distances downstream of the rotor are shown in fig. 5.14. The free-stream follows a shear layer defined by the power profile, where the free stream velocity $u_\infty$ is defined at hub height. Again, it is clear that there is no velocity deficit immediately downstream of the nacelle. The velocity deficit is distributed over space until the velocity deficit assumes an approximately Gaussian profile until it is finally further distributed to a shear layer profile in the far wake. The flow for this simulation does not accelerate to faster than the free-stream wind near the domain boundaries, indicating that the blockage ratio used in this simulation is sufficiently low.

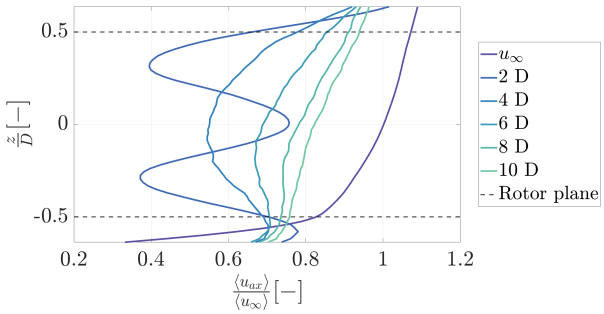


Figure 5.14: Time-averaged streamwise velocity profiles of a vertical line at the rotor centre at various distances downstream for case turb_base.

### Coherent structure in the far-wake

An instantaneous snapshot of the streamwise velocity is shown in fig. 5.15. As a result of the turbulent inflow, flow regions with various velocities are distributed erratically throughout the wake. The quiver lines showing the two-dimensional local velocity direction indicate an up-and-down motion travelling through the wake. The wave-like structure that is conjectured to be a Kelvin-Helmholtz Instability is not present. Inspecting the interface between the free stream and the wake elucidates why this is the case: there is no longer a top-hat velocity profile with a sharp interface. The effects of small perturbations that will exponentially grow into the Kelvin-Helmholtz Instability are overshadowed by effects resulting from the turbulence, such as wake meandering. Wake meandering effects will be further investigated later in this section.

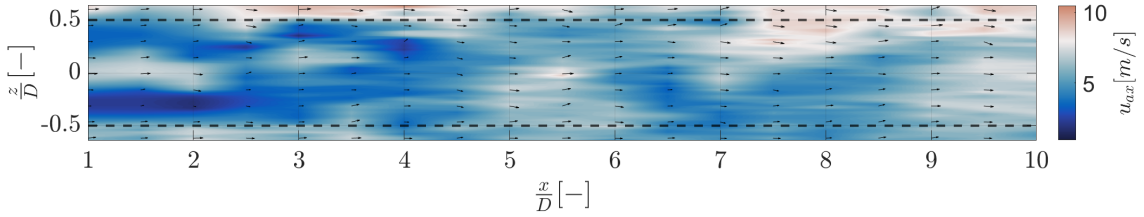


Figure 5.15: A vertical slice of the instantaneous streamwise velocity at $y = 0$ at $t = 1200[s]$ for case turb_base. The dotted lines indicate the rotor plane cylinder. The quiver arrows indicate the local flow direction in the $[xz]$-plane.

### 5.2.2. Proper Orthogonal Decomposition

Proper Orthogonal Decomposition is applied to slices parallel to the rotor plane. The first seven spatial modes of vertical slices parallel to the rotor plane, separated $2D$ are shown in fig. 5.16. Their respective frequency spectra are shown infig. 5.17. Finally, their respective relative energy is shown in fig. 5.18. The mean mode, $r = 0$, is identical to the mean flow. The frequency of the mean mode is $f = 0$. At $0D$, the mean mode shows the expected shear layer of the undisturbed velocity field. In this region, $60\%$ of the energy is described by the mean.

At $2D$, the mean mode shows the velocity deficit inside the rotor plane and outside the nacelle radius. In this region, $20\%$ of the energy is described by the mean. Compared to the mean mode found from the uniform inflow, the relative energy of the mean mode is lower. Because more complex dynamics are present in this signal, and the energy is divided into more complex spatial and temporal dynamics, a more complex set of modes is necessary to describe the energy. The spatial modes at $2D$ show coherent structure. In unison with the mean mode, one can visualize that the reconstruction of the mean mode $r = 0$, with mode $r = 1$ oscillating around the mean, results in a side-to-side motion of the wake deficit. This mode persists throughout the wake until $8D$ and, in unison with the mean, can be associated with the side-to-side component of the wake meandering phenomenon. The frequency of this mode is $St \approx 0.2[-]$. Similarly, in unison with the mean mode, one can visualize that the reconstruction of the mean mode $r = 0$, with mode $r = 2$ oscillating around the mean, results in an up-and-down motion of the wake deficit. Again, this structure persists through the wake.

Note that the spatial modes $r = 1$ and $r = 2$ are only coincidentally linked to the horizontal and vertical motion of the wake, and they could have just as well been related to the motion of the wake in other directions. However, it seems that the wake has a preference for moving in these specific directions. A possible reason for this is the shear layer, promoting motion in the direction along the shear layer and perpendicular to the shear layer. Another possible reason is that there already seems to be side to side motion in the free stream flow arising from modes $r = 2$ and $r = 4$. The frequency of these latter modes also corresponds to the wake meandering frequency of $St \approx 0.2[-]$.

Near the rotor plane, at $2D$ and $4D$, modes $r = 3$ and $r = 4$ are paired. In unison with the mean, they contribute to a rotation in the wake deficit. Note that this is not linked to the rotational frequency of the rotor, as becomes clear when evaluating the respective frequencies associated with these modes in fig. 5.17. The frequency of the rotation of the wake deficit is located around twice that of the wake meandering phenomenon at $St \approx 0.4$.

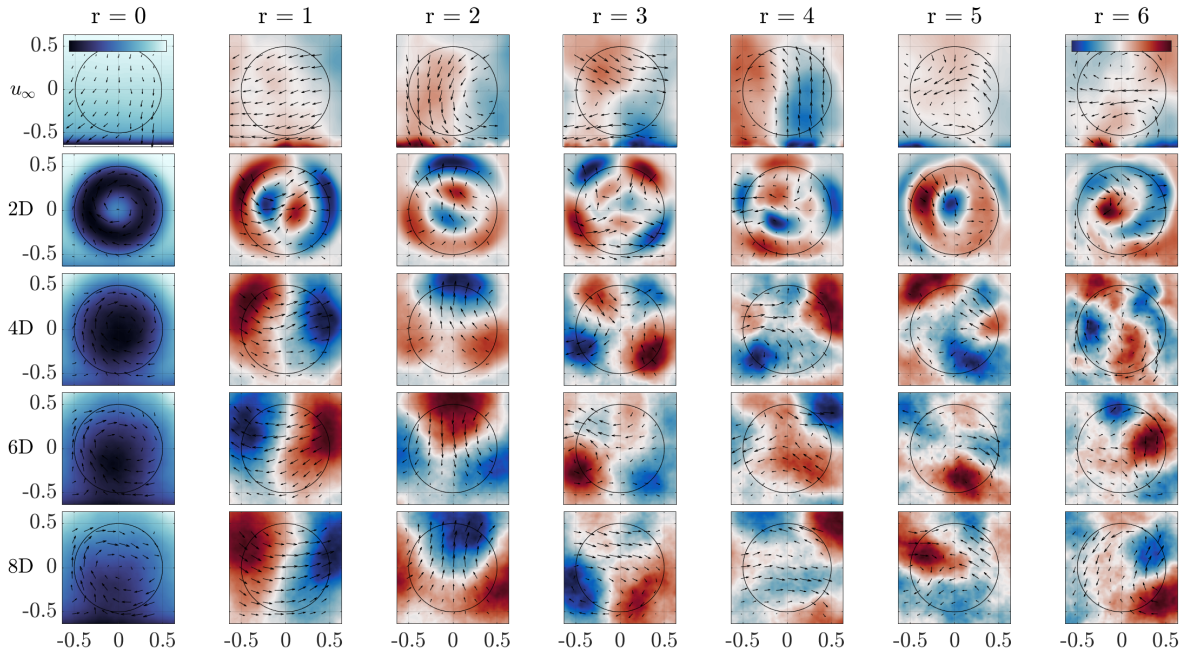


Figure 5.16: The first seven spatial modes of Proper Orthogonal Decomposition performed on the velocity field of vertical slices parallel to the rotor plane, separated $2D$ for case turb_base. The first mode $r = 0$ is the mean. The modes $r = 1, 2, \ldots, 6$ oscillate around the mean. The quiver arrows indicate the $v$ and $w$ components of the respective modes. The modes are used for qualitative analysis, and their magnitude is only taken into account in the frequency spectrum.

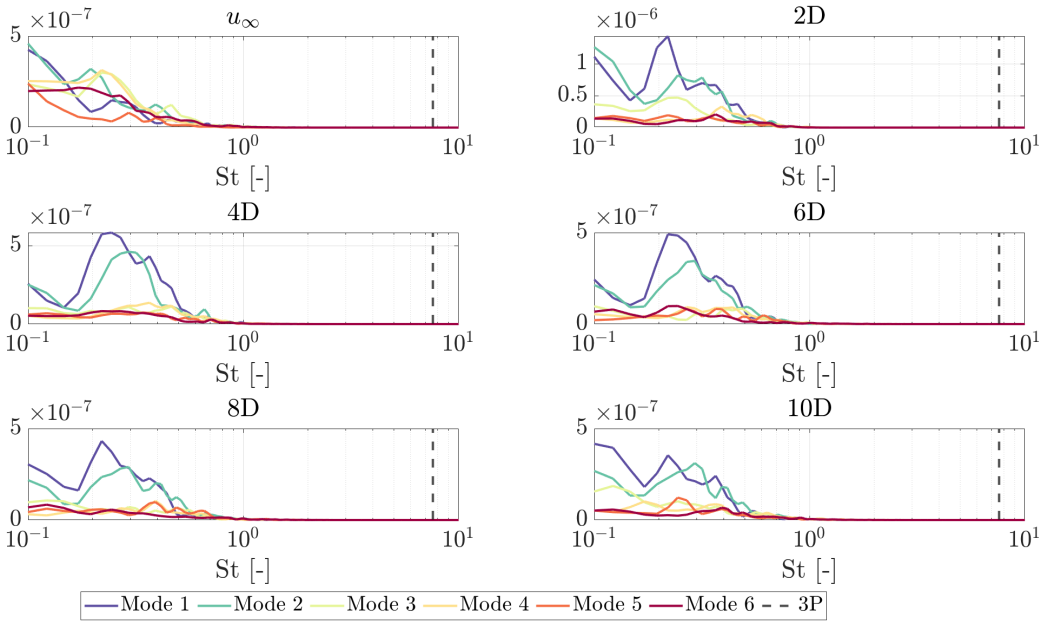


Figure 5.17: The frequency spectrum found by applying Welch's method on the first six temporal modes multiplied with their respective variance $\sigma$ excluding the mean mode, of Proper Orthogonal Decomposition performed on the velocity field of vertical slices parallel to the rotor plane, separated $2D$ for case turb_base.

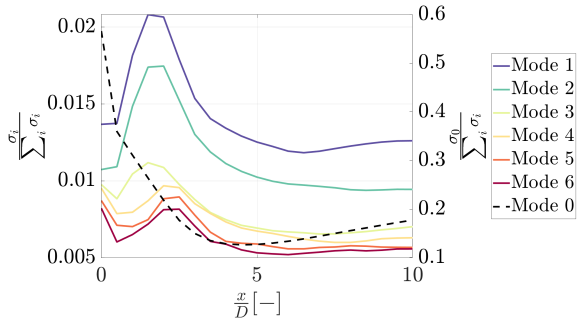


Figure 5.18: Relative energy of the first seven modes for case turb_base. The relative energy of the mean mode is much larger than the other modes and plotted on the right $y$-axis.

The rotor frequency does not show up in the signals as it does for uniform inflow. The frequency spectrum at $0.5D$ is shown on a double logarithmic axis in fig. 5.19. The 3P frequency can be seen here, and it becomes clear that the magnitude of this signal is low compared to the other phenomena present in the signal.

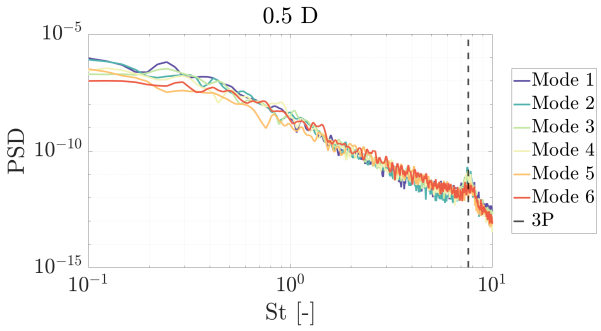


Figure 5.19: The frequency spectrum found by applying Welch's method on the first six temporal modes multiplied with their respective variance $\sigma$ excluding the mean mode, of Proper Orthogonal Decomposition performed on the velocity field of vertical slices parallel to the rotor plane, at $0.5D$ for case turb_base.

**Wake meandering**

The wake meandering conjecture arising from the POD analysis is analyzed by finding the wake centre location at every time step and applying Welch's method to find the frequency at which this phenomenon occurs. This is performed at locations separated $2D$ and shown in fig. 5.20. The wake center oscillates in a side-to-side motion around $St = 0.2[-]$. The side-to-side motion is stronger than the up-and-down motion.

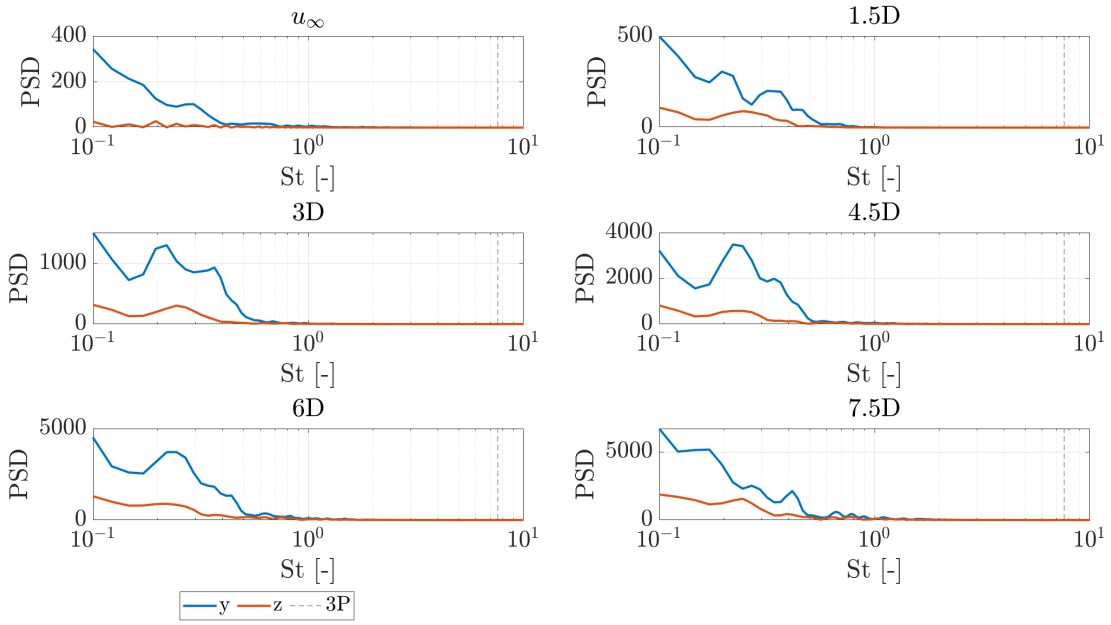


Figure 5.20: The frequency spectrum found by applying Welch's method on the time signal of the respective $y$ and $z$-location of the wake centre found at locations separated $1.5D$, for case turb_base.

## 5.3. Dynamic induction control

This section shows an analysis of the dynamics occurring in the wake of a wind turbine actuated with dynamic induction control at $St = 0.25[-]$ under uniform inflow conditions. The cases used to perform this analysis are uni_high_0.25

and uni_low_0.25. First, the flow is analysed by looking at instantaneous snapshots of the velocity, pressure and Q-criterion. The findings are summarised in a schematic overview. Proper Orthogonal Decomposition is used to find the relative energy and time dynamics of coherent structures in the wake.

### 5.3.1. General flow overview

#### Transient

To describe the transient behaviour of the LES simulation, the time evolution of the spatial average of circular slices with rotor diameter $D$ parallel to the rotor plane, separated $2D$, is shown in fig. 5.21b. It can be seen that the solution stabilizes after approximately $1500s$. From here on, data with $t > 2000s$ will be used for analysis. The flow assumes perfectly periodic behaviour after the transient. This is to be expected with a perfectly periodic excitation signal on the wind turbine and uniform inflow. When taking time-averages of flow quantities, care needs to be taken to average over integer periods of the excitation signal.

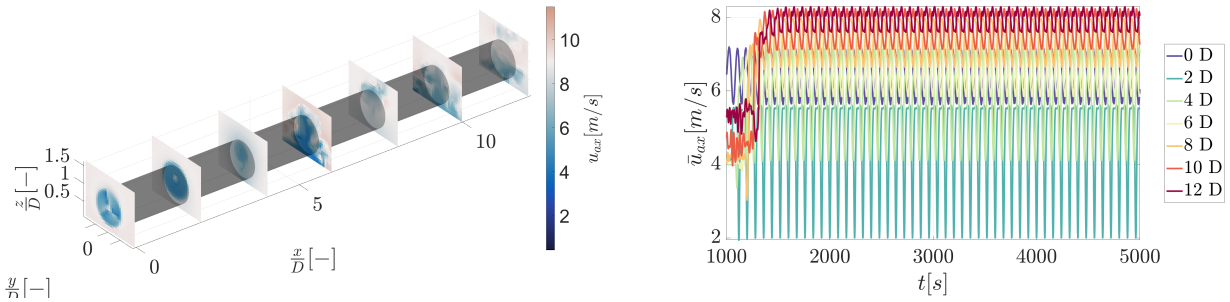


(a) Slices showing contour plots of instantaneous streamwise velocity at $t = 5000[s]$. The transparent cylinder indicates the rotor plane cylinder, the area of spatial averaging.

(b) Instantaneous streamwise velocity averaged over a rotor plane cylinder slice.

Figure 5.21: Transient behaviour of the streamwise velocity for case uni_high_0.25.

#### Turbine signal

The excitation signal applied on the blade pitch $\theta$ is shown in fig. 5.22. The sinusoidal signal applied on the pitch results in a sinusoidal behaviour of the thrust coefficient $C_T$. The flow can be analysed as a function of the actuation signal. Velocity and pressure data in the flow field are coupled to an excitation signal bin and a time-step. The dotted lines indicate the bin edges. The bin counter resets to $1$ after one actuation period. The velocity and pressure data in the same bin is averaged to find the average quantity per bin.

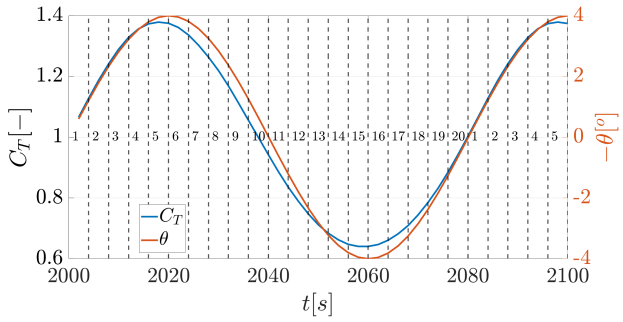


Figure 5.22: Periodically oscillating thrust coefficient $C_T[-]$ caused by periodically oscillating blade pitch $\theta$ for case uni_high_0.25. The flow data is divided into bins. Bin walls are indicated with dotted lines.

### 5.3.2. Dynamic induction control phenomena

Instantaneous snapshots of the instantaneous streamwise velocity, pressure and Q-criterion at four bins corresponding to $\theta = -4^o$, $0^o$, $0^o$ and $4^o$ are shown in fig. 5.23 and fig. 5.25. Figure 5.22 shows that this corresponds to bins $5$, $10$, $15$ and $20$. The arising phenomena will be discussed by tracking the low-velocity field through the wake. Additionally, the reaction of the flow in the rotor plane to the actuator signal is discussed. The analysis will show that the low-velocity field corresponds to a low-pressure field, and is the region where the coherent vortex ring arises that is conjectured to be responsible for the increase in energy transport from the surrounding flow into the wake.

**Location A,** $\theta = -4^o$

A is located at the rotor plane. The top figure corresponds to $\theta = -4^o$. At $\theta = -4^o$, the rotor extracts a high amount of energy from the flow. As a result, a system of relatively low velocity is created. The pressure immediately downstream of the rotor is relatively low, as the pressure drop over the rotor is largely due to the high thrust. The Q-criterion isocontour in fig. 5.25 shows a coherent vortex system connected to the rotor with a length of approximately $0.5D$. This can be explained by the large shear between the high-velocity flow surrounding the wake and the low-velocity flow in the wake.

**Location B,** $\theta = 0^o$

B is located $0.7D$ downstream of the rotor plane. The low-velocity field created as a result of the high thrust coefficient has travelled with the wake velocity. Additionally, the low-pressure field has also been convected with the wake velocity. At location B, the wake is starting to expand. This is a result of the continuity equation and decreasing velocity, as described by Actuator Disk Theory. At the top of the wake, surrounding flow is accelerated to faster than the free-stream wind speed, indicated by the red glow. This is caused by the high blockage ratio. The coherent vortex system connected to the rotor, shown by the Q-criterion in fig. 5.25, has grown to a length of approximately $1D$.

**Location C,** $\theta = 4^o$

C is located $1.4D$ downstream of the rotor plane. Figure 5.23a shows there is a positive radial velocity component before the system of low velocity and a negative radial velocity component behind the system of low velocity. This can be interpreted as the relatively high-speed flow in the wake, released between $\theta = 0^o$ and $\theta = 4^o$, overtaking the relatively low-speed flow in the wake. The high-speed flow chooses the path of least resistance, travelling around the low-speed flow by moving up. From a pressure point of view, this motion upwards can be explained by the flow accelerating towards a region of low pressure. It can indeed be seen in fig. 5.23b that at location C, a low-pressure zone concentrated around the edge of the rotor plane starts to form. This also explains the downward motion of the high-velocity flow behind location C: it is accelerated towards the low-pressure zone, resulting in a velocity component in the radial direction. Finally, the radial velocity in the wake can be explained by the fact that the wake expands around the low-velocity regions and contracts around the relatively high-velocity regions. This expansion and contraction is accompanied by a radial velocity component. It can be seen in fig. 5.24 that the positive radial velocity before location C, negative radial velocity after location C, and shear between the high-velocity flow surrounding the wake and the low-velocity flow in the wake, a stronger vortex is formed, shown by a higher positive Q-criterion. The radial velocity component transports low-energy flow out of the wake and transports high-energy flow into the wake. This claim will be further investigated in chapter 6. At $\theta = 4^o$, the rotor extracts a relatively low amount of energy from the flow. A system of relatively high velocity is released. The pressure immediately downstream of the rotor is relatively high. The coherent vortex system shown by the Q-criterion in fig. 5.25 has released from the rotor. This can be explained by the reduction of shear between the high-velocity flow surrounding the wake and the low-velocity flow in the wake.

**Location D,** $\theta = 0^o$

D is located $1.9D$ downstream of the rotor plane. The radial velocity components have grown slightly. This can be seen most clearly by the increase in the Q-criterion in fig. 5.24. Apart from the stronger vortex at the edge of the rotor plane, a second vortex has formed around the centre of the rotor plane. The Q-criterion isocontour in fig. 5.25 shows that this vortex has a doughnut shape centred around the root vortex. This inner vortex ring results from the shear

layer between the region of high-speed flow in the nacelle wake and low-speed flow in the wake. The inner vortex arises for the same reasons as the outer vortex. However, the nacelle wake is an artefact of the simulation and will not appear in physical flow. At $\theta = 0^o$, a new coherent vortex system starts to be formed at the rotor plane for the next cycle.

**Location E,** $\theta = -4^o$
E is located $2.3D$ downstream of the rotor plane. It can be seen in fig. 5.24 that the inner vortex ring and outer vortex ring have come close to each other and have started to interact. It can be seen in fig. 5.23a that the high-velocity region from the nacelle wake has left the root vortex region and is spread over a larger area.

**Locations F, G, and H,** $\theta = -4^o$
F is located $3.2D$ downstream of the rotor plane. The high-velocity region from the nacelle wake shown in fig. 5.23a has spread further. The Q-criterion at the bottom of the wake cylinder shown in fig. 5.24 has started to move up. G is located $4D$ downstream of the rotor plane, H is located $4.7D$ downstream of the rotor plane. The coherent ring vortex has broken up due to the interaction of the inner and outer vortex ring. The wake remains dominated by relatively high-speed and low-speed flow regions, but the variations are less high.

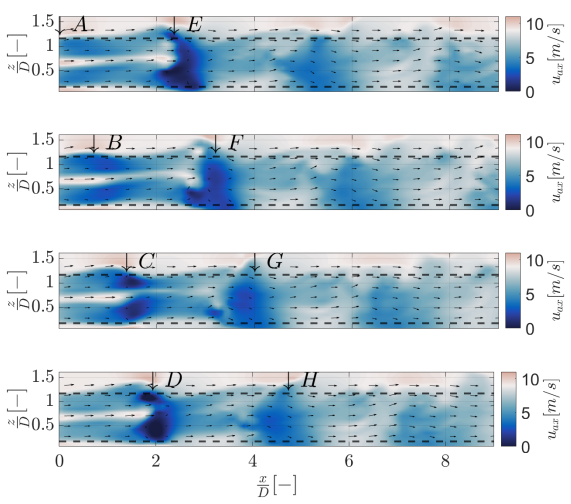


(a) Vertical slice of the streamwise velocity averaged over a bin at the shown value of the excitation signal at the centre of the rotor plane for case uni_high_0.25.

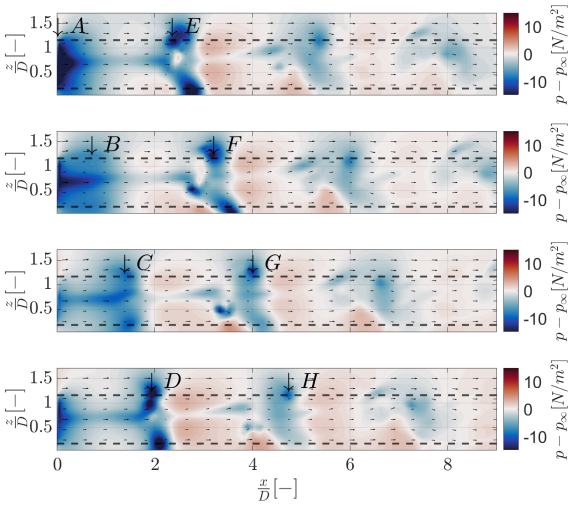


(b) Vertical slice of the pressure averaged over a bin at the shown value of the excitation signal at the centre of the rotor plane case uni_low_0.25.

Figure 5.23: Streamwise velocity and pressure at $y = 0$, averaged over a bin, at, from top to bottom, $\theta = -4^o, 0^o, 4^o$ and $0^o$. The dotted lines indicate the rotor plane cylinder. The quiver arrows indicate the local flow direction in the $[xz]$-plane. The letters indicate the locations of interest, tracking the low-velocity field through the wake.

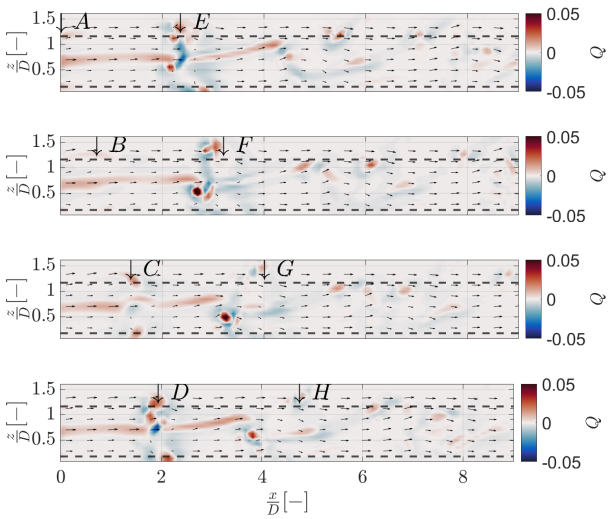


Figure 5.24: Vertical slice of the Q-criterion at $y = 0$, computed from velocities averaged over a bin at, from top to bottom, $\theta = -4^o, 0^o, 4^o$ and $0^o$, for case uni_high_0.25.

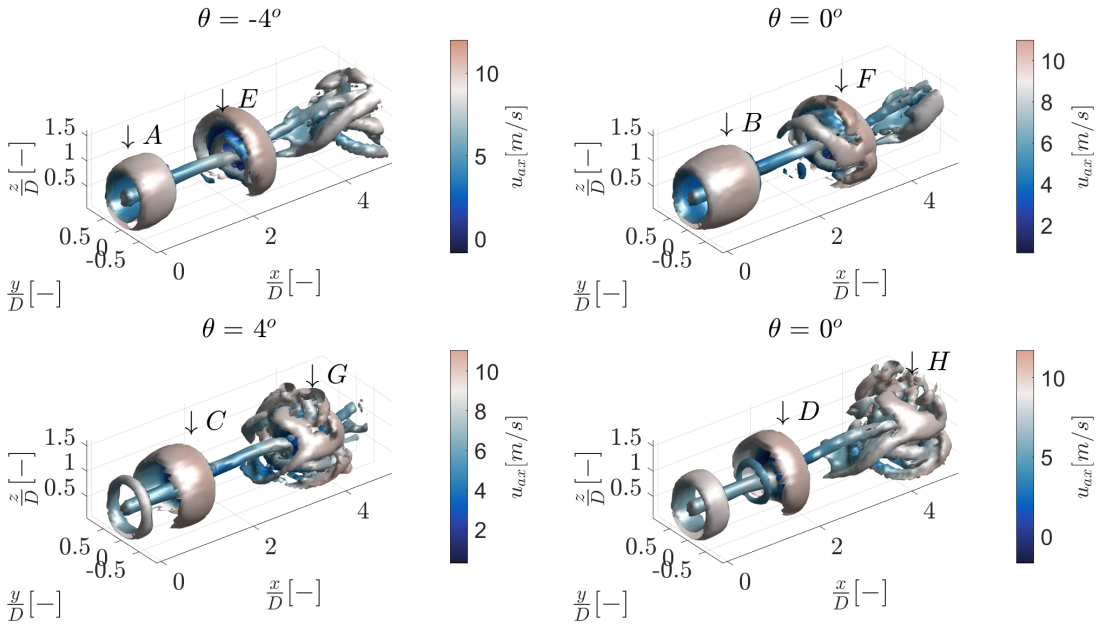


Figure 5.25: Isosurface of the Q-criterion, computed from velocities averaged over a bin at $\theta = -4^o, 0^o, 4^o$ and $0^o$, where $Q = 0.0001$, coloured by the local streamwise velocity, for case uni_high_0.25.

### 5.3.3. Schematic overview

A schematic interpretation of the phenomena that occur in the wake of a wind turbine actuated with dynamic induction control is shown in fig. 5.26.

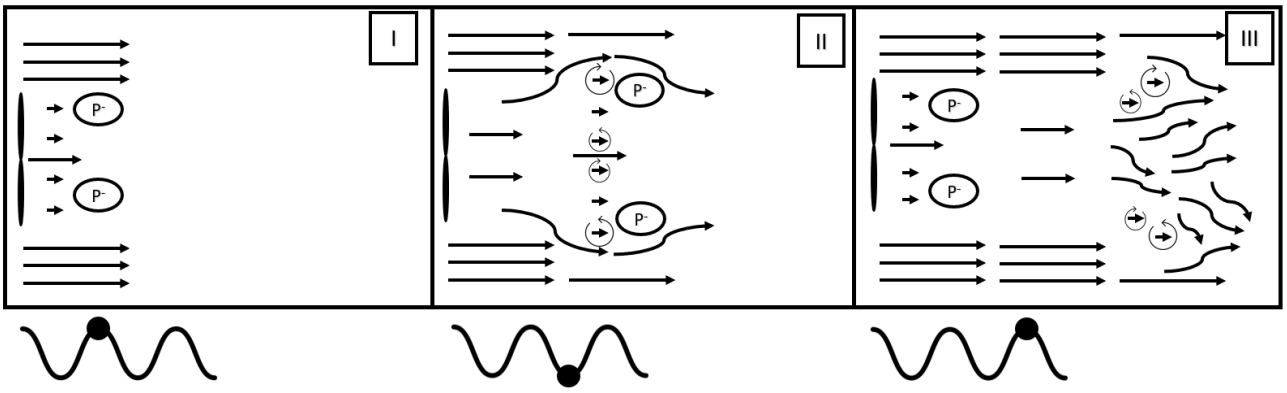


Figure 5.26: Schematic overview of the phenomena occurring in the wake of a wind turbine actuated with dynamic induction control.

1. High thrust.
    - High energy is extracted from the flow by the rotor.
    - A system of relatively low velocity is released.
    - This system is characterised by low pressure.
    - The system is prevented from expanding by the tip vortices.
2. Low thrust, creation of inner and outer vortex ring.
    - Low energy is extracted from the flow by the rotor.
    - A system of relatively high wake velocity is released.
    - The system of low velocity expands as a result of continuity.
    - The regions of low-pressure move towards the edge of the wake.
    - The low-velocity flow from inside the wake accelerates towards the region of low pressure, resulting in a positive radial velocity.
    - The high-velocity flow from outside the wake accelerates towards the region of low pressure, resulting in a negative radial velocity.
    - The positive radial velocity before the low-pressure region, negative radial velocity after the high-pressure region, and shear between the high-velocity flow surrounding the wake and the low-velocity flow in the wake, create a vortex at the interface between the wake and high-velocity flow.
    - An inner vortex is formed at the shear layer between the high-velocity nacelle wake and low-velocity wake flow.
3. High thrust, start of a new cycle and ring vortex breakdown.
    - Low energy is extracted from the flow by the rotor.
    - A new system of low velocity is created that travels slower than the system of the previous cycle. The systems from separate cycles do not interact.
    - The vortex system is travelling downstream. The interaction between the outer vortex and inner vortex results in the breakdown of the coherent vortex ring.
    - The breakdown of the vortex ring is accompanied by an increase in turbulence intensity.

### 5.3.4. Proper Orthogonal Decomposition

Proper Orthogonal Decomposition is applied to give insight into the coherent spatial and temporal structures. Firstly, POD is applied on slices parallel to the rotor plane. Then, POD is applied to a vertical slice perpendicular to the rotor plane.

#### Parallel slices

The first seven spatial modes of vertical slices parallel to the rotor plane, separated $2D$ are shown in fig. 5.27. Their respective frequency spectra are shown in fig. 5.28. Finally, their respective relative energy is shown in fig. 5.29.

At $0D$, modes $r = 2, 3, 4$ and $5$ together reconstruct the rotating character of the wake. Modes $r = 1$ and $6$ combine to reconstruct the accelerating and decelerating axial velocity in the rotor plane. The mean has a strong radial velocity component. The modes show acceleration and deceleration of this radial velocity component. All modes show a frequency peak at the actuation frequency $St = 0.25[-]$. At $2D$, the first six spatial modes show a strong coherent structure that reconstructs both the acceleration and deceleration in the wake centre and shows a characteristic ring outside the rotor area associated with the vortex ring created by dynamic induction control. The modes show a strong radial component of the flow, suggesting strong interaction between the free-stream flow and the flow in the wake. The relative energy of the first 6 modes peaks around $2D$. All modes show a frequency peak at the actuation frequency and harmonics of the actuation frequency. At $4D$, traces from the strong coherent structure at $2D$ are still present but less clearly defined. Additionally, the relative energy in the first 6 modes has decreased. Most of the coherent structure has broken down and will decay into turbulence further in the wake. Clear frequency peaks at the actuation frequency and harmonics of the actuation frequency can be seen throughout the wake. The mean mode, $r = 0$, is identical to the mean flow. The energy of the mean mode decreases until $3.5D$, when it starts increasing again. This location coincides with the breakdown of the coherent ring vortex that can be seen in fig. 5.25.

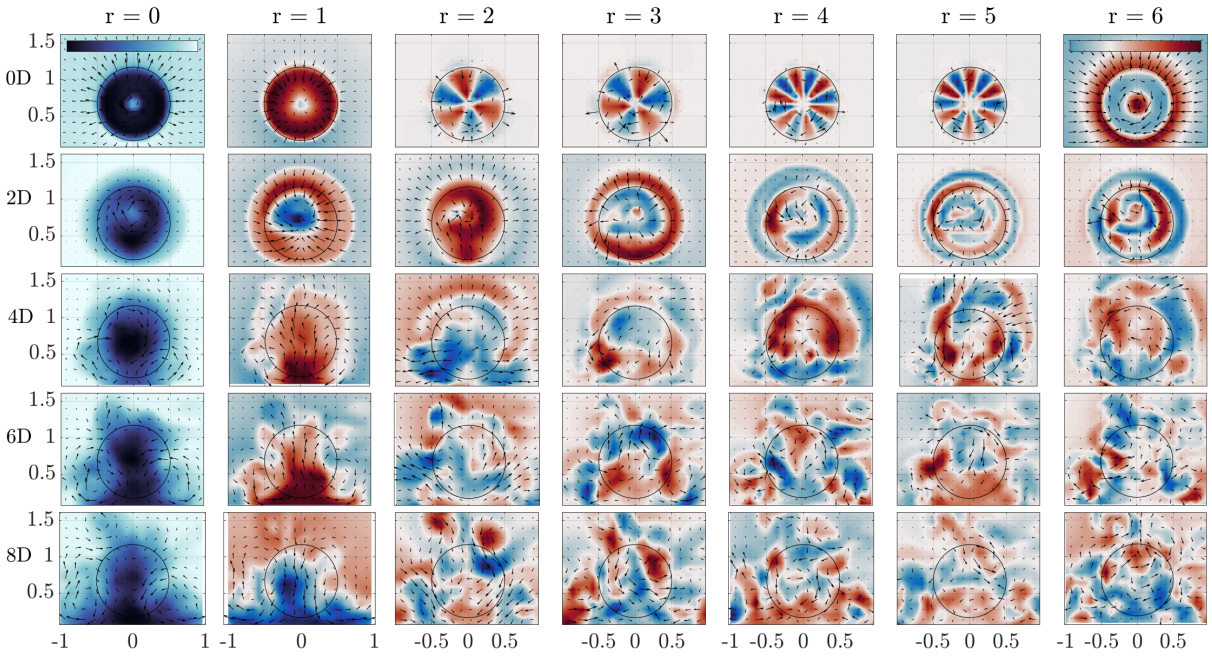


Figure 5.27: The first seven spatial modes of Proper Orthogonal Decomposition performed on the velocity field of vertical slices parallel to the rotor plane, separated $2D$ for case uni_high_0.25. The first mode $r = 0$ is the mean. The modes $r = 1, 2, \ldots, 6$ oscillate around the mean. The quiver arrows indicate the $v$ and $w$ components of the respective modes. The modes are used for qualitative analysis, and their magnitude is only taken into account in the frequency spectrum.

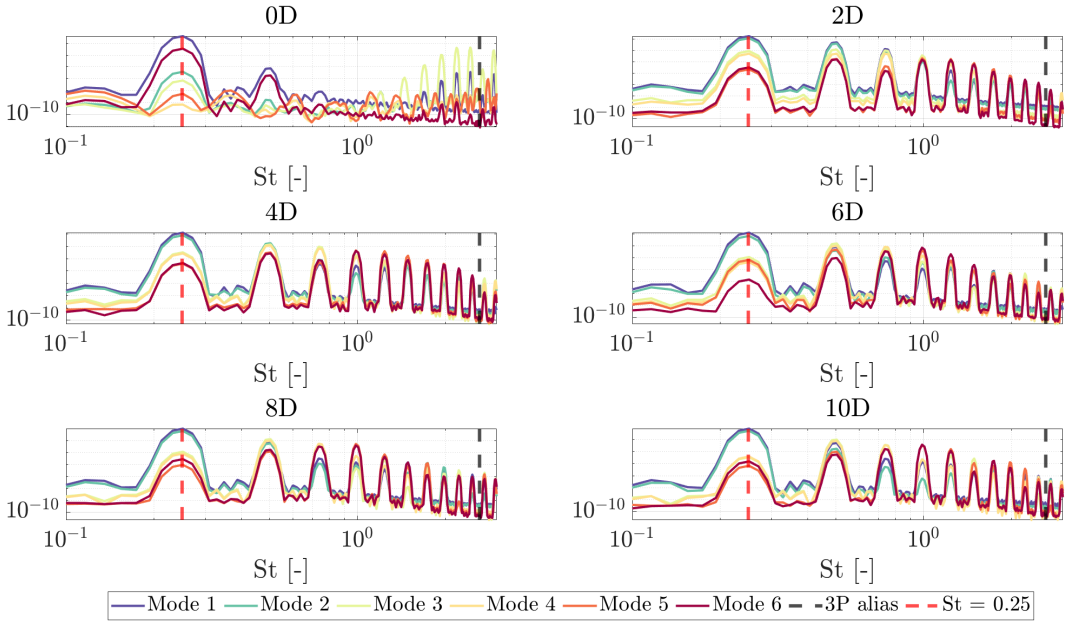


Figure 5.28: The frequency spectrum found by applying Welch's method on the first six temporal modes multiplied with their respective variance $\sigma$ excluding the mean mode, of Proper Orthogonal Decomposition performed on the velocity field of vertical slices parallel to the rotor plane, separated $2D$ for case uni_high_0.25.

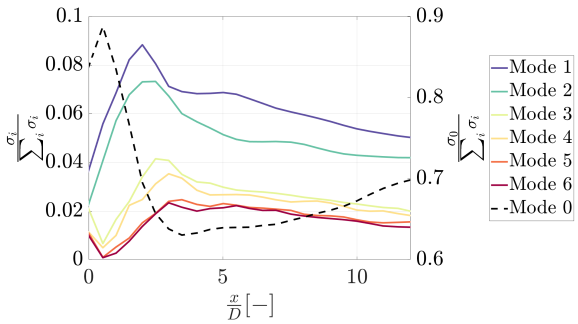


Figure 5.29: Relative energy of the first seven modes for case uni_high_0.25. The relative energy of the mean mode is much larger than the other modes and is plotted on the right $y$-axis.

**Perpendicular slice**

Proper Orthogonal Decomposition is applied to a vertical slice perpendicular to the rotor plane. The actuation frequency and harmonics of the actuation frequency are dominant throughout the wake. The spatial modes show a higher intensity in the region $1D - 3D$. The axial acceleration and deceleration in the spatial modes is accompanied by the acceleration and deceleration of the radial velocity.

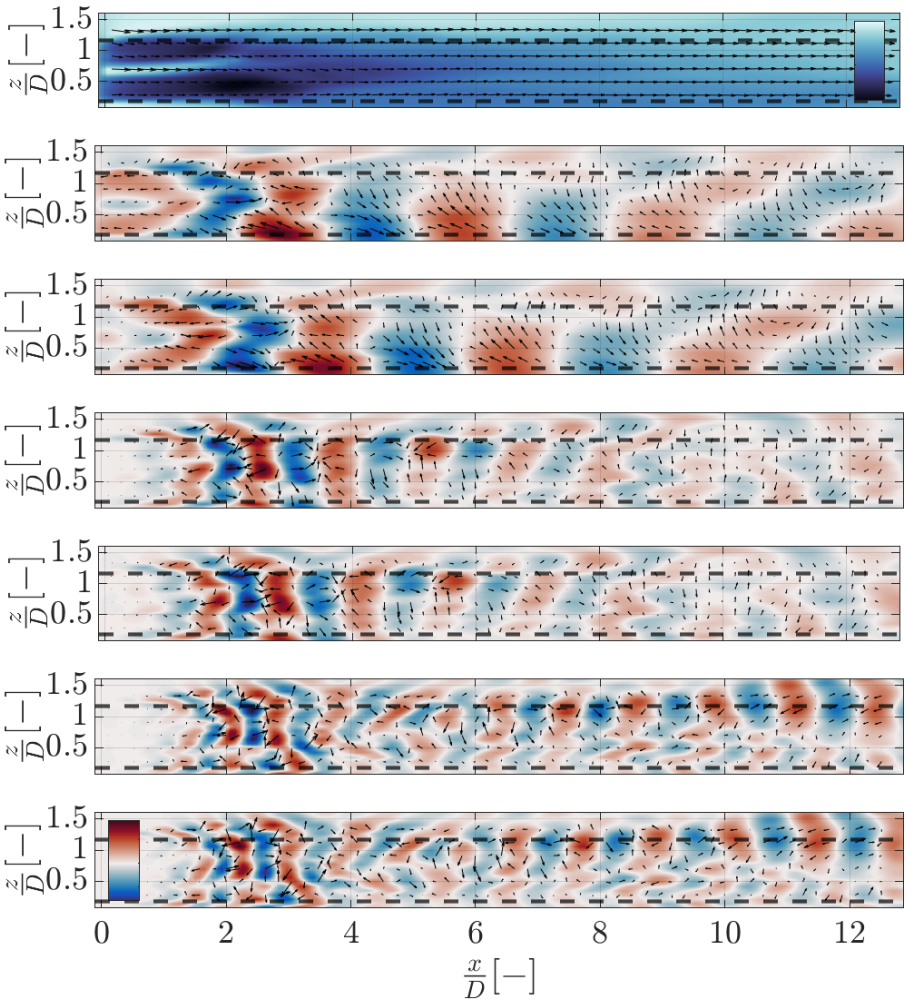


Figure 5.30: The first seven spatial POD modes for case uni_high_0.25. The first mode $r = 0$ is the mean. The modes $r = 1, 2, \ldots, 6$ oscillate around the mean. The quiver arrows indicate the $v$ and $w$ components of the respective modes. The modes are used for qualitative analysis, and their magnitude is only taken into account in the frequency spectrum.

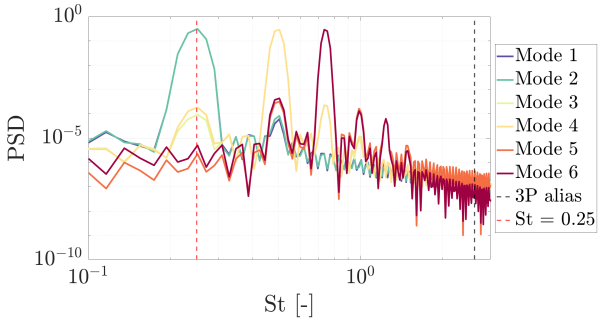


Figure 5.31: The frequency spectrum found by applying Welch's method on the first six temporal modes multiplied with their respective variance $\sigma$, excluding the mean mode for case uni_high_0.25.

## 5.4. Discussion

This section discusses the findings of this chapter. First, the findings for baseline control with uniform and turbulent inflow are presented. Then, the findings for dynamic induction control are discussed.

### 5.4.1. Baseline control, uniform inflow

The POD analysis shows that in the near wake of the simulated wind turbine with baseline control under uniform inflow, until $5D$, the flow is dominated by the mean, and there are no dynamics. After $5D$, the dominant phenomenon in this simulation is the Kelvin Helmholtz Instability. The Kelvin Helmholtz Instability relies on a stable interface between the wake and free stream. Other than the Kelvin Helmholtz Instability, there are no dynamics found that can be leveraged for dynamic induction control. Proper Orthogonal Decomposition also reveals oscillations at $St = 0.4[-]$ between $2D - 4D$ related to the nacelle wake. While these have very little energy compared to the mean, they might be related to the initial perturbation that grows into the Kelvin Helmholtz Instability. The nacelle wake is an artefact of the simulation but is conjectured to cause the onset of the dominant phenomenon in the wake. This can potentially be solved by running a simulation where the nacelle is modelled as a body-force (Churchfield et al., 2015). Blockage effects can be seen in the form of flow acceleration near the domain boundaries, but they do not influence the phenomena in the wake. The resolution of the used data-set captures the dominating dynamics in the form of the Kelvin Helmholtz Instability. However, the spatial resolution is too low to capture the tip vortices in the Q-criterion. The temporal resolution is too low to describe the $3P$ frequency.

Comparing the POD results to fig. 2.17, the described Kelvin Helmholtz Instability is also found by De Cillis et al. (2020). However, the the tip vortices and von Kármán vortex street described by De Cillis et al. (2020) are not seen. It is clear that the vortex street is not captured because the tower is not modelled in this simulation. The spatial resolution from the data-set is too low to see the tip-vortices.

### 5.4.2. Baseline control, turbulent inflow

The POD analysis shows that the dominant phenomenon in the wake of the simulated wind turbine with baseline control under turbulent inflow is wake meandering and that the wake meandering is strongest in the side-to-side direction. This is confirmed by evaluating the wake centre location using the weighted centre approach. No phenomena resembling the Kelvin Helmholtz Instability can be seen. The interface between the low-velocity flow in the wake and the high-velocity flow surrounding the wake is smoothed out and constantly moving. Additionally, it can be seen from the energy distribution in the POD modes that the mean is less dominant and most of the energy is present in the modes. Similar to the uniform inflow case, a strong nacelle wake as a result of not modelling the nacelle can be seen. However, the effect of the nacelle wake is less pronounced in this simulation. The inflow conditions for this simulation, turbulent inflow and a vertical velocity profile in the wind, are more realistic than for the uniform inflow case. Therefore, the phenomena found from this simulation are likely a better representation of reality. Addition-

ally, the domain is larger so that there are no blockage effects. A drawback of the available data-set is that the spatial resolution in the axial direction is not high enough to see tip vortices.

Comparing the POD results to fig. 2.18, similar dipole, quadrupole, and hexapoles can be seen as found by Sørensen et al. (2015). Additionally, the relative energy distribution shows a similar profile. Contrary to Sørensen et al. (2015), the monopoles occurring in the far wake can not be seen. The spatial domain of the available data is not long enough.

### 5.4.3. Dynamic induction control

The wake of the simulated wind turbine with dynamic induction control under uniform inflow can be divided in three regions. Region I exists from the rotor plane to approximately $1D$. The transition from region I to region II is characterised by the creation of a vortex ring. The vortex ring is accompanied by a positive radial velocity component before the vortex and a negative radial velocity behind the vortex. This is conjectured to transport low energy flow from the wake out of the wake and high energy flow into the wake. This is further investigated in chapter 6. The transition from region II to region III is characterized by the breakdown of the vortex ring. In this simulation, the breakdown is initiated by interaction with an inner vortex ring that is created around the nacelle wake. The exact breakdown location is hard to characterize on the based analysis. The breakdown location based on inspecting the Q-criterion isocontour is around $3D$. Alternatively, the same location can be found by inspecting the relative energy of POD modes parallel to the rotor plane.

The breakdown of the vortex ring is related to the interaction with the inner vortex formed around the nacelle wake. This nacelle wake is an artefact of the simulation, so no accurate prediction on the breakdown dynamics can be made following the analysis of this simulation. Further drawbacks of the applied simulation environment are blockage effects and the lack of a realistic boundary condition at the floor boundary layer. At the top of the wake, the flow is accelerating as a result of blockage. At the bottom of the boundary layer, the wake wants to expand but meets the boundary layer. However, no realistic shear layer is formed. The dynamics occurring at the bottom of the wake are hard to interpret. When including more realistic boundary conditions, such as a shear layer or turbulent inflow, there might be new interactions that cause the ring vortex breakdown. Most interestingly, the wake meandering phenomenon found in this work and by Andersen et al. (2013) occurs around $St = 0.2[-]$ and might interact with the vortex ring.

# 6

# Analysis of transport of kinetic energy

This chapter presents an analysis of the transport of kinetic energy from the surrounding flow into wake. First, the baseline control case with uniform and turbulent inflow are analysed. This gives more insight into the flow dynamics found in chapter 5 while also allowing for validation of the kinetic energy transport framework against similar cases in literature. The, the kinetic energy transport framework is applied on dynamic induction control with uniform inflow.

## 6.1. Baseline control, uniform inflow

This section shows an analysis of the kinetic energy transport in the wake of a turbine with baseline control under uniform inflow conditions. The cases used to perform this analysis are uni_high_base and uni_low_base.

**Power profile in the wake**

The rotor is achieving a time-averaged trust coefficient of $C_T = 0.80$. The axial induction factor is then $a = 0.28$.

$$\begin{aligned} C_T &= \frac{T}{\frac{1}{2}\rho u_\infty^2 \pi R^2} \\ C_T &= 4a(1-a) \end{aligned} \tag{6.1}$$

The power found from eq. (6.2) is shown in fig. 6.1a. The power is found from the time-averaged velocity, averaged over the rotor plane and multiplied with the rotor plane surface and normalized by the free stream power. Dotted lines are plotted at power levels corresponding to $u_{AD,rotor} = u_\infty(1-a)$ and $u_{AD,far-wake} = u_\infty(1-2a)$.

$$P/P_\infty = \frac{\frac{1}{2}\rho\langle\bar{u}_{ax}\rangle^3 \pi R^2}{\frac{1}{2}\rho u_\infty^3 \pi R^2} \tag{6.2}$$

The power level in the rotor plane matches the value predicted by Actuator Disk theory, while the power level never quite reaches the predicted value in the far wake. This can be attributed to wake mixing, which is not taken into account in Actuator Disk theory. The spatial gradient of the power in the axial direction $\partial P/\partial x$, non-dimensionalised by the rotor diameter $D$, is shown in fig. 6.1b. In the near-wake, between $0-3D$, the flow is decelerating, and the spatial gradient of the power in the axial direction is negative. In this region, the flow is accommodating to the pressure drop over the rotor-plane responsible for the power output of the wind turbine, as described by Actuator Disk theory. Around $3D$, the flow is no longer decelerating. The spatial gradient of the power in the axial direction gradient crosses zero. The power in the wake slowly increases until around $8D$, where a sharp increase in the power and power spatial gradient in the far wake $> 8D$ can be seen. This is the region where dynamics in the form of the Kelvin Helmholtz

instability start to appear, as found from section 5.1.1. The various components of the energy flux, in a time-averaged and instantaneous sense, will be investigated to quantify where this increase in power in the wake comes from.

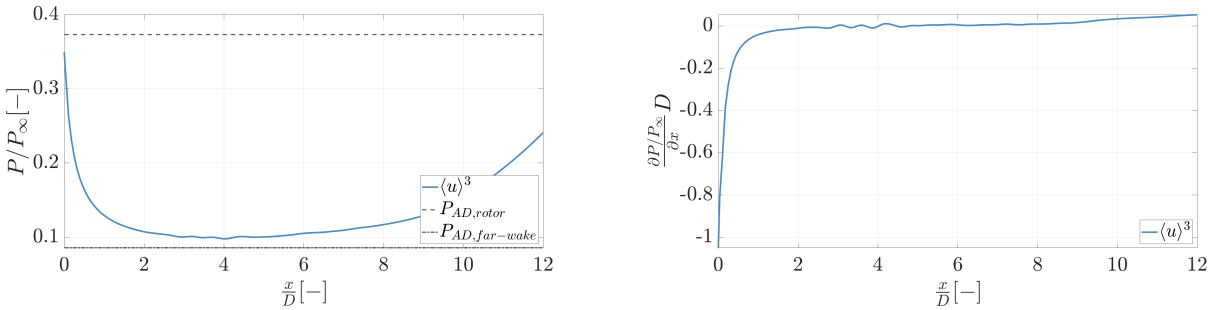


(a) Power. Dotted lines indicate the power in the rotor plane and the far wake predicted by Actuator Disk theory.

(b) Spatial gradient of power in the axial direction $\partial P/\partial x$, normalized by the rotor diameter $D$.

Figure 6.1: Power and spatial gradient of power in the axial direction found from the time-averaged velocity, averaged over the rotor plane and multiplied with the rotor plane surface and normalized by the free stream power for case uni_high_base.

There are some unexpected oscillations in the spatial gradient of power in fig. 6.1b. They are investigated by looking at a vertical slice of the local spatial gradient of power in fig. 6.2. Strong oscillations can be seen between $2D$ and $4D$, in a region associated with the nacelle wake.

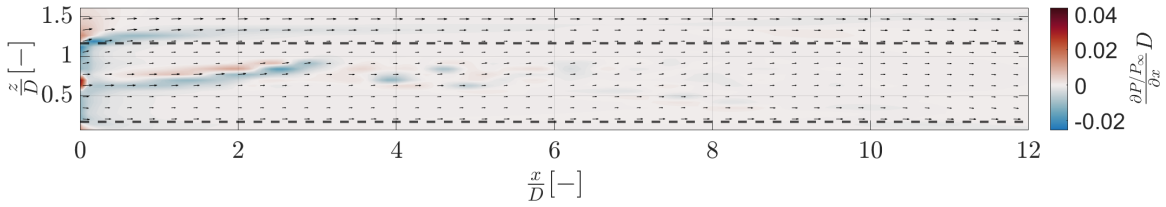


Figure 6.2: Vertical slice of the mean spatial gradient of power in the $x$-direction at $y = 0$ for case uni_high_base. The dotted lines indicate the rotor plane cylinder. The quiver arrows indicate the local flow direction in the $[x\,z]$ plane.

### 6.1.1. Transport of mean kinetic energy

The spatial gradient of power can be explained by investigating the various energy transport terms. Recalling the Reynolds Averaged Navier Stokes energy equation from chapter 4, with all terms written out and neglecting the viscous terms, where the terms are colour-coded to distinguish them in figures:

$$\underbrace{\oiint_{\mathcal{S}_{disk}} (\langle u_{ax}\rangle\langle E\rangle \cdot \hat{n})\, d\mathcal{S}}_{\text{Power increase over control volume, blue}} = -\underbrace{\oiint_{\mathcal{S}_{wall}} (\langle u_{rad}\rangle\langle E\rangle \cdot \hat{n})\, d\mathcal{S}_{wall}}_{\text{Advection, green}} - \underbrace{\oiint_{\mathcal{S}_{wall}} \left(\langle u_i\rangle\langle u_i' u_j'\rangle \cdot \hat{n}\right) d\mathcal{S}_{wall}}_{\text{Reynolds stress work, red}} - \underbrace{\oiint_{\mathcal{S}_{disk}} \left(\langle u_{ax}\rangle \frac{\langle p\rangle}{\rho} \cdot \hat{n}\right) d\mathcal{S}_{disk}}_{\text{Axial pressure work, light brown}} - \underbrace{\oiint_{\mathcal{S}_{wall}} \left(\langle u_{rad}\rangle \frac{\langle p\rangle}{\rho} \cdot \hat{n}\right) d\mathcal{S}_{wall}}_{\text{Radial pressure work, dark brown}} - \underbrace{\iiint_{\mathcal{V}} (\mathcal{P})\, d\mathcal{V}}_{\text{Production of turbulent kinetic energy, orange}} \tag{6.3}$$

The wall surface integral terms are evaluated by interpolating the required values at $40$ points along the control volume surface, averaging and multiplying with the control volume circumference. All quantities are divided by $dx$ and multiplied by rotor diameter $D$. In this way, the equation can be interpreted as the spatial gradient of power $\partial P/\partial x$ as a function of flux terms per unit length. All terms are shown in fig. 6.3a for case uni_high_base and fig. 6.3b for case uni_low_base.

The flux terms do not well describe the fluctuations in the power spatial gradient. They will not be taken into account in this analysis. For case uni_high_base, the sum of terms on the R.H.S. (shown in the plot by the black dotted line) and the power spatial gradient (shown in the plot by the blue line) are a good fit further than $3D$, confirmed by the small residual. In the near wake, $< 3D$, there is a large residual. This is caused by not taking pressure data into account. This is confirmed by the data from case uni_low_base, where there is a small residual further than $0.5D$. The large residual closer than $0.5D$ can be explained by the force field induced by the rotor, which is not considered in this work. The highest energy flux can be found $> 9D$ and is a combination of advection of kinetic energy by the mean flow, Reynolds stress work, and the production of turbulent kinetic energy. Pressure work approaches zero in the far wake. The individual components of the Reynolds Averaged Navier Stokes energy equation are addressed below.

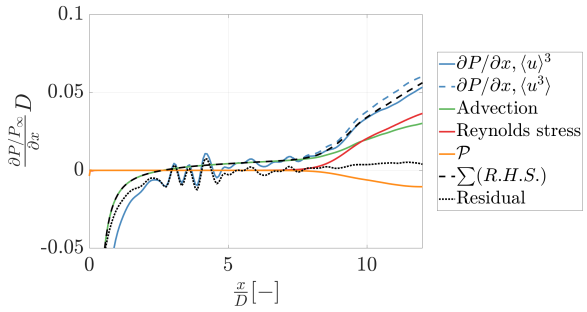


(a) Case uni_high_base.

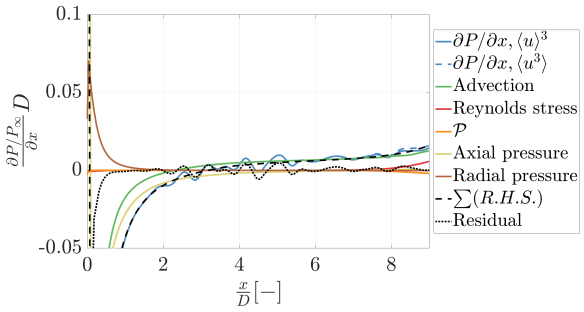


(b) Case uni_low_base.

Figure 6.3: Components of the Reynolds Averaged Navier Stokes energy equation for case uni_high_base and case uni_low_base.

### Advection

The evaluation of the advection term in eq. (6.3) is shown in fig. 6.3a for case uni_high_base. Advection is negative in the near-wake region and becomes positive around $2D$. A vertical slice of the mean radial velocity for case uni_high_base is shown in fig. 6.4. A colour map is chosen where red colours correspond to positive radial velocities, and blue corresponds to negative radial velocities. The radial velocity is positive in the near-wake, carrying energy out of the wake, matching the negative advection term. The positive advection term in fig. 6.3a suggests that above $2D$, a negative radial velocity can be expected. In this slice, that can not clearly be seen, suggesting that the positive advection component in this region comes from the left and right side of the rotor plane and not from the top and bottom of the rotor plane. The radial velocity at the top of the wake becomes negative around $9D$, carrying energy into the wake. This corresponds to the sharp increase of the advection term around $9D$ in fig. 6.3.

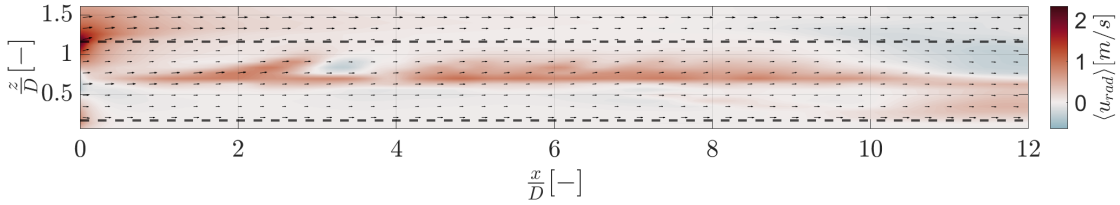


Figure 6.4: Vertical slice of the mean radial velocity $\langle u_{rad}\rangle$ at the centre of the rotor plane for case uni_high_base. The dotted lines indicate the rotor plane. The quiver arrows indicate the local flow direction in the $[xz]$ plane.

**Reynolds stress**

The surface integral of Reynolds stress components with a radial velocity term is shown in fig. 6.5. Clearly, the dominant Reynolds stress term is $\langle u_{ax}\rangle\langle u'_{ax}u'_{rad}\rangle$. In this work, the Reynolds stress flux component is therefore only evaluated by this term.

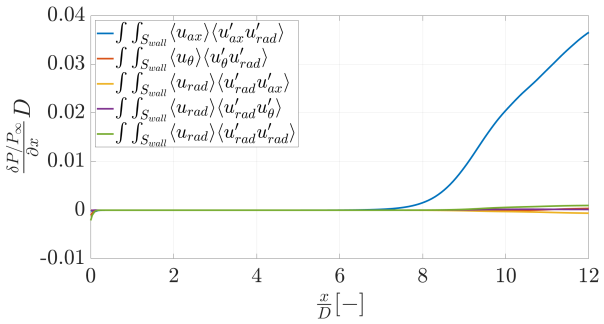


Figure 6.5: Surface integral of Reynolds stress components with a radial velocity term $u_{rad}$ for case uni_high_base.

Figure 6.3a and fig. 6.3b show an increase in the Reynolds stress term starting around $8D$. A vertical slice of the dominant Reynolds stress term $\langle u_{ax}\rangle\langle u'_{ax}u'_{rad}\rangle$ is shown in fig. 6.6. Indeed, around $8D$ the start of a region with a strong Reynolds stress component can be seen. This region coincides with the region associated with the Kelvin Helmholtz Instability discussed in section 5.1.1. Comparing this result to the one found by Newman et al. (2014), shown in fig. 2.7, different flow behaviour can be seen. The Reynolds stress region found by Newman et al. (2014) appears

immediately downstream of the rotor, while the Reynolds stress region found here only occurs $8D$ downstream. The difference is likely caused by the lack of turbulent inflow here. This will be investigated in section 6.2.

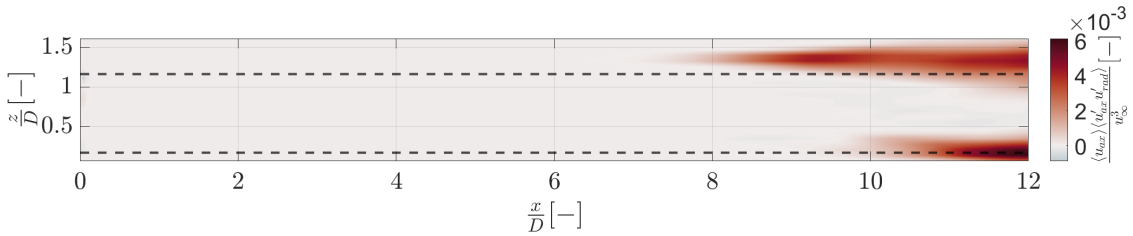


Figure 6.6: Vertical slice of the dominant Reynolds stress component $\langle u_{ax}\rangle\langle u'_{ax}u'_{rad}\rangle$ normalized by the free stream velocity $u_\infty^3$, at the center of the rotor plane for case uni_high_base.

**Pressure**

Figure 6.3b shows a negative energy contribution from the axial pressure work component in the near wake, before $5D$, and a positive flux contribution from the radial pressure work component before $2D$. A vertical slice of the pressure field for case uni_low_base, is shown in fig. 6.7. There is a low pressure region immediately downstream of the rotor, as predicted from actuator disk theory. The negative flux contribution from the axial pressure work can be explained by decomposing the surface integral:

$$\oiint_{\mathcal{S}_{disk}} (\langle u_{ax}\rangle\langle p\rangle \cdot \hat{n})\, d\mathcal{S}_{disk} = \oiint_{\mathcal{S}_{disk}} (\langle u_{ax}\rangle\langle p\rangle)\, d\mathcal{S}_{disk}\Big|_{x_{out}} - \oiint_{\mathcal{S}_{disk}} (\langle u_{ax}\rangle\langle p\rangle)\, d\mathcal{S}_{disk}\Big|_{x_{in}} \tag{6.4}$$

Pressure is increasing in the axial direction. The evaluation of the integral at $x_{out}$ is less negative than the evaluation of the term at $x_{in}$, resulting in a net positive of the surface integral, or a net negative energy contribution. In other words: more low-pressure flow is transported into the flow than low-pressure flow is transported out of the flow. This leads to a net negative energy contribution. On the other hand, the positive radial velocity $u_{rad}$ shown in fig. 6.4 in the near-wake is transporting low-pressure air out of the wake, resulting in a positive energy contribution. The radial velocity decreases at $2D$, and the pressure at the edge of the rotor-plane approaches zero after $2D$, so that this term approaches zero after $2D$.

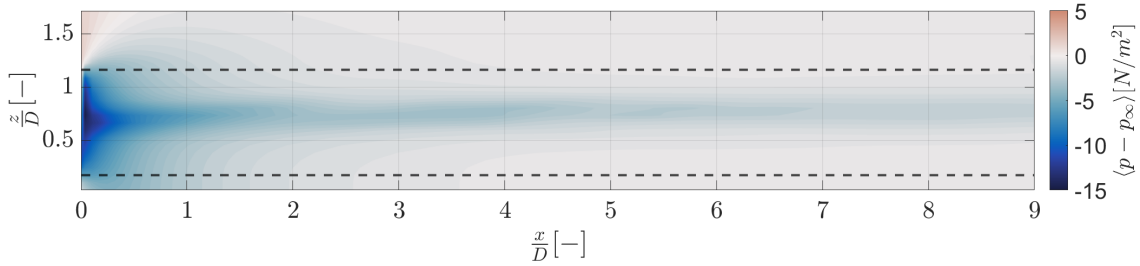


Figure 6.7: Vertical slice of the pressure field at $y = 0$ for uni_low_base. The dotted lines indicate the rotor plane cylinder.

**Turbulent kinetic energy**

Figure 6.3a shows an increase in the production of turbulent kinetic energy starting at $8D$. A vertical slice of the turbulent kinetic energy production $\mathcal{P} = \langle S_{ij} \rangle \langle u_i' u_j' \rangle$ is shown in fig. 6.8. Indeed, around $8D$ the start of a region where turbulent kinetic energy is produced can be seen. This region coincides with the region associated with the Kelvin Helmholtz Instability discussed in section 5.1.1.

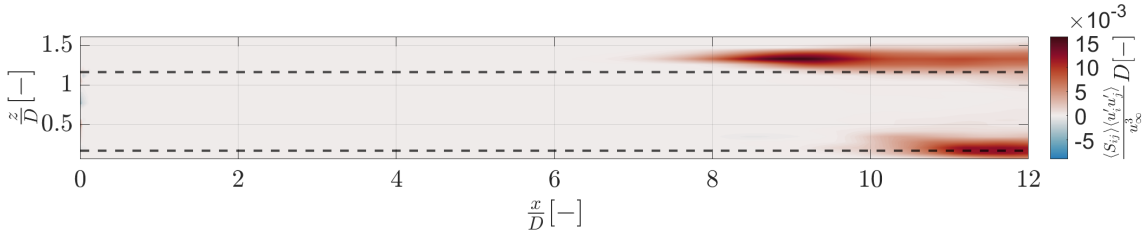


Figure 6.8: Vertical slice of the production of turbulent kinetic energy $\mathcal{P} = \langle S_{ij} \rangle \langle u_i' u_j' \rangle$, normalized by the free stream velocity $u_\infty^3$ and rotor diameter $D$, at $y = 0$ for case uni_high_base. The dotted lines indicate the rotor plane cylinder.

## 6.1.2. Transport of instantaneous kinetic energy

The spatial gradient of power can also be explained by investigating the various flux terms using the instantaneous Navier Stokes energy equation. Recalling the instantaneous Navier Stokes energy equation from chapter 4, with all terms written out and neglecting viscous terms, where the terms are colour-coded to distinguish them in figures:

$$\underbrace{\iiint_{\mathcal{V}} \left( \frac{dE}{dt} \right) d\mathcal{V}}_{\substack{\text{Time rate of change of energy} \\ \text{in control volume, purple}}} + \underbrace{\oiint_{\mathcal{S}_{disk}} (u_{ax} E \cdot \hat{n})\, d\mathcal{S}}_{\text{Power increase over control volume, blue}} = \underbrace{- \oiint_{\mathcal{S}_{wall}} (u_{rad} E \cdot \hat{n})\, d\mathcal{S}_{wall}}_{\text{Advection, green}} \underbrace{- \oiint_{\mathcal{S}_{disk}} \left( u_{ax} \frac{p}{\rho} \cdot \hat{n} \right) d\mathcal{S}_{disk}}_{\text{Axial pressure work, light brown}} \underbrace{- \oiint_{\mathcal{S}_{wall}} \left( u_{rad} \frac{p}{\rho} \cdot \hat{n} \right) d\mathcal{S}_{wall}}_{\text{Radial pressure work, dark brown}} \tag{6.5}$$

While the Reynolds Averaged Navier Stokes equations result in a time-averaged evaluation of the energy equation, the instantaneous energy equation gives an evaluation at every time step. Having the evaluation at every time step provides more insight, but also requires one more step of analysis. The temporal behaviour of the terms of slices parallel to the rotor plane at $1D$ and $10D$ downstream of the rotor is shown in fig. 6.9a and fig. 6.9b for case uni_low_base. At $1D$, the sum of the terms on the L.H.S. is a good fit to the sum of the terms on the R.H.S.. At $10D$, there are strong oscillations in all terms, but the sum of the terms on the R.H.S. captures the trend of the sum of the terms on the L.H.S..

Evaluating the individual components at $1D$ in fig. 6.9a, it can be seen that both the advection and axial pressure term are negative, matching the Reynolds Averaged Navier Stokes energy equation analysis. There is a small positive component from the radial pressure. The time rate of change of energy of the control volume oscillates around zero. Evaluating the individual components at $10D$ in fig. 6.9b, large oscillations can be seen, related to the Kelvin Helmholtz Instability. Where the time rate of change and axial pressure term in the RANS energy equation analysis were $0$ in the far wake, they can be seen to have large oscillations here. It will be shown that the mean of these oscillations is $0$, so there is no net energy contribution from the oscillations in the time rate of change and axial pressure. The power increase over the control volume and advection term show similar behaviour. It will be shown that the mean of these

terms matches. Evaluating the time resolution of the terms shows that the curves do not look smooth. The results will be more accurate when using a higher time resolution.

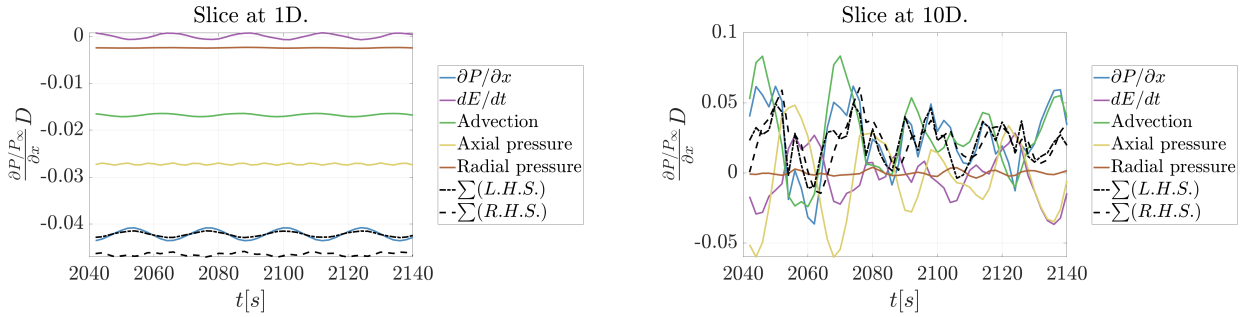


(a) Slice at $1D$.

(b) Slice at $10D$.

Figure 6.9: Temporal behaviour of terms of the instantaneous Navier Stokes equation, evaluated over a slice parallel to the rotor plane at $1D$ and $10D$ downstream of the rotor, for case uni_low_base.

Taking the temporal average of all terms, their net energy contribution as a function of downstream distance can be found. The results are shown in fig. 6.10a for case uni_high_base and fig. 6.10b for case uni_low_base. Comparing the instantaneous advection term of the Reynolds Averaged Navier Stokes energy equation to the RANS representation in fig. 6.3, similar results can be seen. The RANS approximation consists of the transport due to the mean flow (advection), work done due to turbulent fluctuations (Reynolds stress), and the transfer of energy from the mean flow field to the smaller scales ($\mathcal{P}$):

$$\underbrace{\oiint_{\mathcal{S}_{wall}} (u_{rad} E \cdot \hat{n})\, d\mathcal{S}_{wall}}_{\text{Instantaneous energy transport}} \approx \oiint_{\mathcal{S}_{wall}} \left( \underbrace{\langle u_{rad} \rangle \langle E \rangle \cdot \hat{n}}_{\substack{\text{Transport due} \\ \text{to mean flow}}} + \underbrace{\langle u_{ax} \rangle \langle u'_{ax} u'_{rad} \rangle \cdot \hat{n}}_{\substack{\text{Transport due} \\ \text{to fluctuations}}} \right) d\mathcal{S}_{wall} + \underbrace{\iiint_{\mathcal{V}} (\mathcal{P})\, d\mathcal{V}}_{\substack{\text{Transfer of energy from} \\ \text{mean flow to smaller scales}}} \tag{6.6}$$

The temporal average of the energy temporal gradient is zero since the considered flow is steady. Additionally, the temporal average of the pressure work after $5D$ is zero. Therefore, instantaneous advection is a good predictor of the spatial gradient of power after $5D$.

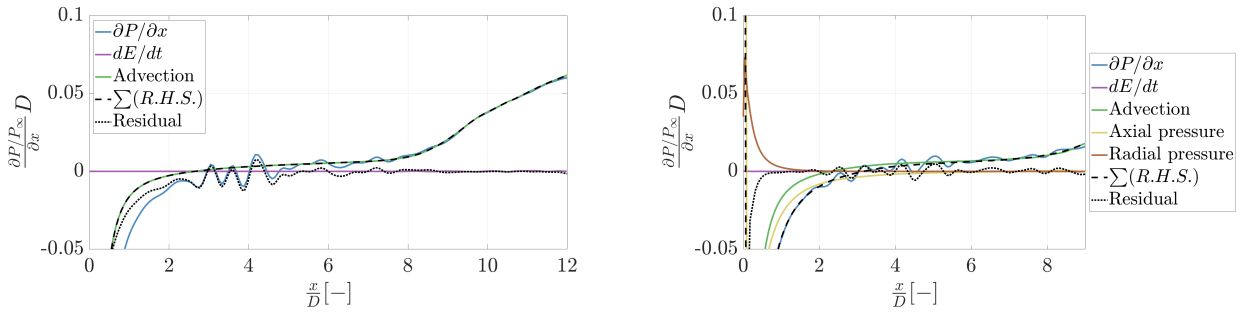


(a) Case uni_high_base.

(b) Case uni_low_base.

Figure 6.10: Components of the instantaneous Navier Stokes energy equation for case uni_high_base and case uni_low_base.

## 6.2. Baseline control, turbulent inflow

This section shows an analysis of the kinetic energy transport in the wake of a turbine with baseline control under turbulent inflow conditions. The case used to perform this analysis is turb_base.

**Power profile in the wake**

The power profile, averaged over the rotor plane and normalized by the free stream power, is shown in fig. 6.11a. The spatial gradient of the power profile is shown in fig. 6.11b. In the near-wake, between $0-1.5D$, the flow is decelerating, and the spatial gradient of power in the axial direction is negative. Around $1.5D$, the flow is no longer decelerating. The recovery is stronger than in the uniform inflow case, and the peak of the gradient appears closer to the wind turbine than in the uniform inflow case. The various components of the energy flux, in the time-averaged and instantaneous form, will be investigated to quantify where this increase comes from.

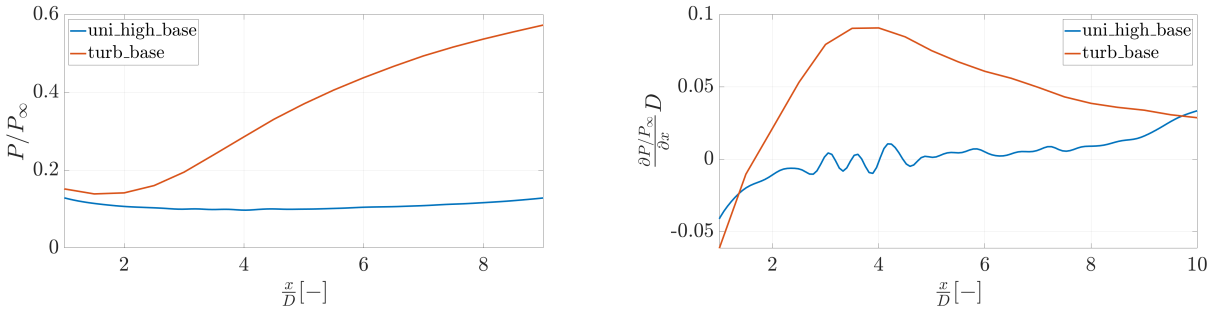


(a) Power.

(b) Spatial gradient of power.

Figure 6.11: Power and spatial gradient of power in the axial direction found from the time-averaged velocity, averaged over the rotor plane and multiplied with the rotor plane surface and normalized by the free stream power for case turb_base.

**Transport of kinetic energy**

The spatial gradient of the power profile can be explained by investigating the various flux terms. The terms computed from the Reynolds Averaged Navier Stokes energy equation are shown in fig. 6.12a. The terms computed from the instantaneous Navier Stokes energy equation are shown in fig. 6.12b. The peak of the advection and Reynolds stress term in fig. 6.12a coincide with the peak of the gradient in power. The turbulent kinetic energy production term appears in conjunction with the increase in the Reynolds stress term. Similarly, the peak of the advection term in fig. 6.12b coincides with the peak of the gradient in power. As expected, the increasing trend towards the far wake, as seen in the baseline case due to the Kelvin-Helmholtz instability, is not seen here. There is a large residual in the near-wake, which can be explained by the lack of pressure data. The trend of the residual follows the trend of the pressure flux as seen from case uni_low_base.

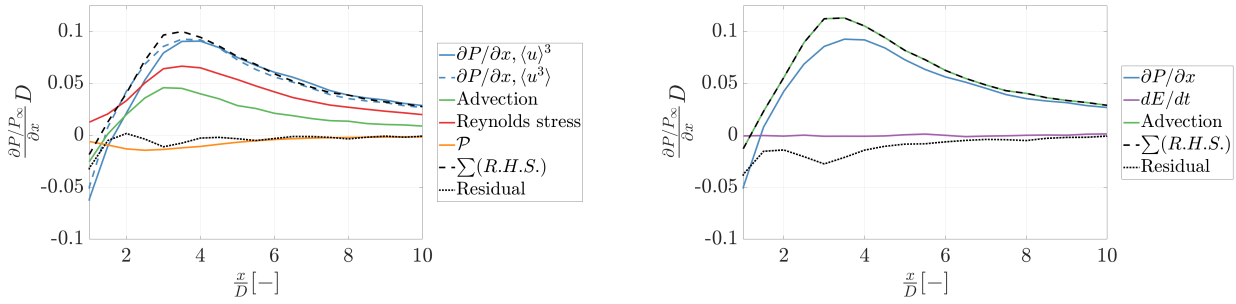


(a) Components of the Reynolds Averaged Navier Stokes energy equation.

(b) Components of the instantaneous Navier Stokes energy equation.

Figure 6.12: Components of the Reynolds Averaged Navier Stokes energy and instantaneous Navier Stokes energy equation for case turb_base.

### Advection

The evaluation of the advection term in eq. (6.3) is shown in fig. 6.12a. Advection is negative in the near-wake region and becomes positive around $1.5D$. A vertical slice of the mean radial velocity for case turb_base is shown in fig. 6.13. The radial velocity is positive in the near-wake, carrying energy out of the wake, matching the negative advection term. The radial velocity at the bottom boundary of the wake is negative starting at $1D$, carrying energy into the wake. The radial velocity term at the top boundary of the wake becomes negative around $2D$, carrying energy into the wake. This matches the positive advection term in fig. 6.12a.

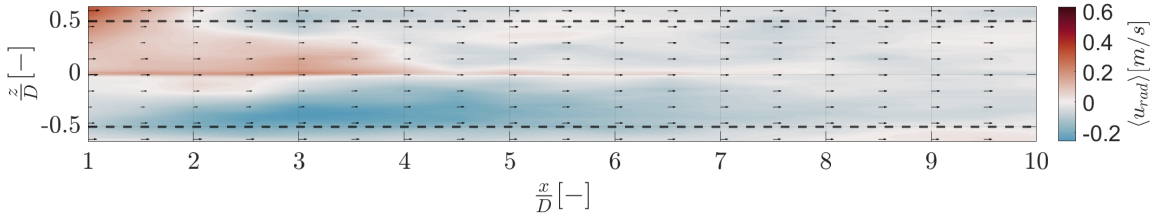


Figure 6.13: Vertical slice of the mean radial velocity $\langle u_{rad} \rangle$ at $y = 0$ for case turb_base. The dotted lines indicate the rotor plane cylinder. The quiver arrows indicate the local flow direction in the $[xz]$ plane.

### Reynolds stress

The surface integral of Reynolds stress components with a radial velocity term is shown in fig. 6.14. Similar to uniform inflow, the dominant Reynolds stress term is $\langle u_{ax} \rangle \langle u'_{ax} u'_{rad} \rangle$. The Reynolds stress flux components are only evaluated by this term.

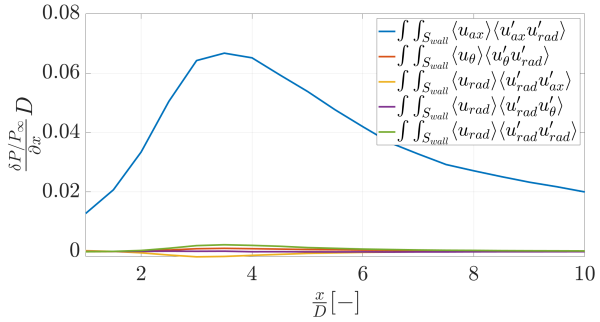


Figure 6.14: Surface integral of Reynolds stress components with a radial velocity term $u_{rad}$ for case turb_base.

Figure 6.12a shows that the Reynolds stress term is present throughout the wake and strongest in the region $2D - 7D$. A vertical slice of the dominant Reynolds stress term $\langle u_{ax}\rangle\langle u'_{ax}u'_{rad}\rangle$ is shown in fig. 6.15. Indeed, a region with a strong Reynolds stress component can be seen at the top boundary of the rotor plane starting at $2D$. The Reynolds stress component is higher at the top of the wake than at the bottom of the wake. This can be explained by the shear layer on the inflow wind profile.

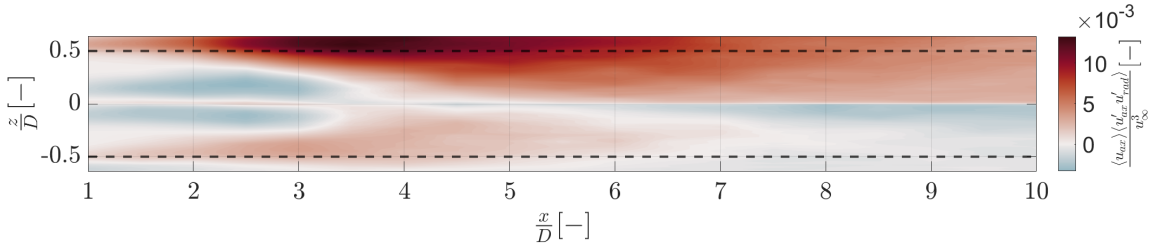


Figure 6.15: Vertical slice of the dominant Reynolds stress component $\langle u_{ax}\rangle\langle u'_{ax}u'_{rad}\rangle$, normalized by the free-stream velocity $u_\infty^3$, at $y = 0$, for case turb_base.

**Turbulent kinetic energy**

Figure 6.12a shows that the production of turbulent kinetic energy term $\mathcal{P} = S_{ij} < u'_i u'_j >$ is strongest in the region $1D - 6D$. A vertical slice of the turbulent kinetic energy production is shown in fig. 6.16. Indeed, there is a region of production of turbulent kinetic energy at the top of the rotor cylinder between $1D - 6D$. Additionally, turbulence is produced in near-wake regions $1D - 3D$ with a high-velocity gradient in the $z$-direction: the regions between the high velocity of the free-stream, low velocity in the wake, and high velocity immediately downstream of the nacelle.

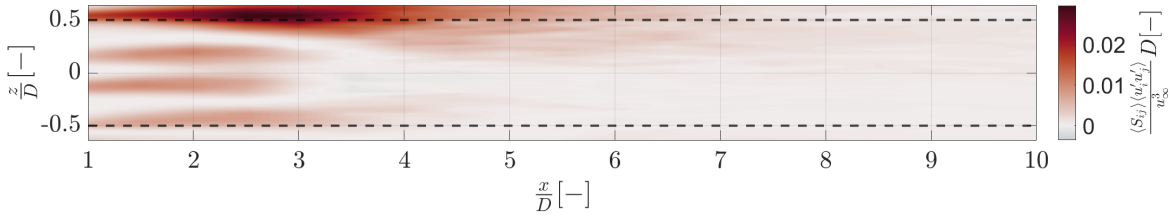


Figure 6.16: Vertical slice at $y = 0$ of the production of turbulent kinetic energy $\mathcal{P} = S_{ij} < u_i'u_j' >$ for case turb_base. $\mathcal{P}$ is normalized by the free stream velocity $u_\infty^3$ and rotor diameter $D$. The dotted lines indicate the edges of the rotor cylinder.

## 6.3. Dynamic induction control

This section shows an analysis of the kinetic energy transport in the wake of a turbine with dynamic induction control under uniform inflow conditions. The cases used to perform this analysis are uni_high_0.25 and uni_|ow_0.25.

**Power profile in the wake**

The average power in the wake is shown in fig. 6.17a for case uni_high_0.25. Additionally, two realisations of instantaneous power, found from flow field bins corresponding to an excitation signal of the blade pitch $\theta = -4^o$ and $4^o$, are shown. The peaks and valleys in power can be imagined as a travelling wave through the wake. The black dotted lines show the envelope of peaks and valleys. With an oscillating excitation signal, the instantaneous velocities and resulting power have a large, periodic deviation from the mean. This introduces an error in the average power that has been used so far, that can be characterized by Jensen's inequality:

$$\frac{1}{2}\rho A\langle u_{ax}\rangle^3 \leq \frac{1}{2}\rho A\langle u_{ax}^3\rangle \tag{6.7}$$

The more accurate $\frac{1}{2}\rho A\langle u_{ax}^3\rangle$ is found using two methods. Firstly, it is found by finding the instantaneous power for all time-steps and averaging over time. When applying this method, care needs to be taken to average over an integer number of periods of the excitation signal. Secondly, it is found using the bin approach described in section 5.3: the flow is described by one period of the actuation signal, where the simulation data is grouped into bins corresponding to the timing of the actuation signal. The instantaneous power is found for every flow field corresponding to the bins and averaged. Using this approach, the average is inherently taken over one period. Both approaches match and are shown in fig. 6.17a as $\langle u^3\rangle$.

The spatial gradient of power is shown in fig. 6.17b for power found using $\langle u\rangle^3$ and $\langle u^3\rangle$. The two gradients differ. This will be investigated further below. Additionally, the spatial gradient of two realisations of the power, found at an excitation signal of the blade pitch $\theta = -4^o$ and $4^o$ are shown. The instantaneous gradients show large deviations from the mean. The envelope of peaks and valleys is shown by the black dotted lines and is largest in the region $1D - 5D$.

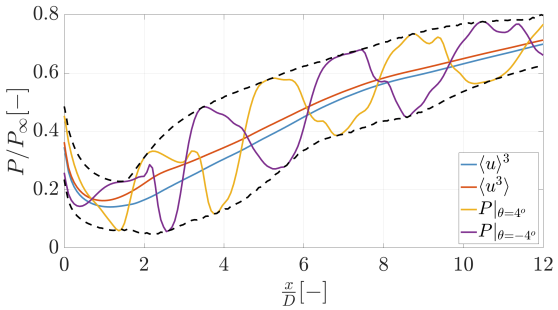


(a) Power. Dotted lines indicate the envelope of instantaneous power.

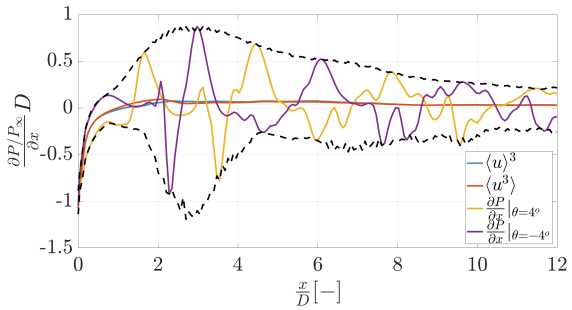


(b) Spatial gradient of power. Dotted lines indicate the envelope of the spatial gradient of instantaneous power.

Figure 6.17: Power and spatial gradient of power found from $\frac{1}{2}\rho A\langle u_{ax}\rangle^3$ and $\frac{1}{2}\rho A\langle u_{ax}^3\rangle$ for case uni_high_0.25. The power is averaged over the rotor plane and normalized by the free-stream power.

The effect of the error characterized by Jensen's equality on case uni_high_base, turb_base and uni_high_0.25 is shown in fig. 6.18. A smaller error is introduced when the fluctuations are less strong. The difference is small enough for case uni_high_base and turb_base to be in the order of the residual. However, for case uni_high_0.25 there is a large difference. The spatial gradient of instantaneous power shows a peak between $1.5 - 2.5D$. This coincides with the region where the coherent vortex ring, described in section 5.3, is seen.

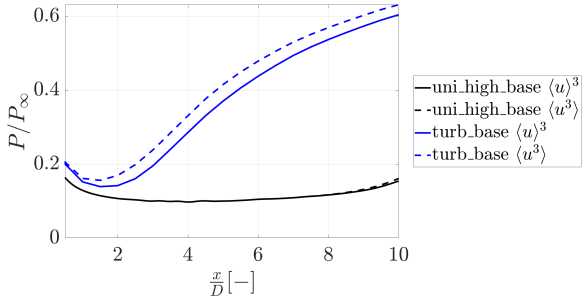


(a) Power.

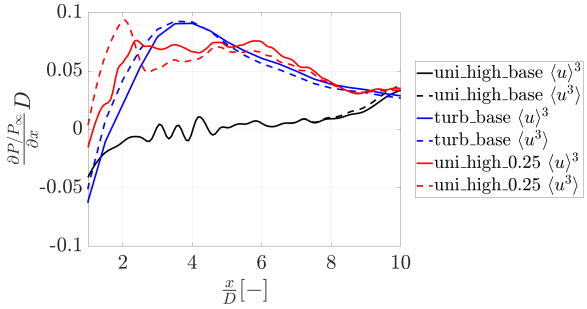


(b) Spatial gradient of power.

Figure 6.18: Power and spatial gradient of power found from $\frac{1}{2}\rho A\langle u_{ax}\rangle^3$ and $\frac{1}{2}\rho A\langle u_{ax}^3\rangle$ for case uni_high_base, turb_base and uni_high_0.25. The power is averaged over the rotor plane and normalized by the free-stream power.

### 6.3.1. Transport of instantaneous kinetic energy

The temporal behaviour of the instantaneous Navier Stokes energy equation terms of a slice at $2D$ and $5D$ downstream of the rotor is shown in fig. 6.19 for case uni_high_0.25. At $2D$, there is a large difference between the sum of the terms on the L.H.S. and the R.H.S.. This difference is expected to be caused by the lack of pressure data. At $5D$, this difference is smaller but still present.

Investigating the advection term, the working principle of dynamic induction control can be seen. The advection of energy into the wake is first positive, then negative, and then low for a while. The positive advection can be related to the region in front of the vortex ring, where there is a velocity component into the wake. The negative advection can be related to the region behind the vortex ring, where there is a velocity component out of the wake. Then, there is a low radial velocity component when there is no vortex ring present at the slice. The advection into the wake is higher than the advection out of the wake. This can be explained by the fact that high energy flow is transported into the wake, and low energy flow is transported out of the wake. The net contribution of advection is positive.

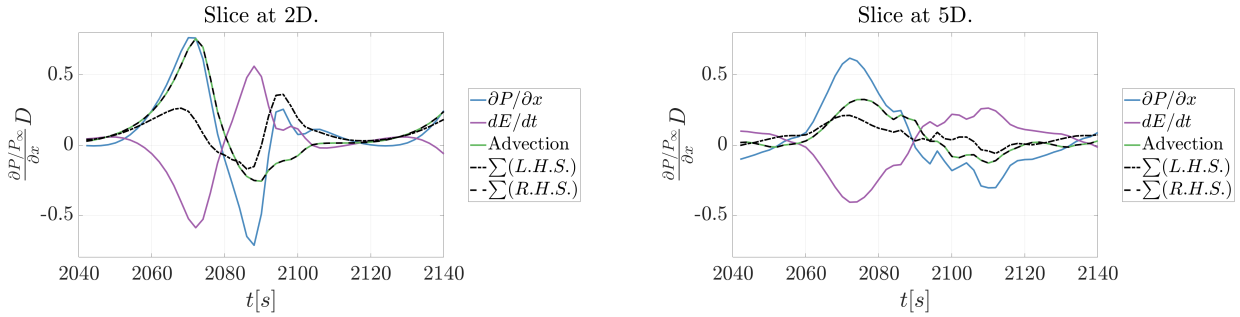


(a) Slice at $2D$.

(b) Slice at $5D$.

Figure 6.19: Temporal behaviour of components of the instantaneous Navier Stokes equation for case uni_high_0.25 at $1D$ and $5D$ downstream of the rotor.

The temporal behaviour of the instantaneous Navier Stokes energy equation terms of a slice at $2D$ and $5D$ downstream of the rotor is shown in fig. 6.20 for case uni_low_0.25. It is expected that the residual found for the slice at $2D$ is resolved, as compared to case uni_high_0.25, by taking into account pressure data. However, there is still a difference between the terms on the L.H.S. and the R.H.S..

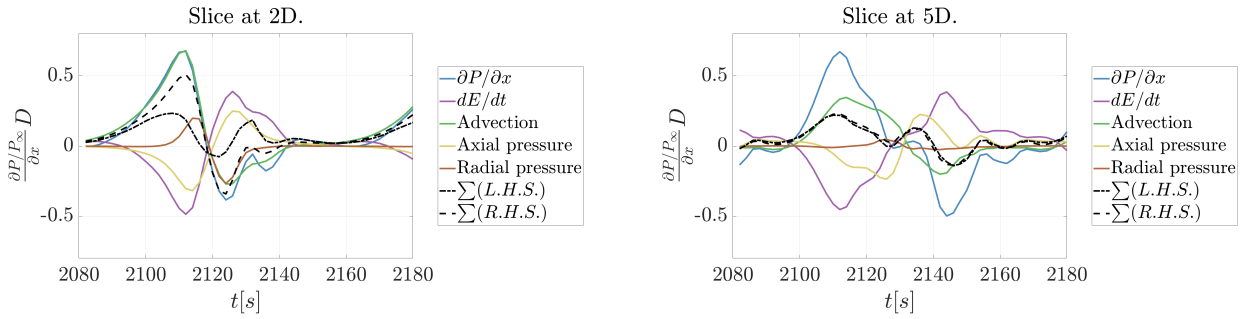


(a) Slice at $2D$.

(b) Slice at $5D$.

Figure 6.20: Temporal behaviour of components of the instantaneous Navier Stokes equation for case uni_low_0.25 at $1D$ and $5D$ downstream of the rotor.

Taking the temporal average of all terms, their net energy contribution as a function of downstream distance can be found. The results are shown in fig. 6.21a for case uni_high_0.25 and fig. 6.21b for case uni_low_0.25. Figure 6.21a shows that the advection term is a good match to the spatial gradient of power after $3D$ for case uni_high_0.25. The residual in the near wake can be explained by the lack of pressure data. Figure 6.21b shows that the sum of the advection and pressure terms is a good match to the spatial gradient of spatial gradient after $3D$ for case uni_low_0.25. Before $3D$, the temporal average of the difference shown in fig. 6.20 results in a residual. After $3D$, the temporal average of the pressure terms averages out to zero.

The behaviour of the gradient of the power profile can be related to the phenomena in the flow. Three regions can be defined: region I, before the forming of the vortex ring, region II, where the vortex ring is present, and region III, after the breakdown of the vortex ring. The kinetic energy transport in region I is dominated by pressure terms. The transition of region I to region II will be defined as the zero-crossing of the spatial gradient of power. The dominant kinetic energy transport term in region II is advection, but pressure terms are not negligible.. The transition of region II to region III will be defined as the valley in the gradient of power. Region III is dominated by advection terms and pressure terms are negligible.

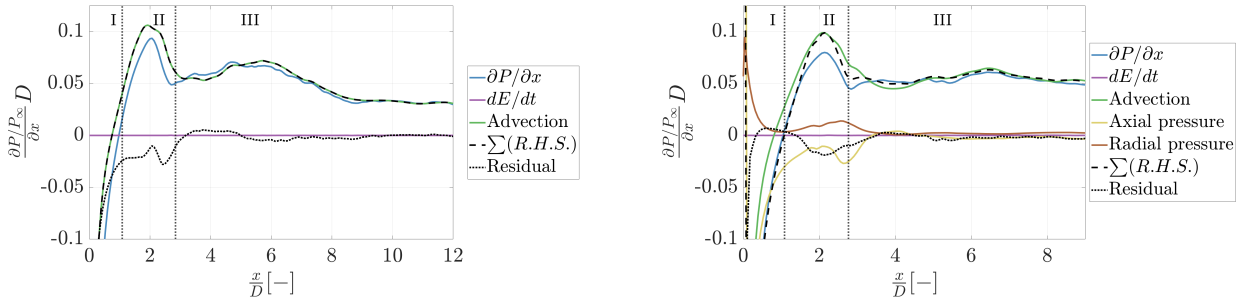


(a) Case uni_high_0.25.

(b) Case uni_low_0.25.

Figure 6.21: Components of the instantaneous Navier Stokes energy equation for case uni_high_0.25 and case uni_low_0.25. The regions corresponding to the behaviour of the vortex ring are indicated: region I, where no vortex ring is present, region II, where the vortex ring is present, and region III, where the vortex ring has broken down.

## 6.3.2. Transport of mean kinetic energy

The Reynolds Averaged Navier Stokes energy equation terms for case uni_high_0.25 and case uni_low_0.25 are shown in fig. 6.22. The sum of the terms on the R.H.S. is not a good fit to power found from $\langle u \rangle^3$. Instead, the transport of kinetic energy is compared to the power found from $\langle u^3 \rangle$. Again, a residual in the region $1D - 3D$ can be seen. However, the analysis still provides insight. In the region $1D - 3D$, there is a large contribution from the Reynolds stress term. In other words: there is high kinetic energy transport caused by fluctuating velocities.

Again, the three regions can clearly be defined. It is interesting to see that the time-averaged component of advection does not show a peak in region II, while the fluctuating component of advection in the form of Reynolds stress shows a clear peak in region II. The turbulent transport of kinetic energy is higher than in the baseline case on account of the turbulence created by the ring vortex breakdown.

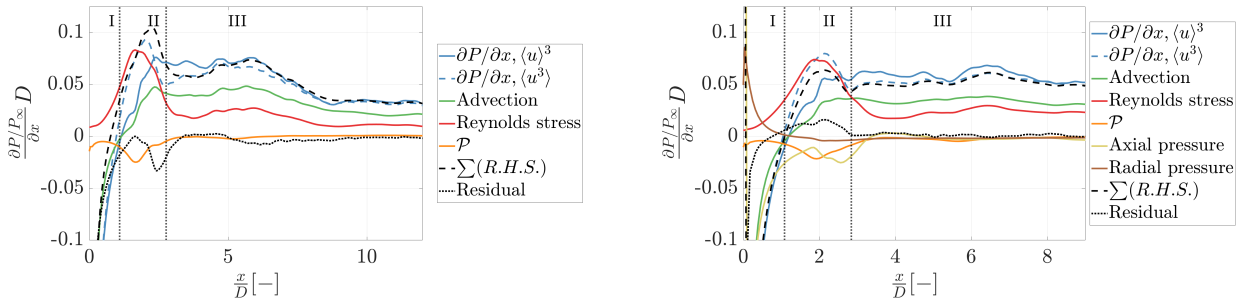


(a) Case uni_high_0.25.

(b) Case uni_low_0.25.

Figure 6.22: Components of the Reynolds Averaged Navier Stokes energy equation for case uni_high_0.25 and case uni_low_0.25. The regions corresponding to the behaviour of the vortex ring are indicated: region I, where no vortex ring is present, region II, where the vortex ring is present, and region III, where the vortex ring has broken down.

A vertical slice of the dominant Reynolds stress term $\langle u_{ax} \rangle \langle u'_{ax} u'_{rad} \rangle$ is shown in fig. 6.23. Indeed, a region of high Reynolds tress is seen until $2.5D$, where the Reynolds stress term at the top of the wake cylinder switches sign.

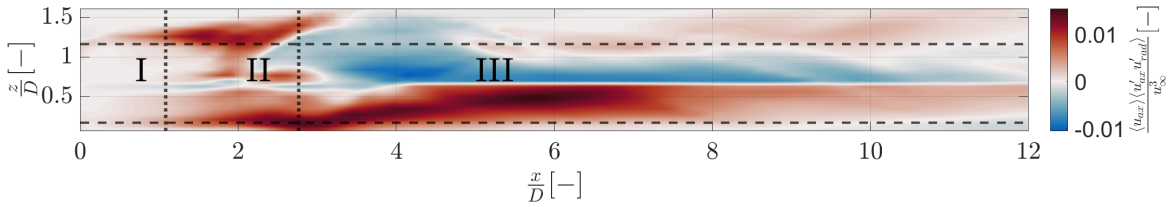


Figure 6.23: Vertical slice of the dominant Reynolds stress component $\langle u_{ax}\rangle\langle u'_{ax}u'_{rad}\rangle$, normalized by the free-stream velocity $u_\infty^3$, at $y = 0$, for case uni_high_0.25. The regions corresponding to the behaviour of the vortex ring are indicated: region I, where no vortex ring is present, region II, where the vortex ring is present, and region III, where the vortex ring has broken down.

## 6.4. Discussion

This section discusses the findings of this chapter. First, the findings for baseline control with uniform and turbulent inflow are presented. Then, the findings for dynamic induction control are discussed.

### 6.4.1. Baseline control, uniform inflow

The terms of the Reynolds Averaged Navier Stokes energy equation and the instantaneous Navier Stokes energy equation, derived in chapter 4, are evaluated in the wake of a turbine with baseline control with uniform inflow. Both methods show that they can describe the increase in power in the wake as a function of energy transport. The analysis shows that pressure data is needed to adequately describe the evolution of power in the wake in the near-wake. Additionally, a high residual near the turbine location related to the energy extraction of the rotor is present. There are fluctuations in the spatial gradient of power in the wake between $2D - 5D$ that are not well-described by the energy transport terms. They are conjectured to be related to the nacelle wake. Figure 6.9a shows that these fluctuations exist as early as $1D$. They have the same frequency as the frequency in the far-wake related to the Kelvin Helmholtz Instability. There is a small amount of energy transport before $9D$, until strong fluctuations arise related to the Kelvin Helmholtz Instability. This is the main driver of energy transport into the wake for this simulation. The instantaneous energy flux shown in a slice at $10D$ in fig. 6.9b shows that when there are large fluctuations, the time resolution of the data is not high enough to adequately capture the energy transport.

### 6.4.2. Baseline control, turbulent inflow

The evolution of power in the wake of a turbine with baseline control with turbulent inflow is very different from uniform inflow: the recovery is much higher. Evaluating the energy equations shows that this is caused by a higher Reynolds stress and advection term. The Reynolds stress is highest around $3D$ in the wake. Comparing this to the Reynolds stress found by Newman et al. (2014), shown in fig. 2.7, the region of Reynolds stress looks similar both in terms of shape and magnitude. The production of turbulent kinetic energy is located in the same region as the Reynolds stress.

Figure 6.12a can be compared to the mean kinetic equation terms found by Houtin—Mongrolle et al. (2021) in fig. 2.6a. In their plot, Houtin—Mongrolle et al. (2021) have not decomposed the surface integrals of advection and pressure. The pressure terms are combined under 'Pressure work'. The spatial gradient of power $\partial P/\partial x$ and advection term are combined under 'MKE change'. Additionally, MKE has an opposite sign in their work. Finally, the results shown in fig. 2.6a are for a wind turbine misaligned with the wind by $\gamma = 30^o$. Although different cases are considered, the general trends in MKE change, Reynolds and TKE production are similar. The residual in the near-wake shown in fig. 6.12a matches the trend of the pressure work term found by Houtin—Mongrolle et al. (2021).

### 6.4.3. Dynamic induction control

The qualitative analysis in section 5.3 showed three distinct regions in the wake of a wind turbine actuated with dynamic induction control: region I immediately downstream, where the vortex ring is not formed yet. Region II is characterised by the presence of a vortex ring. Finally, region III is defined after the breakdown of the vortex ring. Evaluating the three regions using the energy transport equations, the regions can be coupled to dominant transport terms. In region I, the transport of kinetic energy is dominated by pressure terms. In region II, the instantaneous Navier Stokes equations show that the advection into the wake, caused by the negative radial velocity behind the vortex ring, is larger than the advection out of the wake, caused by the positive radial velocity before the vortex ring. The Reynolds Averaged Navier Stokes equations show a peak in Reynolds stress in this region. It is interesting to note that these peaks correlate very well with the relative energy distribution of the Proper Orthogonal Decomposition modes related to the vortex ring found in fig. 5.29. Finally, region III is characterized by a drop of the Reynolds stress that occurs at the same location as the ring vortex breakdown. The turbulent transport in this region remains higher than that of the baseline case on account of the turbulence generated by the ring vortex breakdown.

It is shown that computing the power from the time-averaged velocities introduces an error that can be characterized by Jensen's inequality. While this error remains small for the baseline control simulations, the error in the power and the gradient of the power becomes large when applying dynamic induction control. Therefore, the Reynolds Averaged Navier Stokes energy terms are related to the power found from $\langle u^3 \rangle$. A more accurate way to assess this would be to use the Reynolds work term $\langle u_{ax} \rangle \langle u_{ax' u'_{ax}} \rangle$. This is not implemented here for practical reasons.

The quantitative results show a good match with the qualitative results, and provide additional insight. However, there is a relatively large residual in region II. For the instantaneous energy equation shown in fig. 6.21b, this difference could be explained by the neglected viscous transport term, the sub-filter scale stress tensor or the viscous dissipation term, as discussed in chapter 4:

$$\text{residual} = \frac{\partial}{\partial x_i}\left(-2\nu u_j S_{ij}\right) - \frac{\partial \tau_{ij}}{\partial x_i} + u_j f_j - \epsilon \tag{6.8}$$

For the Reynolds Averaged energy equation shown in fig. 6.22b, the neglected terms are:

$$\text{residual} = \frac{\partial}{\partial x_i}\left(-2\nu \langle u_j \rangle \langle S_{ij} \rangle\right) - \frac{\partial \tau_{ij}}{\partial x_i} + \langle u_j \rangle \langle f_j \rangle - \epsilon \tag{6.9}$$

However, the error is more likely to be caused by other factors. The error for the instantaneous energy equation could be explained by insufficient temporal resolution. The error for the Reynolds Averaged energy equation could be explained by:

$$\langle u_{rad} \rangle \langle p \rangle \neq \langle u_{rad} p \rangle \tag{6.10}$$

Further research on the residual is recommended to fully understand the transport of energy from the free stream to the wake. Finally, it is interesting to note that the energy transport found for the case uni_high_0.25 and case uni_low_0.25 differs by quite a lot. The general trend of the location of the regions is similar, but the magnitude of the energy transport terms is not. A grid convergence study to determine the necessary spatial and temporal resolution to capture the dynamics is recommended.

# 7

# Evaluating actuation frequencies

This chapter gives a brief comparison between dynamic induction control cases with different actuation frequencies. No further analysis is performed, and the findings will mostly serve as the basis of recommendations for further research.

**Evaluating the spatial gradient of power**

The power and spatial gradient of power for dynamic induction control with different actuation frequencies is shown in fig. 7.1. As seen before, the baseline control case with turbulent inflow has a dramatically improved wake recovery as compared to the baseline control case with uniform inflow. Similarly, the dynamic induction control cases show a peak recovery in the region associated with the vortex ring, and improved recovery in the region after the breakdown of the vortex ring. Evaluating the three dynamic induction control cases computed in the low-resolution SOWFA environment, it can be seen that they perform differently in the three regions defined in section 6.4.3. The recovery is shown in fig. 7.1b. In the near-wake region I, dominated by pressure, the wake recovery is highest for a low actuation frequency. In region II, dominated by the vortex ring, the low frequency has the highest wake recovery. Finally, in region III, the recoveries are similar. The wake recoveries are ordered from high-frequency to low-frequency or the other way around, and there does not seem to be an optimum for the $St = 0.25[-]$ case. The difference in effectiveness of the three actuation frequencies is influenced by the intensity of the vortex ring, that determines the peak of the advection component into the wake, and the breakdown location of the vortex ring, that determines the length of the peak of the advection component. Comparing the different powers in the wake to the ones found by Frederik et al. (2020a) shown in fig. 2.12, the trend does not match. Frederik et al. (2020a) found a significant power improvement at $5D$ for a case with $St = 0.25[-]$ as compared to other actuation frequencies, whereas here the powers are very close together. A possible explanation for this can be seen when comparing the power found from the low-resolution cases to the power found for the high-resolution dynamic induction control case. It can be expected that when the resolution is sufficiently high, the two results should be similar. However, there is a large difference between the power in the wake found for the high-resolution and low-resolution wake. It can be concluded that either the time resolution or the spatial resolution for the low-resolution case is not sufficient. For further research on finding an effective actuation frequency, it is recommended that a grid refinement study is performed. In such a study, the case is computed with varying resolutions. When the resolution is high enough, the solutions will converge.

When comparing the improvement in wake recovery of the dynamic control cases with the improvement in wake recovery caused by turbulent inflow, the magnitude of the effect is similar. It is hard to say what the effect of dynamic induction control would be under turbulent inflow based on the analysis in this thesis. It is expected that the peak in transport of kinetic energy in region II remains in turbulent inflow, while the increase in region III will be limited.

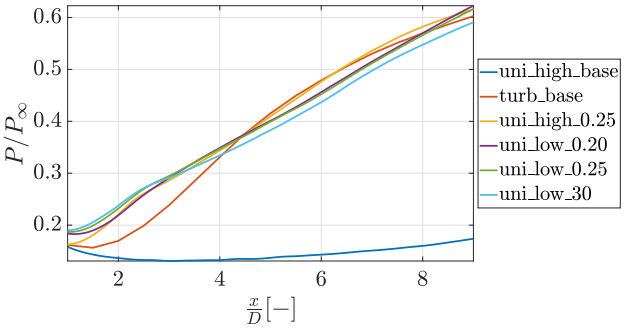


(a) Power.

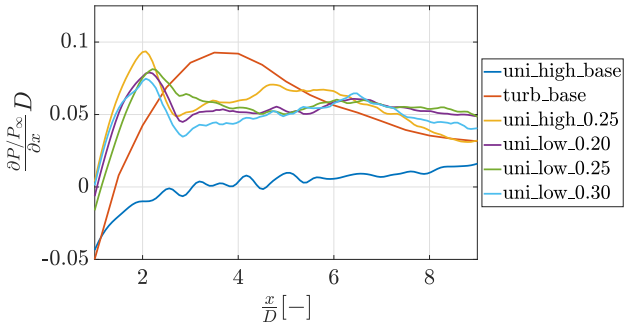


(b) Spatial gradient of power in the axial direction $\partial P/\partial x$, normalized by the rotor diameter $D$.

Figure 7.1: Power and spatial gradient of power for different actuation frequencies. Uniform and turbulent inflow baseline cases are also shown for reference.

### Dynamic inflow

The time behaviour of the thrust coefficient $C_T$ is shown in fig. 7.2. The thrust coefficient for the baseline case can be seen to be constant in time. The thrust coefficient for case uni_low_theta_4 and case uni_low_theta_-4 shows a transient behaviour at $t = 0[s]$. This is because the flow field is established by running the simulation for $1000[s]$. Then, at $t = 1000[s]$, the blade pitch $\theta$ is set to $4^o$ or $-4^o$, effectively imposing a step function on the pitch. The transient behaviour is a result of the wake needing some time to adjust to the changed rotor parameters. This process is known as dynamic inflow, and usually occurs from a time-varying wind speed. Models to capture this effect are described by Yu (2018). It can be seen that the varying excitation frequencies for the low-resolution cases, show different peak thrust coefficients. The highest actuation frequency has the highest peak of the thrust coefficient, and approaches the value achieved by the step function, that is the upper limit of that can be achieved by pitching the blades at this amplitude. The thrust coefficient of the high-resolution dynamic induction control case is higher than the thrust coefficient of the low-resolution case with the same frequency. They are expected to be similar, given the same inflow conditions that are applied here. An explanation for the higher thrust coefficient can be the low time-resolution for the low-resolution case. The blade tip is passing multiple grid points in one computation step, resulting in inaccuracies. The difference in thrust coefficient is probably the main reason for the difference in the power in the wake shown in fig. 7.1. Despite the limitations of the low-resolution case, it is interesting to see the effect of the actuation frequency on the peak thrust coefficient $C_T$, and it is likely that the optimum actuation frequency is at least partly reliant on this phenomenon.

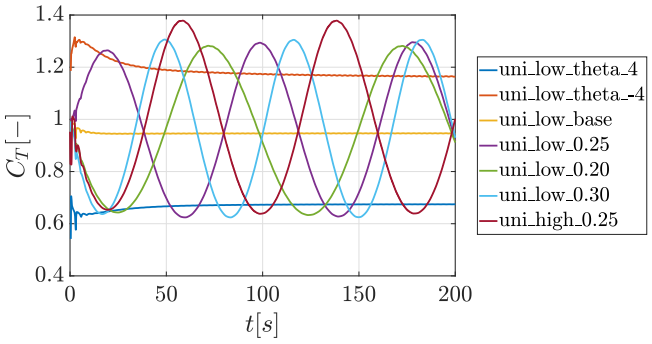


Figure 7.2: Time behaviour of the thrust coefficient $C_T$ for varying inflow cases.

# 8

# Conclusions and recommendations

This chapter will provide an overview of the conclusions that can be drawn based on the analysis performed in this thesis, answering the research questions. Then, recommendations are given for further research. Finally, the main contributions of this work are summarised.

## 8.1. Conclusions

Clustering wind turbines in wind farms results in wake losses. A potential solution to mitigate these losses is wind farm control, which is to deviate from optimal individual wind turbine operation in order to improve a total wind farm objective. A novel research direction within wind farm control is dynamic control, where an upstream wind turbine is dynamically actuated in order to promote wake recovery. Dynamic control is showing promising results in research, but the aerodynamic phenomena underlying the wake recovery are not yet well understood. This thesis aims to elucidate the working principle behind dynamic induction control.

In order to provide quantitative insight in the transfer of kinetic energy from the free stream to the wake, the instantaneous and Reynolds Averaged Navier Stokes energy equations are used. The RANS energy equation has seen much use in literature related to wake recovery. Because of the highly time-varying nature of dynamic induction control, this work proposes the use of the instantaneous Navier Stokes energy equations to analyze the flow. A derivation for the transport of kinetic energy into a cylindrical control volume in a wind turbine wake is provided for the instantaneous and Reynolds Averaged Navier Stokes energy equation, showing similarities but also slight differences in the derivation between the two approaches.

The dominant phenomenon in the wake for a wind turbine with baseline control simulated with uniform inflow is the Kelvin Helmholtz Instability. This instability occurs under specific flow conditions: an approximately step difference in the axial velocity over the interface between the wake and the free stream. The result of the Kelvin Helmholtz Instability is that any small perturbation of the interface shape will exponentially grow in space and time. Using Proper Orthogonal Decomposition, this behaviour can indeed be seen: a perturbation at $St \approx 0.8[-]$ that grows in the wake. The onset of the instability can already be seen in the temporal behaviour of the kinetic energy at $1D$ downstream of the wind turbine.

Analysis of the wake of a wind turbine with baseline control simulated with turbulent inflow does not show the Kelvin Helmholtz Instability. The necessary flow conditions at the interface are disturbed by the turbulent flow. Instead, analysis through Proper Orthogonal Decomposition shows that the dominant phenomenon in the flow is wake meandering at a frequency of $St \approx 0.2[-]$. This is confirmed by finding the wake center with the Weighted Geometric-Center Approach. The dominant direction of wake meandering is side-to-side. Analysis from the energy equations show that the recovery is much higher than for uniform inflow, and that the peak of the Reynolds stress occurs at $3D$ in the wake.

Analysis of the wake of a wind turbine with dynamic induction control show that three regions can be defined: the near-wake region dominated by pressure terms, the vortex ring region dominated by advection and Reynolds stress terms, and the region after the vortex breakdown, dominated by turbulent fluctuations.

The transition from region I to region II is characterised by going from a deceleration of the flow in region I to acceleration of the flow in region II. This occurs at $1D$. The transition of the second region to the third region is triggered by the breakdown of the vortex ring. This occurs at $3D$. In region II, there is a an upward radial velocity before the vortex ring and a negative radial velocity after the vortex ring. Analysis of the instantaneous Navier Stokes energy equations shows that more energy is carried into the wake by the negative radial component, than is carried out of the wake by the positive radial velocity component. In region III, the turbulence intensity has increased as compared to baseline control, leading to increased wake recovery even after the ring vortex breakdown.

In the simulation used in this work, uniform inflow and not modelling the nacelle, the transition from region II to region III is triggered by the interaction of an inner vortex ring with the outer vortex ring. This inner vortex ring arises from the nacelle wake. The nacelle wake is an artefact of the simulation and not physical. Therefore, the ring vortex breakdown location predicted with the current simulation does not have much physical meaning. Additionally, the temporal resolution used in the low-resolution SOWFA cases is too low to accurately describe the thrust coefficient. Therefore, the relation between flow and wind farm parameters and effective settings for dynamic induction control could not be established based on the analysis in this research. However, it is shown that dynamic inflow effects can be of influence. Additionally the intensity of the vortex ring and downstream distance of the breakdown location of the vortex ring are of importance to the effectiveness of dynamic induction control.

While there remains a lot of work to be done, this thesis confirms the potential of dynamic induction control shown in previous research. A particularly interesting aspect of dynamic induction control shown in this thesis is that a high amount of wake recovery is compressed into a short distance in the order of $3D$. This property makes dynamic induction control a potential way to decrease turbine spacing in wind farms, allowing the placement of more wind turbines on the same area.

## 8.2. Recommendations

While this research has not succeeded in establishing effective settings for dynamic induction control, it has provided some of the groundwork needed for further research. Firstly, the working principle of dynamic induction control is qualitatively described. Secondly, a framework for investigating the transport of kinetic energy is provided. Recommendations are given for the simulation set-up, evaluating the effect on the downstream wind turbine, flow analysis and actuation signal.

**Simulation set-up**

It has been shown that the breakdown location of the ring vortex is of importance to the effectiveness of dynamic induction control, but that the breakdown location predicted by the current simulation set-up does not have much physical meaning. It is recommended to investigate the interaction of the ring vortex with a more realistic simulation set-up. Possible additions to the simulation set-up include:

- Nacelle model
- Tower model
- Turbulent inflow
- Shear layer on the inflow wind profile

These additions result in a frequency component in the wake. For example, a tower model introduces frequency components in the wake in the form of a von Kármán vortex street (De Cillis et al., 2020) and turbulent inflow introduces wake meandering (Andersen et al., 2013). It is likely that these phenomena will interact with the vortex ring. Using these additions will provide a prediction of the ring vortex breakdown location with more physical meaning.

Part of the effectiveness of dynamic induction control comes from the increased turbulence intensity in region III. It would be interesting to see what the effect of the ring vortex breakdown is on the turbulence intensity in region III when there is already turbulence naturally present.

Finally, it is shown that the low-resolution cases used in this research suffer from a too low time-resolution. It is recommended to perform a grid refinement study, taking into account spatial and temporal resolution. The solutions will converge when the resolution is high enough, providing a means to validate the used simulation environment.

**Downstream wind turbine**
The goal of dynamic induction control is to increase kinetic energy recovery in the wake for a downstream wind turbine to benefit from that energy. Frederik et al. (2020a) found that the most effective actuation frequency depends on the turbine spacing. This finding is not replicated in this research. However, it is also shown that the data used to attempt to replicate this result is suffering from a too low temporal resolution. It is recommended to replicate the result by Frederik et al. (2020a), while also taking into account the additions to the simulation set-up mentioned above.

**Flow analysis**
The provided framework to evaluate the transport of kinetic energy using the Reynolds Averaged and instantaneous Navier Stokes energy equation has created insight into the flow. However, there is a residual in region II, a region with large oscillations, that could not be explained. For the instantaneous Navier Stokes energy equation, it is unclear what is causing the residual. Possibilities include incorrectly neglecting the viscous terms, a too low time or spatial resolution, or a mistake in the implementation. For the Reynolds Averaged Navier Stokes energy equation, it is shown that:

$$\langle u_{rad} \rangle \langle p \rangle \neq \langle u_{rad} p \rangle \tag{8.1}$$

This could be solved by applying Reynolds decomposition on the pressure and further deriving the equations:

$$p = \langle p \rangle + p' \tag{8.2}$$

This research has shown the use of Proper Orthogonal Decomposition to identify coherent spatial and temporal modes in the wake. An interesting aspect of POD is that it can be combined with the energy transport equations to find the kinetic energy transport per mode, as shown by De Cillis et al. (2020). This can be used to further understand the kinetic energy transport contribution of individual phenomena.

An alternate to using Proper Orthogonal Decomposition to find coherent spatial and temporal modes in the wake is Dynamic Mode Decomposition (Kutz et al., 2016). Both approaches are based on the Singular Value Decomposition. One of the main differences is that Proper Orthogonal Decomposition decomposes the signal into spatially orthogonal modes, whereas Dynamic Mode Decomposition decomposes the signal into temporally orthogonal modes. In other words: POD modes can show peaks at multiple temporal frequencies, whereas DMD decomposes the signal into modes that sinusoidally oscillate at a single frequency. This can be an advantage when linking a spatial mode to a purely sinusoidal actuation signal.

**Actuation signal**
The control signal applied on the blade pitch in this research is sinusoidal. However, inspecting the time evolution of the thrust coefficient found by an adjoint-based optimization by fig. 2.10a looks more like a saw-tooth signal. The thrust is increased in a single step and then gradually decreased, until it is increases with a step again. Increasing the pitch in a single step results in a peak thrust coefficient as a result of the dynamic inflow effect, and this could potentially be a more effective actuation signal. This will introduce different loads on the blade, that will also need to be taken into account.

## 8.3. Contribution to the field

Despite the limitations imposed by the available simulations, several important and valid concepts have been formulated that can aid further research on dynamic induction control.

- A framework is provided to evaluate the transport of kinetic energy into a cylindrical control volume in a wind turbine wake using the instantaneous Navier Stokes energy equation. This approach can be used to provide insight into the time behaviour of kinetic energy transport. The approach can be used in conjunction with the Reynolds Averaged Navier Stokes energy equation.
- The working principle of dynamic induction control is qualitatively described, by dividing the wake in three regions: region I, dominated by pressure, region II, dominated by a vortex ring and region III, dominated by turbulence. The peak of transport of kinetic energy occurs in region II, as is confirmed by analysis through the instantaneous Navier Stokes energy equations.
- In a simulation with uniform inflow and where the effect of the nacelle is not modelled, the transition from region II to region III is triggered by interaction of the outer vortex ring with an inner vortex ring that forms around the nacelle wake. The nacelle wake is a result of not modelling the nacelle and deemed non-physical, so the ring vortex breakdown location that arises from this simulation does not have much physical meaning.

# Bibliography


J F Ainslie. Journal of Wind Engineering and Industrial Aerodynamics, 27 (1988) 213-224. *Journal of Wind Engineering*, 27(1-3):213–224, 1988. URL http://linkinghub.elsevier.com/retrieve/pii/0167610588900372.

Søren Juhl Andersen, Jens N. Sørensen, and Robert F. Mikkelsen. Simulation of the inherent turbulence and wake interaction inside an infinitely long row of wind turbines. *Journal of Turbulence*, 14(4):1–24, 2013. ISSN 14685248. doi: 10.1080/14685248.2013.796085.

Søren Juhl Andersen, Jens Nørkær Sørensen, and Robert F. Mikkelsen. Turbulence and entrainment length scales in large wind farms. *Philosophical Transactions of the Royal Society A: Mathematical, Physical and Engineering Sciences*, 375 (2091), 2017. ISSN 1364503X. doi: 10.1098/rsta.2016.0107.

Jennifer Annoni, Pieter M. O. Gebraad, Andrew K. Scholbrock, Paul A. Fleming, and Jan-Willem van Wingerden. Analysis of axial-induction-based wind plant control using an engineering and a high-order wind plant model. *Wind Energy*, 19:1135–1150, 2016. doi: 10.1002/we.1891.

Christian Bak, Frederik Zahle, Robert Bitsche, Taeseong Kim, Anders Yde, Lars Christian Henriksen, Anand Natarajan, and Morten Hartvig Hansen. Description of the DTU 10 MW Reference Wind Turbine. *DTU Wind Energy Report*, I-0092(July), 2013.

R. J. Barthelmie, S. T. Frandsen, K. Hansen, J. G. Schepers, K. Rados, W. Schlez, A. Neubert, L. E. Jensen, and S. Neckelmann. Modelling the impact of wakes on power output at Nysted and Horns Rev. *European Wind Energy Conference and Exhibition 2009, EWEC 2009*, 2(October 2015):1351–1373, 2009.

G. Berkooz, P. Holmes, and J. L. Lumley. The proper orthogonal decomposition in the analysis of turbulent flows. *Annu. Rev. Fluid Mech.*, 25:539–575, 1993. ISSN 00664189. doi: 10.1146/annurev.fluid.25.1.539.

S. Boersma, B. M. Doekemeijer, P. M.O. Gebraad, P. A. Fleming, J. Annoni, A. K. Scholbrock, J. A. Frederik, and J. W. Van Wingerden. A tutorial on control-oriented modeling and control of wind farms. *Proceedings of the American Control Conference*, 2017. ISSN 07431619. doi: 10.23919/ACC.2017.7962923.

Kenneth Brown, Daniel Houck, David Maniaci, and Carsten Westergaard. Rapidly recovering wind turbine wakes with dynamic pitch and rotor speed control. In *AIAA Scitech 2021 Forum*, pages 1–16, 2021. ISBN 9781624106095. doi: 10.2514/6.2021-1182.

Tony Burton. *Wind Energy Handbook*. Wiley, 2nd edition, 2001. ISBN 0471489972.

Filippo Campagnolo, Vlaho Petrović, Carlo L. Bottasso, and Alessandro Croce. Wind tunnel testing of wake control strategies. *Proceedings of the American Control Conference*, 2016-July:513–518, 2016. ISSN 07431619. doi: 10.1109/ACC.2016.7524965.

Matthew J. Churchfield, Zhixiang Wang, and Sven Schmitz. Modeling wind turbine tower and nacelle effects within an actuator line model. In *33rd Wind Energy Symposium*, 2015. ISBN 9781624103445. doi: 10.2514/6.2015-0214.

Giovanni De Cillis, S. Cherubini, O. Semeraro, S. Leonardi, and P. De Palma. POD analysis of the recovery process in wind turbine wakes. *Journal of Physics: Conference Series*, 1618(6), 2020. ISSN 17426596. doi: 10.1088/1742-6596/1618/6/062016.

Sten Frandsen, Rebecca Barthelmie, Sara Pryor, Ole Rathmann, Søren Larsen, Jørgen Højstrup, and Morten Thøgersen. Analytical modelling of wind speed deficit in large offshore wind farms. *Wind Energy*, 9(1-2):39–53, 2006. ISSN 10991824. doi: 10.1002/we.189.

Joeri A. Frederik, Bart M. Doekemeijer, Sebastiaan P. Mulders, and Jan Willem van Wingerden. The helix approach: Using dynamic individual pitch control to enhance wake mixing in wind farms. *Wind Energy*, 23(8):1739–1751, 2020a. ISSN 10991824. doi: 10.1002/we.2513.

Joeri Alexis Frederik, Robin Weber, Stefano Cacciola, Filippo Campagnolo, Alessandro Croce, Carlo Bottasso, and Jan-Willem van Wingerden. Periodic dynamic induction control of wind farms: proving the potential in simulations and wind tunnel experiments. *Wind Energy Science*, 5(1):245–257, 2020b. ISSN 2366-7443. doi: 10.5194/wes-5-245-2020.

Pieter M O Gebraad. *Data-Driven Wind Plant Control, PhD Thesis*. PhD thesis, TU Delft, 2014.

Pieter M.O. Gebraad and J. W. Van Wingerden. A control-oriented dynamic model for wakes in wind plants. *Journal of Physics: Conference Series*, 524(1), 2014. ISSN 17426596. doi: 10.1088/1742-6596/524/1/012186.

H. Glauert. AIRPLANE PROPELLERS. In William Frederick Durand, editor, *Aerodynamic Theory*, pages 169–360. Springer, 1935. ISBN 978-3-642-89630-9. doi: https://doi.org/10.1007/978-3-642-91487-4.

Tuhfe Göçmen, Paul Van Der Laan, Pierre Elouan Réthoré, Alfredo Peña Diaz, Gunner Chr Larsen, and Søren Ott. Wind turbine wake models developed at the technical university of Denmark: A review. *Renewable and Sustainable Energy Reviews*, 60:752–769, 2016. ISSN 18790690. doi: 10.1016/j.rser.2016.01.113. URL http://dx.doi.org/10.1016/j.rser.2016.01.113.

Jay P. Goit and Johan Meyers. Optimal control of energy extraction in wind-farm boundary layers. *Journal of Fluid Mechanics*, 768:5–50, 2015. ISSN 14697645. doi: 10.1017/jfm.2015.70.

Martin Hansen. *Aerodynamics of wind turbines*. Routledge, 3rd edition, 2015. ISBN 0898711657. doi: 10.1002/9781119994367.ch3.

Charlotte Bay Hasager, Nicolai Gayle Nygaard, Patrick J.H. Volker, Ioanna Karagali, Søren Juhl Andersen, and Jake Badger. Wind farm wake: The 2016 Horns Rev photo case. *Energies*, 10(3), 2017. ISSN 19961073. doi: 10.3390/en10030317.

F. Houtin—Mongrolle, P. Benard, G. Lartigue, and V. Moureau. A level-set framework for the wind turbine wake analysis: from high-fidelity unsteady simulations to 1D momentum theory. *Journal of Physics: Conference Series*, 1934(1): 012011, 2021. ISSN 1742-6588. doi: 10.1088/1742-6596/1934/1/012011.

J C R Hunt, a a Wray, and P Moin. Eddies, streams, and convergence zones in turbulent flows. *Center for Turbulence Research, Proceedings of the Summer Program*, 1(1970):193–208, 1988.

N O Jensen. A note on wind generator interaction. *Risø-M-2411 Risø National Laboratory Roskilde*, pages 1–16, 1983. ISSN 01676105. URL http://www.risoe.dk/rispubl/VEA/veapdf/ris-m-2411.pdf.

Ángel Jiménez, Antonio Crespo, and Emilio Migoya. Application of a LES technique to characterize the wake defl ection of a wind turbine in yaw. *Wind Energy*, 13(December 2009):559–572, 2010. doi: 10.1002/we.380.

Kathryn E. Johnson and Naveen Thomas. Wind farm control: addressing the aerodynamic interaction among wind turbines. *Proceedings of the American Control Conference*, pages 2104–2109, 2009. ISSN 07431619. doi: 10.1109/ACC.2009.5160152.

I. Katic, J. Højstrup, and N.O. Jensen. A Simple Model for Cluster Efficiency. *European wind energy association conference and exhibition*, 1, 1987.

Ali C. Kheirabadi and Ryozo Nagamune. A quantitative review of wind farm control with the objective of wind farm power maximization. *Journal of Wind Engineering and Industrial Aerodynamics*, 192(March):45–73, 2019. ISSN 01676105. doi: 10.1016/j.jweia.2019.06.015. URL https://doi.org/10.1016/j.jweia.2019.06.015.

Pijush Kundu, Ira Cohen, and David Dowling. *Fluid Mechanics*. Academic Press, 2015. ISBN 9780124059351.

J. Nathan Kutz, Steven L. Brunton, Bingni W. Brunton, and Joshua L. Proctor. Dynamic Mode Decomposition: Data-Driven Modeling of Complex Systems. *Society for Industrial and Applied Mathematics*, page 234, 2016.

Gunner C. Larsen, Helge Aa Madsen, Kenneth Thomsen, and Torben J. Larsen. Wake meandering: A pragmatic approach. *Wind Energy*, 11(4):377–395, 2008. ISSN 10954244. doi: 10.1002/we.267.

Jaime Liew, Albert M. Urbán, and Søren Juhl Andersen. Analytical model for the power-yaw sensitivity of wind turbines operating in full wake. *Wind Energy Science*, 5(1):427–437, 2020. ISSN 23667451. doi: 10.5194/wes-5-427-2020.

Jakob Mann. The Spatial Structure of Neutral Atmospheric Surface-Layer Turbulence. *Journal of Fluid Mechanics*, 273: 141–168, 1994. ISSN 14697645. doi: 10.1017/S0022112094001886.

Jakob Mann. Wind field simulation. *Probabilistic Engineering Mechanics*, 13(4):269–282, 1998. ISSN 02668920. doi: 10.1016/s0266-8920(97)00036-2.

Charles Meneveau and Joseph Katz. SCALE-INVARIANCE AND TURBULENCE MODELS FOR LARGE-EDDY SIMULATION. *Annu. Rev. Fluid Mech.*, pages 1–32, 2000.

Wim Munters and Johan Meyers. Dynamic strategies for yaw and induction control of wind farms based on large-eddy simulation and optimization. *Energies*, 11(1), 2018a. ISSN 19961073. doi: 10.3390/en11010177.

Wim Munters and Johan Meyers. Towards practical dynamic induction control of wind farms: Analysis of optimally controlled wind-farm boundary layers and sinusoidal induction control of first-row turbines. *Wind Energy Science*, 3(1):409–425, 2018b. ISSN 23667451. doi: 10.5194/wes-3-409-2018.

Juan Pablo Murcia Leon. *Uncertainty quantification in wind farm flow models*. PhD thesis, DTU, 2017.

A. Jensen Newman, Donald A. Drew, and Luciano Castillo. Pseudo spectral analysis of the energy entrainment in a scaled down wind farm. *Renewable Energy*, 70:129–141, 2014. ISSN 09601481. doi: 10.1016/j.renene.2014.02.003. URL http://dx.doi.org/10.1016/j.renene.2014.02.003.

Karl Nilsson, Stefan Ivanell, Kurt S. Hansen, Robert Mikkelsen, Jens N. Sørensen, Simon-Philippe Breton, Dan Henningson, and 1. Large-eddy simulations of the Lillgrund wind farm. *Wind Energy*, 18:449–467, 2015. doi: 10.1002/we.1707.

Stephen B. Pope. *Turbulent flows*. Cambridge University Press, 2000.

Fernando Porté-Agel, Majid Bastankhah, and Sina Shamsoddin. *Wind-Turbine and Wind-Farm Flows: A Review*, volume 174. Springer Netherlands, 2020. ISBN 1054601900473. doi: 10.1007/s10546-019-00473-0. URL https://doi.org/10.1007/s10546-019-00473-0.

B Sanderse. Aerodynamics of wind turbine wakes: Literature review. *Energy research Centre of the Netherlands*, pages 1–46, 2009. doi: 10.1002/we.

B. Sanderse, S.P.van DerPijl, and B. Koren. Review of computational fluid dynamics for wind turbine wake aerodynamics B. *Wind Energy*, 14(February):799–819, 2011. doi: 10.1002/we.458.

H. Sarlak, T. Nishino, L. A. Martínez-Tossas, C. Meneveau, and J. N. Sørensen. Assessment of blockage effects on the wake characteristics and power of wind turbines. *Renewable Energy*, 93:340–352, 2016. ISSN 18790682. doi: 10.1016/j.renene.2016.01.101. URL http://dx.doi.org/10.1016/j.renene.2016.01.101.

Sasan Sarmast, Reza Dadfar, Robert F. Mikkelsen, Philipp Schlatter, Stefan Ivanell, Jens N. Sørensen, and Dan S. Henningson. Mutual inductance instability of the tip vortices behind a wind turbine. *Journal of Fluid Mechanics*, 755: 705–731, 2014. ISSN 14697645. doi: 10.1017/jfm.2014.326.

Jens N. Sørensen and Wen Zhong Shen. Numerical modeling of wind turbine wakes. *Journal of Fluids Engineering, Transactions of the ASME*, 124(2):393–399, 2002. ISSN 00982202. doi: 10.1115/1.1471361.

Jens N. Sørensen, Robert F. Mikkelsen, Dan S. Henningson, Stefan Ivanell, Sasan Sarmast, and Søren Juhl Andersen. Simulation of wind turbine wakes using the actuator line technique. *Philosophical Transactions of the Royal Society A: Mathematical, Physical and Engineering Sciences*, 373(2035), 2015. ISSN 1364503X. doi: 10.1098/rsta.2014.0071.

Niels N Sørensen. *General purpose flow solver applied to flow over hills*. PhD thesis, Risø National Laboratory, 1995.

M. Steinbuch, W. W. de Boer, O. H. Bosgra, S. A.W.M. Peters, and J. Ploeg. Optimal control of wind power plants. *Journal of Wind Engineering and Industrial Aerodynamics*, 27(1-3):237–246, 1988. ISSN 01676105. doi: 10.1016/0167-6105(88)90039-6.

L. J. Vermeer, Jens N. Sørensen, and A. Crespo. Wind turbine wake aerodynamics. *Progress in Aerospace Sciences*, 39 (6-7):467–510, 2003. ISSN 03760421. doi: 10.1016/S0376-0421(03)00078-2.

J W Wagenaar and J G Schepers. Leaflet : Controlling Wind in ECN ' s Scaled Wind Farm. *TNO Publications*, 2012.

P. D. Welch. The Use of Fast Fourier Transform for the Estimation of Power Spectra. *IEEE Transactions on audio and electroacoustics*, 15(2):70–73, 1976.

Wei Yu. *The wake of an unsteady actuator disc*. PhD thesis, Delft University of Technology, 2018.

Ali Emre Yılmaz and Johan Meyers. Optimal dynamic induction control of a pair of inline wind turbines. *Physics of Fluids*, 30(8), 2018. ISSN 10897666. doi: 10.1063/1.5038600.

Frederik Zahle, Jeppe Johansen, and Niels N. Sørensen. Wind turbine aerodynamics using an incompressible overset grid method. *European Wind Energy Conference and Exhibition 2007, EWEC 2007*, 1(January):1–21, 2007.